

Methane Pyrolysis for Zero-Emission Hydrogen Production: A Potential Bridge Technology from Fossil Fuels to a Renewable and Sustainable Hydrogen Economy

Nuria Sánchez-Bastardo,* Robert Schlögl, and Holger Ruland*

Cite This: *Ind. Eng. Chem. Res.* 2021, 60, 11855–11881

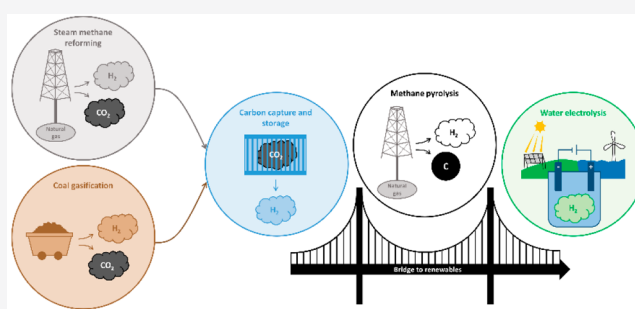
Read Online

ACCESS |

Metrics & More

Article Recommendations

ABSTRACT: Hydrogen plays a key role in many industrial applications and is currently seen as one of the most promising energy vectors. Many efforts are being made to produce hydrogen with zero CO₂ footprint via water electrolysis powered by renewable energies. Nevertheless, the use of fossil fuels is essential in the short term. The conventional coal gasification and steam methane reforming processes for hydrogen production are undesirable due to the huge CO₂ emissions. A cleaner technology based on natural gas that has received special attention in recent years is methane pyrolysis. The thermal decomposition of methane gives rise to hydrogen and solid carbon, and thus, the release of greenhouse gases is prevented. Therefore, methane pyrolysis is a CO₂-free technology that can serve as a bridge from fossil fuels to renewable energies.



1. INTRODUCTION

The establishment of a sustainable power system to meet the growing energy demand is one of our most critical current challenges. The basis of this energy system is the decrease of greenhouse gas (GHG) emissions to reduce global warming, and thus, accomplish the goals set out in the Paris Agreement¹ and Kyoto Protocol.² Specifically, Germany aims to become carbon neutral by 2050.³ Since most CO₂ emissions derive from the combustion of fossil fuels for power generation, much research is concerned at present with the development of zero-emission fuels.⁴ The hydrogen economy concept is based on the use of hydrogen as a potential fuel.⁵ Hydrogen is one of the most promising energy carriers and is considered the cleanest fuel because its combustion produces only water.⁶ In addition to this, the combustion of hydrogen originates more energy on a mass basis than conventional fossil fuels.^{7,8} Hydrogen has received special attention for its application in fuel cells and internal combustion engines, enabling the creation of a low-carbon hydrogen economy.⁹ The chemical energy of hydrogen can be efficiently converted to electricity and other energy forms without GHG emissions.^{7,8,10,11} Hydrogen also plays a major role in the development of new strategies for converting industrial CO₂ emissions into important platform chemicals. This is actually one of the objectives set within the Carbon2Chem project, which aims to convert steel mill gases into base chemicals such as methanol.^{12,13} Thereby, the transformation of industrial emissions into chemicals prevents the release of GHG into the atmosphere.

Although hydrogen is a zero-emission fuel, its suitability also depends on the energy consumed and the cleanliness of the production method.¹⁴ The production of hydrogen via water electrolysis using electricity from renewable energies is the most appropriate technology from an environmental point of view due to its zero carbon footprint. The global consumption of renewables is predicted to grow in the next years, but will still remain relatively low for the foreseeable future (Figure 1).¹⁵ Drawbacks such as the fluctuations of renewable energies, geographic limitations, and problems related to energy storage have to be overcome.^{16,17} For instance, the available renewable energies in Germany, that is, onshore wind and solar energies, could provide electricity up to 2000 h a year, which is by far too less to deal with the annual power demand.¹⁸ Further electricity may be supplied by offshore wind energy, but the transportation from the coast to inland areas is still a problem today. Due to power fluctuations, energy-deficit periods will alternate with excess production seasons. The storage of power surplus could be a solution to the intermittence of renewable energy. However, large-scale energy storage remains a challenge.^{19,20}

Received: May 2, 2021
Revised: July 29, 2021
Accepted: July 29, 2021
Published: August 9, 2021



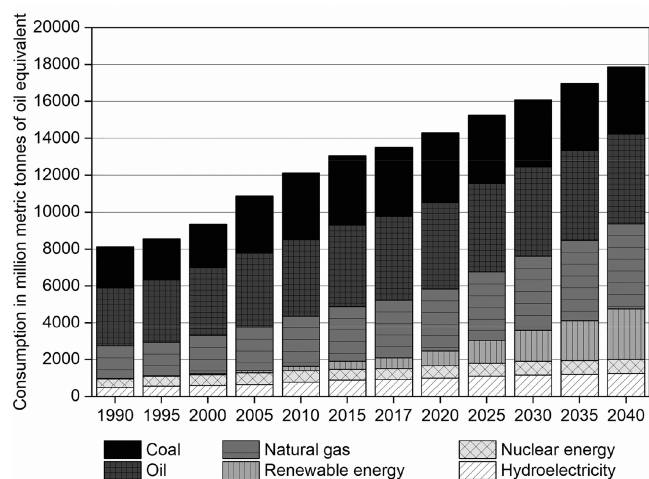


Figure 1. World energy consumption by energy source according to the data reported in ref 15.

Due to the large reserves of fossil fuels and the well-established technologies for their processing, fossil resources will still represent a major part of our energy system in the short term.^{7,21} For this reason, the development of bridge technologies based on fossil fuels with a low environmental impact has been the focus of countless studies in the last years. Among fossil fuels natural gas is currently the main source of hydrogen (48%) followed by oil (30%) and coal (18%), whereas only 4% of the global hydrogen production comes from renewable resources.⁸ Natural gas is expected to gain importance in the next few years over the use of oil and coal, the share of which within the total energy consumption will suffer a meaningful decline (Figure 1).²¹ Steam reforming and gasification of fossil fuels are currently the main processes for hydrogen production due to their technological maturity on an industrial scale. Nevertheless, the major drawback is the unavoidable generation of large amounts of GHGs.²²

Unlike these fossil fuel-based technologies, the pyrolysis of methane appears as a potential process for the transition to a sustainable hydrogen economy.²¹ Methane pyrolysis involves the thermal decomposition of methane into its components, that is, hydrogen and carbon. Therefore, the greatest benefit is the generation of CO₂-free hydrogen with solid carbon as the only byproduct. This is a unique advantage of methane pyrolysis over the conventional steam methane reforming (SMR) and coal gasification processes. Depending on the characteristics and price of the carbon product, its sale may improve the economics of the industrial methane pyrolysis process.^{9,21,23–26} Here, the main problem is the absence of markets that can accommodate such large amounts of carbon, and hence, new applications become necessary.^{9,23} The use of carbon for soil amendment and environmental remediation may be the only alternative that would offer a huge market for the carbon resulting from methane pyrolysis.^{27,28} However, further studies are needed to prove the suitability of the pyrolysis carbon for such an application.²⁷ On the other hand, if carbon is to be stored, the costs associated with solid carbon storage would be lower than the sequestration of CO₂ derived from SMR.²⁹ Owing to the depletion of natural gas, the production of hydrogen via methane pyrolysis is not a sustainable process in the long term. Nevertheless, it may be a temporary solution and probably the most cost-effective bridging technology over the transition period toward

renewable energies.²⁶ This review aims to provide a comprehensive and critical overview of methane pyrolysis with a focus on industrial application. Crucial aspects for the industrialization of the process, such as the use of suitable catalysts and the implementation of feasible processes on an industrial scale, or the finding of realistic applications for the carbon product, are thoroughly discussed in this review.

2. TRADITIONAL AND DEVELOPING TECHNOLOGIES FOR HYDROGEN PRODUCTION

At present fossil fuels undoubtedly predominate over renewable resources for hydrogen production due to their high availability and cost-effective industrially implemented processes. About 96% of global hydrogen production is obtained by coal gasification, oil/naphtha reforming, and steam reforming of methane.²¹ However, these processes have a dramatic environmental impact owing to the large amount of CO₂ emissions. Coal gasification has the largest CO₂ footprint but also the lowest product costs. Because natural gas has a lower carbon content than coal, steam reforming of methane has a much smaller carbon footprint than coal gasification, although the product costs are slightly higher (Figure 2).³⁰

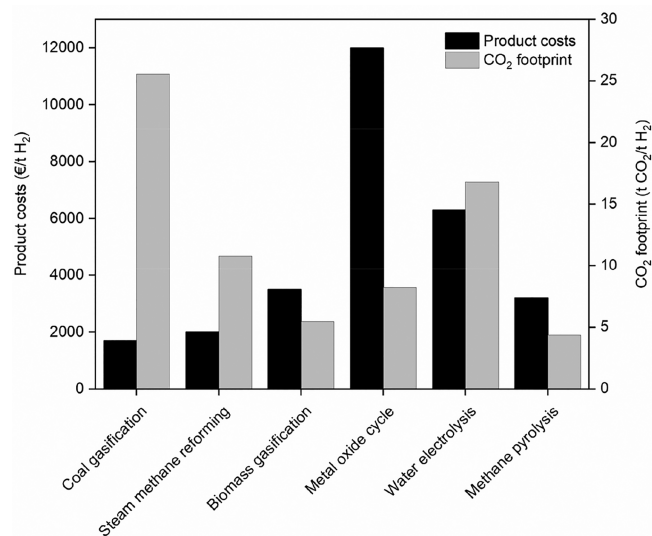


Figure 2. Product costs and CO₂ footprint of different hydrogen production technologies according to the data reported in ref 30. Note: The water electrolysis, metal oxide cycle and methane pyrolysis processes produce CO₂-free hydrogen. The CO₂ footprint of water electrolysis and the metal oxide cycle corresponds to the production of electricity from the grid. In the case of methane pyrolysis, in addition to the CO₂ emissions derived from the generation of electricity, those resulting from the extraction and transportation of natural gas are also taken into account.

SMR has a high energy efficiency (75%), but the need for carbon capture and storage (CCS) systems to obtain high purity hydrogen and decrease the GHG emissions results in a significant energy efficiency drop (60%) (Table 1),²⁸ and may increase the cost of hydrogen production more than 30%.³¹ In addition, the high electricity consumption of the conventional techniques intended for CCS increases the total environmental impact of the process.³² Dry methane reforming is an additional technology for hydrogen production using natural gas as a feedstock. This process generates less CO₂ emissions than SMR, but it is highly endothermic and is generally

Table 1. Energy Efficiencies of Different Technologies for Hydrogen Production

technology	energy efficiency in transformation (%)	energy efficiency with CCS (%)	ref
coal gasification	60	43	22
steam methane reforming	75	60	28
biomass gasification	35–50		40
thermochemical water splitting	20–45		41
water electrolysis	50–70		40
methane pyrolysis	58	58	28

intended for the production of syngas, rather than for pure hydrogen, suitable for the synthesis of higher hydrocarbons and oxygenated derivatives.³³ Biomass gasification is a mature technology that converts biomass into a hydrogen containing gas mixture. Although biomass is considered as a renewable raw material, its limited availability and the complex logistics for transportation to decentralized industries are factors that affect negatively its applicability and the final product costs.³⁰ Moreover, the production of hydrogen is accompanied by significant amounts of CO₂ that force the implementation of further separation and purification steps.⁶ For this reason, biomass gasification is usually intended for direct syngas production to generate energy or synthesize fuels rather than for obtaining pure hydrogen.³⁴

A great effort is being made to establish industrial strategies for hydrogen production with near-zero CO₂ emissions. Thermochemical water splitting and water electrolysis are developing technologies that generate only hydrogen and oxygen. The most common thermochemical water splitting process consists of redox-active metal oxide cycles, which require high temperatures (>1300 °C) that can be achieved by large-scale sunlight concentration systems.³⁵ This technology uses two practically inexhaustible sources, namely water and sun. However, according to the economic evaluation of different hydrogen production processes on a large scale, the metal oxide cycle has the highest product costs and requires a high level of investment (Figure 2).³⁰ The integration of solar energy concentration systems with structures able to split water represents an extensive value and impact on the energy and economy. Nowadays this process is not industrially feasible owing to its relatively poor efficiency and high processing costs.⁶ Water electrolysis involves the decomposition of water into oxygen and hydrogen by passing an electric current.^{36,37} Hydrogen production from water via electrolysis is a completely CO₂-free alternative only if the required electricity comes exclusively from renewable resources.³⁰ If the electricity is not 100% emission-free, water electrolysis can even exceed the carbon footprint of SMR due to the high energy requirements.³⁸ The problems related to renewable energies, such as solar and wind, are their variability and unpredictability, which leads to difficulties to match energy supply and demand. The storage of energy during periods with power surplus is often seen as a crucial element of future power systems, but it is unlikely to be a universal solution for all demand–supply imbalance problems.³⁹ In the specific case of Germany, it seems improbable that a total dependence on renewable energy will be achieved. Thus, due to the high electricity consumption, the viability of water electrolysis depends on the price and carbon footprint of the required electricity.³⁰ Both water processing technologies are still not

economically competitive with the use of fossil fuels.^{7,26} They show the highest product costs, whereas the well-developed technologies, such as steam methane reforming and coal gasification, display the lowest product costs (Figure 2). Until the use of renewable energies is sufficiently expanded, processes based on fossil resources seem to be fundamental, and thus, cleaner economic technologies need to be developed and implemented industrially.

Methane, which is the main component of natural gas, is a suitable raw material in terms of availability due to the existence of huge natural gas reserves.⁶ Since SMR leads to significant CO₂ emissions, cleaner processes have to be investigated. The thermal decomposition of methane, also known as methane pyrolysis, is an adequate alternative because hydrogen and solid carbon are the only reaction products, and thus, the formation of CO₂ is prevented during the reaction itself.^{7,9} The CO₂ footprint of methane pyrolysis (Figure 2) corresponds to the emissions derived from the required electricity and those generated during the extraction and transportation of natural gas. In any case, the CO₂ emissions corresponding to methane pyrolysis are significantly lower than those derived from the well-established fossil fuel-based technologies.³⁰ Methane pyrolysis is a one-step process,⁹ unlike SMR in which the water–gas shift (WGS) reaction has to be carried out additionally. Via the WGS reaction the CO produced in the reaction between methane and water is converted into CO₂ and additional hydrogen.^{26,38} Regarding the energy efficiency, if the sequestration of CO₂ is not considered, SMR is significantly more efficient than methane pyrolysis (75% vs 58%). However, when the implementation of CCS systems is taken into account, the net energy efficiency of both processes becomes very similar (60% for SMR and 58% for methane pyrolysis).²⁸ Methane pyrolysis is more advantageous concerning the energy input requirement as well (Figure 3). According to the standard reaction enthalpies, 37.7 kJ are needed in methane pyrolysis to obtain one mole of H₂,^{7,42} whereas in SMR coupled with the water–gas shift reaction and without taking into account the heat for water evaporation this value amounts to 41.4 kJ per mole of H₂.⁴³ Nevertheless, if the heat required to evaporate liquid water is considered, then 63.4 kJ must be applied for the production of one mole of hydrogen in the steam reforming process.⁴³ The decomposition of methane is also energetically much more favorable than water electrolysis, where 285.8 kJ are required to produce one mole of hydrogen.³⁰ Despite the advantages of methane pyrolysis, the production of hydrogen from this process is not yet competitive with the mature steam reforming technology. The estimated product costs from the decomposition of methane range from 2600 to 3200 € per ton of hydrogen depending on the expected carbon credit. In contrast, one ton of hydrogen generated by steam reforming costs 2000 €. ³⁰ However, this value could increase in the future if higher penalties for CO₂ emissions are imposed. Although methane pyrolysis cannot compete economically today with the traditional process, and even though natural gas is a fossil raw material, this technology seems to be an appropriate temporary alternative for CO₂-free hydrogen production that can serve as a bridge in a transition period toward renewable energies.

3. REACTION MECHANISM OF METHANE PYROLYSIS

3.1. Reaction Mechanism of Noncatalytic Methane Pyrolysis. Different reaction mechanisms for the noncatalytic decomposition of methane have been postulated since the

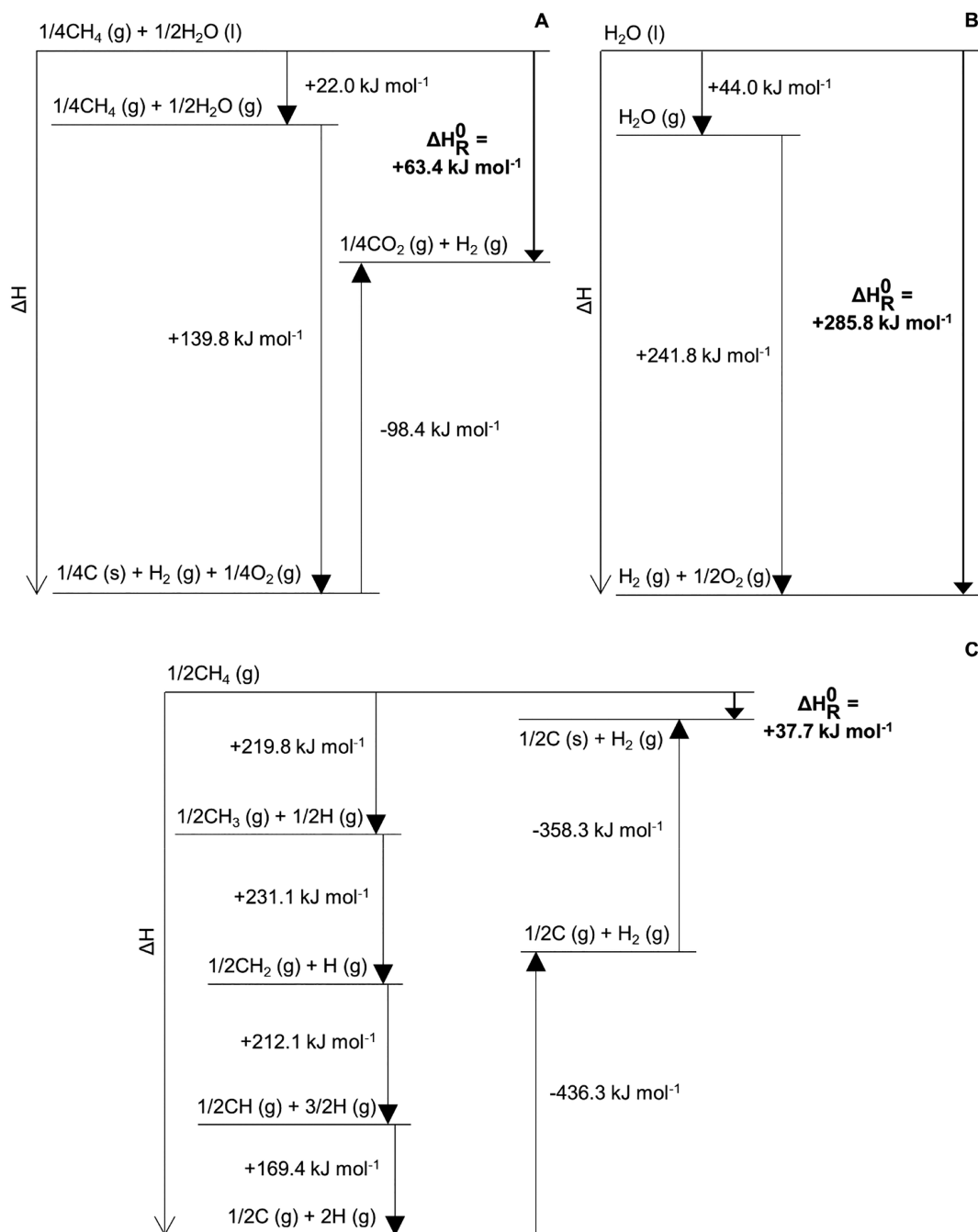
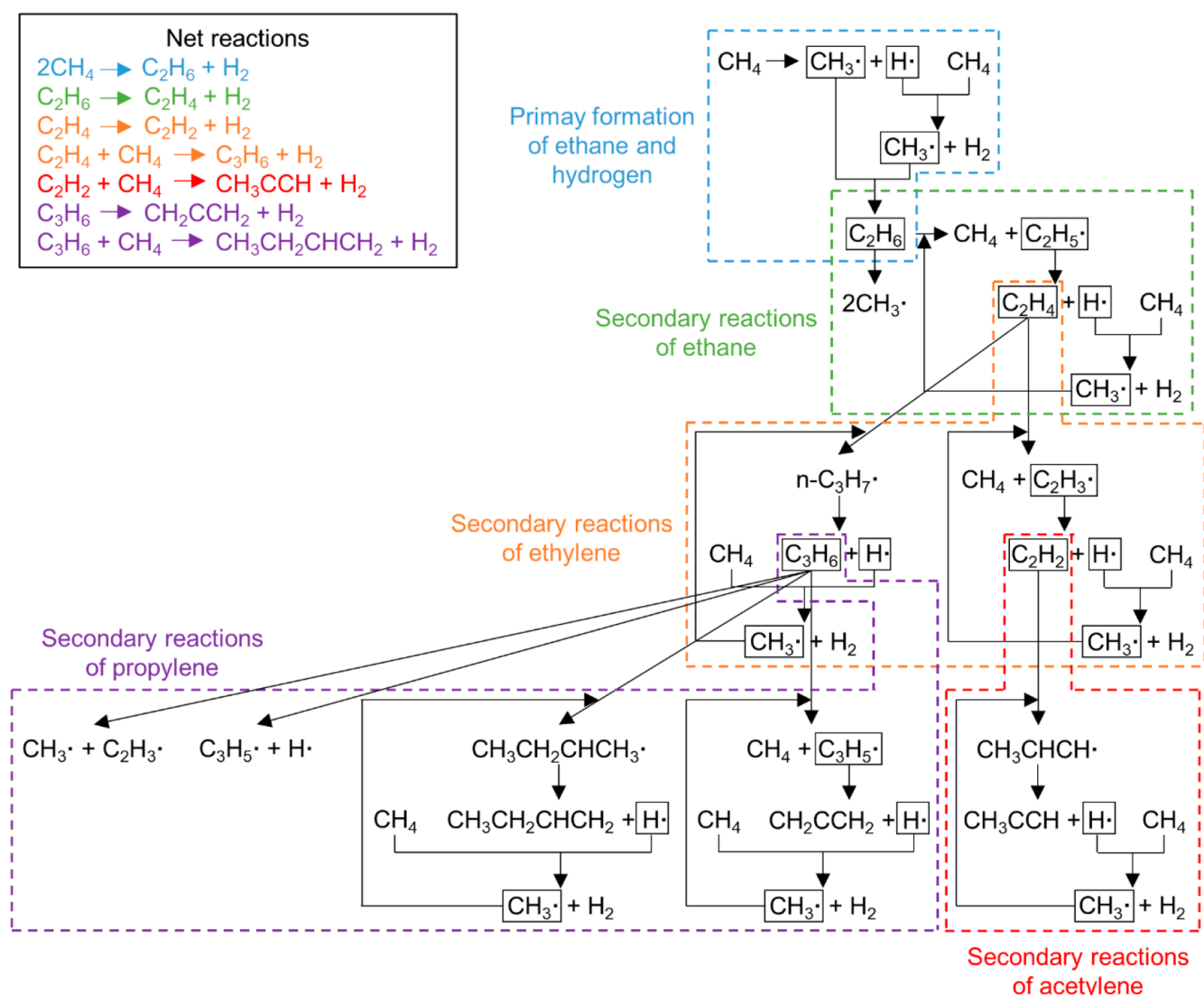


Figure 3. Enthalpy diagrams of (A) steam methane reforming, (B) water electrolysis, and (C) methane pyrolysis. $\Delta_f H_{\text{gas}}^0(\text{H}_2\text{O}) = 241.8 \text{ kJ mol}^{-1}$; $\Delta_f H_{\text{liquid}}^0(\text{H}_2\text{O}) = 285.8 \text{ kJ mol}^{-1}$; $\Delta H_{\text{vap}}^0(\text{H}_2\text{O}) = \Delta_f H_{\text{liquid}}^0(\text{H}_2\text{O}) - \Delta_f H_{\text{gas}}^0(\text{H}_2\text{O})$; $\Delta_f H_{\text{gas}}^0(\text{CO}_2) = -393.5 \text{ kJ mol}^{-1}$; $\Delta H_{\text{dis}}^0(\text{CH}_3-\text{H}) = 439.6 \text{ kJ mol}^{-1}$; $\Delta H_{\text{dis}}^0(\text{CH}_2-\text{H}) = 462.2 \text{ kJ mol}^{-1}$; $\Delta H_{\text{dis}}^0(\text{CH}-\text{H}) = 424.1 \text{ kJ mol}^{-1}$; $\Delta H_{\text{dis}}^0(\text{C}-\text{H}) = 338.7 \text{ kJ mol}^{-1}$; $\Delta H_{\text{dis}}^0(\text{H}-\text{H}) = 436.3 \text{ kJ mol}^{-1}$; $\Delta H_{\text{sub}}^0(\text{C}) = 716.7 \text{ kJ mol}^{-1}$. All enthalpies are taken from the National Institute of Standards and Technology (NIST), except the dissociation enthalpies (ΔH_{dis}^0), which were taken from ref 44.

1960s. Pyrolysis tests in shock-tube experiments have allowed measurement of the initial rate of methane dissociation.^{45–49} Most authors agree that the reaction mechanism involves a free-radical scheme with the initiating reaction step corresponding to the dissociation of methane into a methyl radical and a hydrogen atom.^{45,48,50–56} A detailed reaction mechanism resulting from experiments at low temperatures (<830 °C) was proposed in 1976 (Scheme 1).^{53,54} This mechanism is based on the cleavage of C–H bonds and the consequent formation of methyl radicals. C_{2+} hydrocarbons are generated by the

reaction between CH_3 radicals and other intermediate hydrocarbon species. In the first step, methane splits into a methyl radical and a hydrogen atom to subsequently form ethane and hydrogen molecules. In the second step, the rate of ethane formation falls gradually toward a plateau, and ethylene is obtained as a secondary product via the radical chain dehydrogenation of ethane. In addition, under certain conditions ethane can be dissociated into two methyl radicals. In the third step, acetylene and propylene are formed from ethylene via radical chain dehydrogenation and radical chain

Scheme 1. Reaction Mechanism of the Noncatalytic Methane Pyrolysis Proposed by Chen et al.^{53,54}

methylation reactions, respectively. At the same time, a sharp increase in the formation rate of ethane is observed. This fact is not explained by the described reaction mechanism, and autocatalysis is apparently involved. Unlike other works, where autocatalysis is attributed to the formation of catalytically active carbon, in the present studies the appearance of new radical sources in the autocatalytic region, probably coming from acetylene and propylene, may be responsible for the increased formation rates of ethane and the corresponding products derived from it.^{53,54}

This mechanism was extended in 1985 by adding reverse, isomerization, and abstraction and addition reactions for radicals up to C_3 reacting with primary and secondary products up to C_3 .⁵⁵ The reaction between methane and a methyl radical to produce ethane was taken into account at higher temperatures ($>1000^\circ\text{C}$) (eq 1).^{45,56} Nevertheless, the formation of ethane is unlikely above 1000°C and the direct production of ethylene from methane is more probable (eqs 2 and 3). According to the same study, the formation of benzene occurs from acetylene (eq 4) and ethylene (eqs 5–7), and even if both hydrocarbons can form carbon directly, benzene

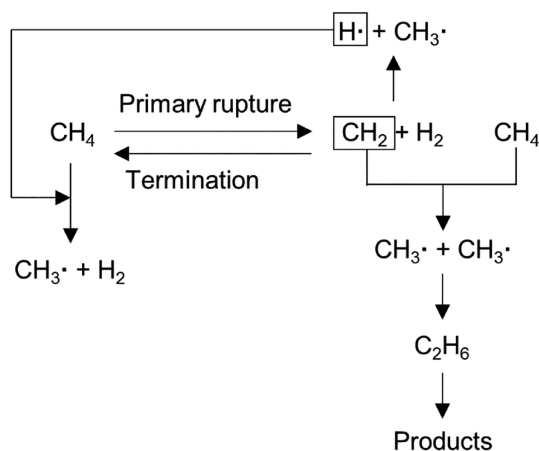
and probably higher condensed aromatics are the main species for carbon growth.⁵⁶



Although it is generally accepted that the rate-limiting step is the splitting of methane into a methyl radical and a hydrogen atom, another reaction mechanism with an alternative rate-determining step has also been proposed. In this case, the controlling stage corresponds to the dissociation of methane into methylene and a hydrogen molecule (Scheme 2):^{46,47}

These controversial results in the initiating and rate-controlling step may be related to the different temperature

Scheme 2. Reaction Mechanism of the Noncatalytic Methane Pyrolysis Proposed by Kevorkian et al.⁴⁶ and Kozlov and Knorre⁴⁷



ranges used in methane pyrolysis experiments. The decomposition of methane into a methyl radical and a hydrogen atom is observed in experiments at lower temperatures (<1400 °C), whereas the dissociation into methylene and a hydrogen molecule derives from reactions at higher temperatures (>1400 °C).⁵⁷

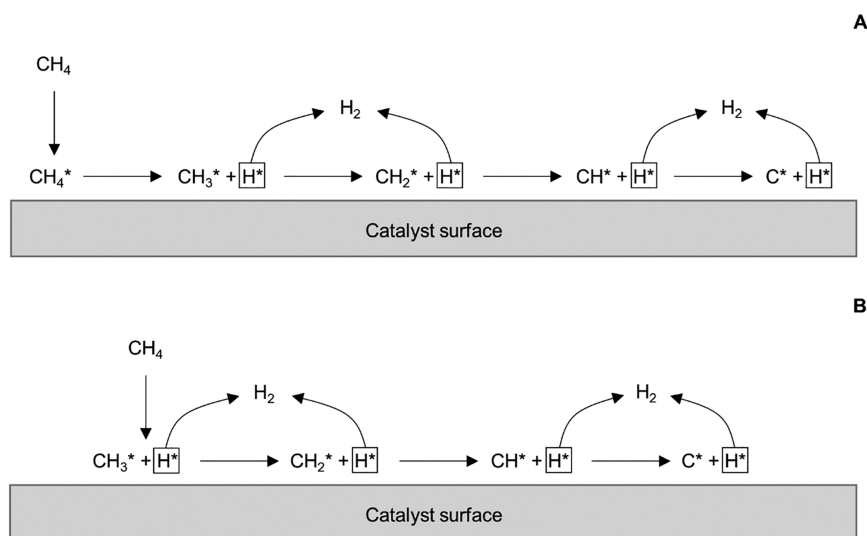
3.2. Reaction Mechanism of Catalytic Methane Pyrolysis. Several reaction mechanisms have been postulated to explain the catalytic pyrolysis reaction of methane. Some works have proposed a molecular adsorption mechanism (Scheme 3A),^{58–63} whereas a dissociative adsorption model has been described in other studies (Scheme 3B).^{64–75} In the molecular adsorption mechanism, methane is first adsorbed on the catalyst surface and then dissociates following a series of stepwise surface dehydrogenation reactions. Nevertheless, according to the dissociative adsorption model, methane dissociates upon adsorption on the catalytic active sites generating chemisorbed CH₃ and H fragments. This step is followed by the same surface dissociation reactions described

by the molecular adsorption mechanism. The dissociative adsorption mechanism emerges from studies on the interaction of methane with metal surfaces at pressures below atmospheric using molecular beam techniques with high-resolution electron energy loss spectroscopy (HREELS) and Auger electron spectroscopy.^{76–78} However, this model has also been applied to methane pyrolysis, which is usually carried out at atmospheric pressure.

Different rate-limiting steps have been proposed in the molecular adsorption mechanism. Some works consider the abstraction of the first hydrogen atom from molecularly adsorbed methane to form an adsorbed methyl group as the initiation and rate-limiting step of the decomposition of methane.^{59,63} Nevertheless, the removal of the second hydrogen from the adsorbed methyl fragment⁵⁸ or the adsorption of methane on the catalyst surface^{60,61} has also been suggested as rate-determining steps. In the dissociative adsorption mechanism, there is also no agreement on the rate-controlling step of the reaction. Some authors confirm that the dissociation of methane giving rise to a methyl group and a hydrogen atom controls the overall mechanism.^{64,75} On the other hand, according to various works on the kinetics of carbon nanotube formation, the dissociative adsorption of methane followed by the removal of hydrogen from the adsorbed methyl group limits the catalytic decomposition of methane.^{70,72,73} The kinetic models presented in the latter works differ in the number of active site types. The kinetic models for double-walled⁷⁰ and single-walled⁷² carbon nanotube synthesis are based on the presence of only one type of active sites, whereas that developed for the formation of multiwalled carbon nanotubes⁷³ considers two different types of active sites. Here, CH_x* and H* species are adsorbed on different kinds of active sites.

Other possible mechanisms arise from studies on the decomposition of hydrocarbons focused on the synthesis of carbon nanostructures via chemical vapor deposition. The vapor–liquid–solid (VLS) model was initially developed in 1964 to explain the crystal growth of silicon whiskers.⁷⁹ Some years later this mechanism was applied to the growth of

Scheme 3. Reaction Mechanisms Proposed for the Catalytic Methane Pyrolysis^a



^a(A) Molecular adsorption mechanism. (B) Dissociative adsorption mechanism.

filamentous carbon, which includes carbon nanotubes and nanofibers, over a nickel catalyst using acetylene as a carbon precursor.⁸⁰ The general VLS mechanism for the decomposition of hydrocarbons comprises several steps (Figure 4).^{80,81} First, the hydrocarbon is adsorbed on the catalyst

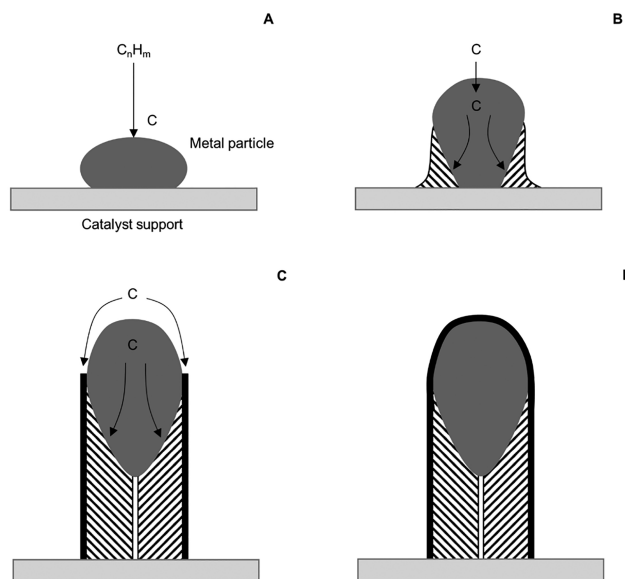


Figure 4. VLS mechanism for the growth of filamentous carbon from hydrocarbon decomposition over metal catalysts. Figure adapted with permission from refs 80 and 81. Copyright 1972 and 1989, respectively, Elsevier.

particle surface and dissociates into elemental carbon (Figure 4A). Then, carbon is taken into solution, diffuses through the bulk of the metal particle and precipitates at the backside of the catalyst particle (Figure 4B). Excess carbon accumulates at the exposed catalyst faces and is transported by surface diffusion around the catalyst particle to form the outer part of the filament. The accumulated carbon deposits force the metal particle away from the support, giving rise to the formation of the carbon filament (Figure 4C). Finally, the particle is completely encapsulated by carbon, and the filament growth ceases because there is no longer contact between the hydrocarbon and the active catalyst particle (Figure 4D).

During the third step (Figure 4C) the metal particle is distorted and elongated, and the metal is assumed to have properties of a liquid. When the metal particle is detached from the support, an initial hollow channel appears because the carbon does not have enough time to deposit in this region. The formation of filamentous carbon from the decomposition of acetylene was also studied over iron, cobalt, and chromium catalysts.⁸² The apparent activation energies for carbon growth over iron, cobalt, chromium,⁸² and nickel⁸⁰ are in agreement with those for the diffusion of carbon through the bulk of the corresponding metal. This suggests that carbon diffusion through the metal particle is the rate-determining step in the filament growth process.^{80,82} A thermal gradient may be the driving force for the bulk carbon diffusion.⁸⁰ Carbon diffuses from the hotter front face, on which the carbon precursor decomposition occurs, to the cooler backside of the catalyst particle, on which the carbon precipitates. This theory is valid when the decomposition of the carbon precursor is exothermic, as in the case of acetylene. The thermal gradient

is maintained by the exothermic decomposition of the hydrocarbon on the front face of the catalyst particle and the endothermic precipitation of the carbon at the backside. However, this hypothesis cannot explain the diffusion of carbon when the decomposition of the hydrocarbon is endothermic, as happens in methane pyrolysis. To overcome this limitation a different driving force is suggested.^{83–85} In this case, the diffusion of carbon through the metal particle derives from a carbon concentration gradient due to the different carbon solubility at the metal–gas and the metal–carbon interfaces.

Studies using high-resolution electron microscopy techniques have led to a new carbon growth mechanism.^{86,87} This mechanism does not involve the bulk diffusion of carbon species but the diffusion on the surface of the catalyst particle. The carbon species start to dissociate at the contact angle between the metal particle and the catalyst support. The accumulation of carbon at the rear part of the metal particle and the subsequent formation of lateral layers following the contour of the metal surface cause the metal particle to move away from the support, resulting in the formation of a carbon filament. The surface diffusion of carbon would also explain the hollow channel in the center of the carbon filaments.⁸⁷ Since these studies were performed with ex situ analytical methods, the microscopy images correspond to the “cold” or even deactivated catalyst. The use of in situ analytical techniques becomes thus crucial to understand the growth of carbon nanotubes and nanofibers. Images of the formation of carbon nanofibers from methane decomposition over nickel supported catalysts provided by time-resolved high-resolution in situ transmission electron microscopy demonstrate that carbon atoms do not necessarily diffuse into the bulk of the metal particles.⁸⁸ Unlike the VLS mechanism, which proposes the carbon diffusion through the metal particles as the rate-limiting stage, this model suggests that the surface transport of carbon atoms controls the rate of the nanofiber growth. This mechanism was later corroborated by other authors for the growth of nanocarbons^{89–91} and extended to the growth of graphene.⁹¹ The growth rate of carbon nanofibers over nickel, cobalt, and iron catalysts by plasma-enhanced chemical vapor deposition shows that the activation energy for carbon surface diffusion is much lower than for bulk diffusion. This would confirm the carbon diffusion on the catalyst surface as the rate-determining step for plasma-enhanced carbon growth.⁸⁹

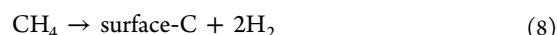
The above-described mechanisms for the growth of carbon filaments involving bulk or surface carbon diffusion correspond to a tip-growth model. In this growth model the metal particles are located at the tip of the carbon filaments since the carbon accumulated at the rear part of the catalyst particle causes its detachment from the support. The formation of carbon filaments can also follow a base-growth mechanism. Here, carbon precipitates on the apex part of the metal particle as far as possible from the support and crystallizes as a hemispherical dome. Subsequent hydrocarbon decomposition occurs on the lower surface of the particle and carbon diffuses upward, leading to the formation of carbon filaments above the metal particle, which remains attached to the support.⁹² The base-growth mechanism of carbon nanotubes is favored by strong metal–support interactions.^{93,94}

The formation of an intermediate metastable carbide phase during the nanostructure growth may also take place.⁹⁵ Here, metal particles undergo partial carburization. The metal is first transformed into a metal carbide, which is subsequently

decomposed during the synthesis of carbon filaments. The carbide cycle mechanism, that is, the decomposition of hydrocarbons through intermediate carbide-like compounds, has been reported for the growth of carbon filaments over iron and nickel catalysts.^{96–99} According to this mechanism, a metastable carbide-like intermediate compound is formed at the surface of an active catalyst particle as a result of the decomposition of the hydrocarbon. Then, the dissociation of the intermediate carbide results in the formation of carbon atoms that enter the bulk metal and lead to the supersaturation of metal by carbon. When a critical supersaturation is attained, a graphite phase is formed at the surface of the metal particle and carbon filaments start to grow. The diffusion of carbon atoms from the surface through the bulk of the metal particles to the sites of crystallization into a graphite phase takes place by a carbon concentration gradient. The decomposed intermediate carbide is restored as a consequence of the continuous dissociation of the hydrocarbon. Therefore, this cyclic process is maintained as long as there is a carbon gas source and available catalytic active sites. The presence of carbide species has been revealed for nickel catalysts in different studies.^{98,100–103} The characterization of the samples in these works was carried out using *ex situ* analytical techniques, such as transmission electron microscopy (TEM) or X-ray diffraction (XRD), after catalyst cooling. Therefore, the observed metal carbide phase could be a result of the precipitation of excess carbon on the nickel particle upon catalyst cooling.¹⁰⁴ Thus, it cannot be assured that nickel carbide is formed as an intermediate compound during the carbon growth. In addition to this, the formation of nickel carbide phases is not confirmed by *in situ* time- and depth-resolved X-ray photoelectron spectroscopy (XPS) and XRD measurements.^{105,106} This would support the fact that an intermediate carbide is not involved in the formation of carbon nanostructures over nickel catalysts.

In the case of iron catalysts, the formation of intermediate iron carbide phases has been extensively reported.^{94,100–103,107–119} Many of the works on iron catalysts were performed using *in situ* measurements.^{108,110,112,113,115,117,119} *In situ* electron microscopy images reveal that the carbide phase, which decomposes into metal and carbon, is an intermediate phase in the formation of graphite layers constituting multiwalled carbon nanotubes.¹¹⁰ Therefore, iron carbide (Fe₃C) would be involved in the growth of carbon nanotubes. The following eqs (eqs 8–11) describe the carbon nanotube growth using methane and iron catalysts.¹⁰⁰ The decomposition of metal carbides into surface graphitic carbon (eq 10) is regarded as the crucial step.

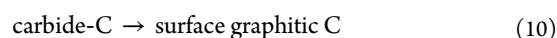
- (a) CH₄ decomposition on the catalyst surface leading to surface carbon and hydrogen:



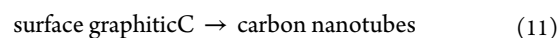
- (b) Carbon diffusion through the catalyst particles leading to carbide formation:



- (c) Formation of graphitic carbon on the catalyst surface from the metal carbide:



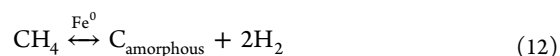
- d) Carbon nanotubes formation from surface graphite:



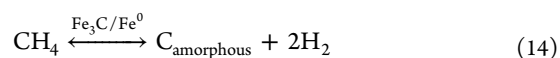
Contrary to the previous results, studies on iron and nickel catalysts based on environmental transmission electron microscopy (ETEM) and *in situ* time-resolved XPS demonstrate that a carbide phase would not be necessary for the formation of carbon nanotubes.¹²⁰ The carbide formation only occurs during the carbon nanotube growth over iron catalysts, while nickel carbide is not detected. Therefore, the growth of carbon nanotubes would not require the presence of a carbide phase.

Iron carbide may serve as an active catalyst for carbon growth^{94,113,115–117,121} and methane dissociation.^{94,118,119} A study on carbon deposition on polycrystalline iron catalysts describe different mechanisms for fresh samples and after the deposition of some carbon, as well as depending on the reaction temperature.¹²¹ Below 600 °C the rate-determining step on fresh samples is the diffusion of carbon in iron, whereas after the deposition of some carbon the rate is determined by the carbide-catalyzed hydrocarbon decomposition. Above 600 °C the surface decomposition of the hydrocarbon is assumed to be the limiting step for the carbon formation. In this case, the geometry of the catalyst surface affects the carbon formation rate on fresh samples. However, after the deposition of some carbon the rate is influenced by the iron carbide active sites instead of the geometry. The formation of γ - and α -Fe phase mixtures takes place in oxide supported iron catalysts during the reduction step prior to the chemical vapor deposition of carbon nanotubes using acetylene as a carbon source.¹¹⁷ This variation in the iron crystal structures is due to carbon contamination prior to hydrocarbon exposure. Two different growth mechanisms occur depending on the phase composition. For γ -rich iron catalyst mixtures, metallic Fe is the active phase for the growth of carbon nanotubes, whereas the formation of an iron carbide is not a prerequisite. However, for α -rich iron catalyst mixtures, the formation of Fe₃C is dominant and takes part in the carbon growth process. An investigation on nanocarbon growth over iron-based catalysts by plasma-enhanced chemical vapor deposition identifies α -Fe and Fe₃C phases depending on the growth temperature.¹¹⁶ Although at low temperatures (600 °C) only Fe₃C acts as a catalyst for the growth of carbon nanotubes both, α -Fe and Fe₃C, are active at higher temperatures. A recent study on methane pyrolysis over iron catalysts confirms that not only metallic Fe but also an iron carbide phase (Fe₃C) is active for the decomposition of methane.¹¹⁹ The proposed reaction mechanism is summarized by eqs 12–15:

- (a) Decomposition of methane on the Fe⁰ surface into amorphous carbon and hydrogen:



- (b) Reaction between the amorphous carbon and Fe⁰ to form Fe₃C or a mixture of Fe⁰ and Fe₃C, which acts as a catalyst of the reaction itself:



- (c) Diffusion of the formed carbon into Fe₃C to form supersaturated Fe₃C.

Table 2. Initial Activity of Nickel, Iron, and Cobalt Catalysts in the Decomposition of Methane for Hydrogen Production

catalyst	T [°C]	P [atm]	CH_4/N_2 [vol vol ⁻¹]	flow rate [mL min ⁻¹]	space velocity [mL h ⁻¹ g _{cat} ⁻¹]	H ₂ yield [%]	ref
Ni/CeO ₂	700	1	1/0	150	4500	53	139
Ni/La ₂ O ₃	700	1	1/0	150	4500	60	139
Ni/SiO ₂	700	1	1/0	60	7200	73	140
Fe/CeO ₂	700	1	1/0	150	4500	51	141
Fe/La ₂ O ₃	700	1	1/0	150	4500	40	141
Fe/SiO ₂	700	1	3/7	70	42000	20	94
Ni/SiO ₂	800	1	1/0	250	5000	74	134
Fe/SiO ₂	800	1	1/0	250	5000	39	134
Co/SiO ₂	800	1	1/0	250	5000	48	134

(d) Decomposition of supersaturated Fe₃C to stoichiometric Fe₃C and transformation of amorphous carbon to graphitic carbon:



From all these results, it can be concluded that different controlling steps have been proposed for the decomposition of methane. There is no general agreement, and the reaction mechanism involved in methane pyrolysis as well as the overall rate-limiting step is still unclear. Additionally, the formation of metal carbides and their role in the decomposition of hydrocarbons and nanocarbon growth is a matter of debate today. Most research on the reaction mechanism focuses on the decomposition of hydrocarbons over metal catalysts and no in-depth studies over carbon catalysts have been found. For this reason, the reaction mechanism over carbon catalysts is far from being clear. Further studies are needed to fully unravel the reaction mechanism and develop enhanced catalysts that accelerate the kinetics under optimized experimental conditions. It is essential to elucidate the reaction mechanism of methane pyrolysis and identify the determining step so that future improvements in the catalytic activity can be achieved.

4. CATALYTIC METHANE PYROLYSIS

In the absence of a catalyst the thermal decomposition of methane requires temperatures above 1000–1200 °C to achieve relevant reaction rates and methane conversions.^{6,43} Such high operating temperatures are necessary because the symmetrical molecular structure and the strong C–H bonds of methane give this molecule great stability.⁶ In order to reduce the reaction temperature and improve the hydrogen yield different metal and nonmetal catalysts (generally carbon materials) have been developed for this process over years.^{6,7,42,122} Moreover, the use of different molten metals and salts has recently attracted particular attention. Further details on the application of molten media to methane pyrolysis are described in section 6.³¹

4.1. Metal Catalysts. Transition metals, mainly nickel, iron, and cobalt, have been widely investigated as active species for methane pyrolysis. Their partially filled 3d orbitals can accept electrons from the C–H bonds of methane, which facilitates its decomposition.^{6,42,93,123–127} In addition, transition metals offer relatively high solubility and capacity for carbon diffusion through their crystalline structure.¹²⁸ Another advantage of metal catalysts is the possibility of obtaining valuable carbon nanotubes as coproduct. Nickel, iron, and cobalt are very active under moderate operating temperatures.¹²⁹ In particular, their activity exhibits the following trend: Ni > Co > Fe (Table 2).^{93,124,125,130–132} Compared to

nickel and iron, cobalt catalysts have not received much attention lately.⁶ Reasons for that are the lower activity^{133,134} and higher price than nickel, as well as toxicity problems.^{122,124,135} However, cobalt is commonly used in small amounts as a promoter of different metal-based catalysts.^{93,136–138}

4.1.1. Nickel Catalysts. Nickel catalysts show the highest initial activity among metal catalysts,^{142,143} although above 600 °C they deactivate rapidly due to carbon coking and poisoning, so that the active metal sites are encapsulated within the carbon formed during the reaction.^{6,93,124,131,136,144–148} The deactivation of the catalyst occurs when the carbon production rate, i.e., the conversion of methane, is faster than the carbon diffusion rate through the metal particles. This imbalance between the carbon production and carbon diffusion rates results in the accumulation of carbon over the metal sites, which prevents the contact of the methane molecules with the active particles and consequently deactivates the catalyst.²² To improve the stability of nickel materials, the use of suitable supports and the incorporation of different dopants have been extensively investigated.

Nickel particles are susceptible to thermal sintering in unsupported catalysts, and thus, many efforts have been made to improve their stability by the use of appropriate supports.¹³² The metal–support interaction affects the reducibility and dispersion of metal particles. Although a strong metal–support interaction hinders the reduction of nickel oxide species, it also decreases the possibility of sintering and agglomeration of nickel particles, improving their fine dispersion on the support and enabling the formation of small crystallite sizes. Consequently, the stability of the catalysts is improved.^{127,149} In some cases hardly reducible nickel solid solutions (Ni_xMg_{1-x}O)^{140,149–152} or spinel structures (NiAl₂O₄)^{153,154} are formed between the nickel particles and the support as a consequence of strong metal–support interactions. The d-orbitals of nickel in these species are completely filled and cannot accept electrons from the C–H bonds, inhibiting the adsorption and dissociation of CH₄.¹⁵³ Additionally, the difficult reducibility of nickel species prevents the formation of active metal particles.^{140,149–151,153,154} The introduction of a second oxide to the catalyst support prevents the formation of nickel structures hardly to reduce.^{153,154} For instance, the addition of TiO₂¹⁵³ or CeO₂¹⁵⁴ to the support of Ni/Al₂O₃ catalysts inhibits the formation of NiAl₂O₄ and increases the reducibility and dispersion of nickel species, which leads to improved activity and stability. Contrary to these findings, Ni/Al₂O₃·MgO shows worse catalytic performance than Ni/Al₂O₃, associated with the formation of an inactive Ni–Mg solid solution.¹⁵² Therefore, the performance of nickel catalysts is a compromise between the metal–support interaction and the

reducibility and dispersion of the metal particles. The interaction between the metal and the support has to be strong enough to avoid the aggregation of the particles and allow their fine dispersion on the support. Nevertheless, too strong metal–support interactions impede the reduction of nickel species either by increasing the reduction temperature of the nickel oxide precursors or by the formation of hardly reducible species between the metal and the support that prevent the formation of active metallic nickel.¹⁵⁵ In addition to this, a strong metal–support interaction can inhibit carbon diffusion, leading to a faster catalyst deactivation.¹⁵⁶ Therefore, a suitable metal–support interaction has to result in well-dispersed and easily reducible nickel particles and, at the same time, allow an appropriate carbon diffusion through them.

The role of promoters in metal catalysts is to create a balance between the rates of methane dissociation and carbon diffusion, that is, to modulate the dissociation rate of methane and increase that of carbon diffusion.¹⁵⁷ The addition of a second metal as a promoter, such as palladium or copper, allows working at higher temperatures without rapid catalyst deactivation. Since the decomposition of methane is an endothermic reaction, the possibility of operating at higher temperatures results in better methane conversions and hydrogen yields.^{128,158} Palladium and especially copper are the most common promoters of nickel catalysts. These metals are not active for methane dissociation because of their filled 3d orbitals, but they can significantly affect the electronic properties of nickel.^{157,159–161} Ni–Cu and Ni–Pd catalysts deactivate above 700 °C, although their stability and the deactivation temperature can be increased with increasing the promoter loading.^{125,158,162} The good stability of promoted catalysts is due to the formation of metal alloys with high lattice constants, which are able to accumulate larger carbon amounts without deactivation.^{128,158} Additionally, the higher carbon diffusion rate through the corresponding alloys rather than through the pure nickel particles prevents the formation of encapsulating carbon on the active sites.^{125,128,156,158} As a result, the generation of filamentous carbon is favored over the formation of encapsulating carbon, which consequently extends the catalyst lifetime.¹²⁵ In addition to this, promoters improve the fine dispersion of nickel particles on the catalyst support^{131,163–166} and the reducibility of nickel oxide species. The better reducibility is associated to the hydrogen spillover effect induced by the promoter. Copper and palladium are active sites for the dissociation of hydrogen molecules, and thus, facilitate the conversion of nickel oxide species into metallic nickel during the reduction step prior to the reaction.^{127,128,165–167} The presence of a larger number of weakly interacted nickel species on the support after doping may also benefit the reducibility^{156,158,165,166} and prevent the formation of hardly reducible nickel structures.^{131,163}

The dopant loading in nickel catalysts is a crucial parameter. Catalysts with higher promoter loadings are stable at higher temperatures, and thus, the deactivation temperature grows with the content of the dopant.^{125,158,162} The higher lattice constants of highly doped catalysts might explain this fact.^{158,162,168} Nevertheless, there is an optimized promoter loading for a given reaction temperature.^{125,131,145,146,162,167} The addition of small dopant amounts results in stable materials with a good metal dispersion and small crystallites that inhibit nickel sintering.¹⁴⁶ However, excessive promoter loadings lead to faster deactivation and worse thermal stability of the catalyst due to the dramatic decrease in surface area and

the formation of large, poorly dispersed nickel crystals.^{125,146,167}

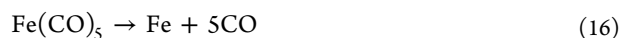
4.1.2. Iron Catalysts. Although iron is less active than nickel for the decomposition of methane, iron catalysts are more resistant to carbon coking and poisoning at high temperatures.^{136,144,169} At low reaction temperatures (<600 °C) nickel-based catalysts exhibit superior catalytic performance, whereas iron materials are still active at higher temperatures at which nickel catalysts deactivate very fast. Unlike nickel, iron materials are stable up to 700–1000 °C.^{6,119,144,170} The higher stability is related to the carbon diffusion rate, which is 3 orders of magnitude higher through iron compared to nickel.^{130,131,149} Thus, iron catalysts keep a better balance between the rates of carbon production and diffusion, leading to a longer catalyst lifetime. Compared to cobalt- and nickel-based materials, iron catalysts are inexpensive and non-toxic.^{119,171–175} Furthermore, the carbon coproduct in iron-catalyzed reactions is free of harmful metals and thus has the potential to be traded or safely stored. For these reasons, iron catalysts are the preferred option to industrialize the pyrolysis process of methane.^{174,176}

Metal promoters influence different catalyst properties (reducibility, surface area, metal dispersion, carbon capacity) and lead to the formation of bimetallic materials that are catalytically more active and stable compared to the corresponding monometallic iron catalysts. An adequate promoter enhances the reducibility of iron oxide species into metallic iron by decreasing the reduction temperature, probably due to the hydrogen spillover effect created by the promoter. A better reducibility of iron catalysts is observed after the addition of cobalt, copper, palladium, molybdenum, and nickel.^{136,177–180} Another advantage of catalyst doping is the increase in the surface area, which takes place over Fe–Mo^{179,181,182} and Fe–Co^{123,182} catalysts. Furthermore, the greater metal dispersion in different bimetallic materials (Fe–Co, Fe–Ni) affects positively the catalytic performance.¹³⁷ The incorporation of a second metal (Ni, Co) also leads to higher carbon capacities and decreases the carbon deposition rate over the active sites due to the balance between the carbon atom formation, diffusion, and precipitation. Consequently, the promoted iron catalysts are more stable and exhibit longer catalyst lifetimes.^{123,136,147,183}

Supported and unsupported iron catalysts as well as different iron organometallic precursors have been investigated in the decomposition reaction of methane. Unsupported and highly iron-loaded materials have a low catalytic activity and deactivate quickly due to the small iron surface area.¹⁸⁴ Bulk iron catalysts are highly susceptible to deactivation also because of their large particle size.¹⁷⁰ Additionally, the poor dispersion of metal particles and the formation of a solid solution between the metal and the support are responsible for the low methane conversion over highly metal-loaded catalysts.¹⁸⁴ Thus, the support plays a crucial role in the suitable dispersion of the iron particles and the maintenance of an effective metal surface during the reaction.¹⁸⁴ The incorporation of a support reduces the sintering effect, so that supported catalysts present a remarkably higher stability.¹⁷⁰ For these reasons, iron catalysts prepared on a suitable support are preferred over unsupported materials. Al₂O₃ is the most common support of iron catalysts. The combination of Fe⁰ and Al₂O₃ keeps a balance between the rate of methane decomposition, and thus, the carbon formation, and the diffusion rate of carbon through the

catalyst particles, avoiding the fast formation of encapsulating carbon.¹¹⁹ The formation of some spinel structures (FeAl₂O₄, MgFe₂O₄, Fe₂SiO₄) between the metal and the support may also take place.^{119,126,147,149,174,177,181} Nevertheless, their role in the catalytic activity is still unclear. FeAl₂O₄ species are detected in some Fe/Al₂O₃ catalysts. Although FeAl₂O₄ is inactive for methane decomposition, the interaction between the metallic iron particles and FeAl₂O₄ may play a positive role as the FeAl₂O₄ species can enhance the catalytic activity by preventing the agglomeration of metal particles through the strong bonding between Fe and FeAl₂O₄.^{119,174,177} Different iron species are found in several Fe/Al₂O₃ catalysts depending on the reduction temperature. Here, the samples with a combination of Fe⁰ and FeAl₂O₄ are more active than those containing Fe⁰ and Fe₃O₄.^{119,174} The formation of FeAl₂O₄ spinel structures is not observed in other works, but the strong interaction between iron and the alumina support is also beneficial because it prevents metal particles from agglomeration.⁹⁴ Contrary to these results, the strong metal–support interaction and the spinel formation are reported to be unfavorable.¹⁴⁷ Different iron species, and hence, different catalytic activities may be observed depending on the catalyst preparation method. For example, Fe/Al₂O₃ catalysts synthesized by impregnation are more active and stable than those prepared by coprecipitation. Catalysts synthesized by coprecipitation contain Fe₂O₃ and Fe species, whereas the catalysts prepared by impregnation present spinel species (FeAl₂O₄) and Fe₃O₄ in addition to some Fe₂O₃ and Fe species.¹²⁶ The activity is related to the presence of Fe²⁺ in FeAl₂O₄ and Fe₃O₄ phases but not to the formation of a spinel structure itself, as stated in other works.^{119,174,177} The appearance of Fe²⁺ in the samples synthesized by impregnation may be positive for the formation of catalytic active sites via in situ reduction during methane decomposition. The impregnation method may also be suitable due to the low interaction between iron and Al₂O₃ and the easier reduction of the resulting catalysts.¹⁴⁷ The appearance of the MgFe₂O₄ spinel phase is detected in some Fe/MgO catalysts as well.^{149,181} The existence of MgFe₂O₄ indicates a strong metal–support interaction, which hinders the reduction of the iron oxide precursor.¹⁸¹ The low surface area of the catalyst and the difficult reduction of the metal particles may be the reasons for the poor activity of Fe/MgO.

Different organometallic compounds, such as iron pentacarbonyl (Fe(CO)₅) and ferrocene (iron dicyclopentadienyl, Fe(C₅H₅)₂), have mainly been intended for the production of carbon nanotubes. Fe(CO)₅ decomposes at temperatures higher than 300 °C (eq 16),⁷¹ whereas the decomposition of ferrocene takes place above 500 °C (eq 17):^{71,185}



Ferrocene has been more widely used than Fe(CO)₅. This is probably due to the low cost, innocuousness, and nontoxicity of ferrocene in contrast to Fe(CO)₅.¹⁸⁵ Ferrocene is a suitable organometallic compound for carbon nanotube growth since it not only gives rise to small iron metal particles but also acts as a carbon source upon its thermal decomposition. The formed iron particles agglomerate into clusters that serve as a catalyst for the decomposition of the reactive carbon species produced in the gas phase (eq 17). The carbon resulting from these species constitutes the source for the subsequent formation of carbon nanotubes that nucleate and grow on the iron clusters.

A hydrocarbon is often injected as an additional carbon source. The hydrocarbon decomposes on the iron particles and produces extra carbon for the formation of larger nanotube amounts.¹⁸⁶ The experimental setup for this process usually consists of a low and a high temperature furnace.^{72,73,187–190} Ferrocene sublimes in the first oven at low temperature (>150 °C). Then, ferrocene as a vapor is carried by a gas stream (Ar, H₂, N₂ and/or hydrocarbons such as acetylene, methane, benzene) into the second furnace at a higher temperature (800–1100 °C). In the second oven ferrocene and the additional hydrocarbon decompose, giving rise to the growth of carbon nanotubes. Ferrocene and Fe(CO)₅ have also been employed as iron catalyst precursors for the pyrolysis of methane with the aim of producing hydrogen, although this application has been rarely reported.⁷¹ In this case, the iron clusters derived from the decomposition of the organometallic compound act as an in situ generated catalyst. Since different gaseous products result from the breakdown of Fe(CO)₅ (eq 16) and ferrocene (eq 17), the outlet gas must be cleaned to remove the undesirable impurities (CO, C₃H₆) and obtain high quality hydrogen. The poisoning of the outlet gas with unwanted compounds may explain the scarce application of these organometallic catalyst precursors in the decomposition of methane for hydrogen production.

4.1.3. Regeneration of Metal Catalysts. Different regeneration methods can be employed to remove the carbon deposits from metal catalysts and restore their activity. The reactivation techniques include combustion with oxygen or air of the carbon byproduct^{191–197} and gasification with steam^{191,195,198,199} or carbon dioxide.^{195,196,200} During oxygen/air regeneration the carbon deposits are burned with oxygen, giving rise to CO₂ in a complete combustion and CO if the oxidation is incomplete. This technique has been used to restore the activity of nickel catalysts. All the carbon on the catalyst surface is eliminated after combustion in air at 550–600 °C.^{191,192,195} The initial activity for hydrogen production is restored after regeneration^{192,193,195} but the deactivation rate of the regenerated catalyst is much faster compared to the fresh catalyst.^{192,194,197} This fact is attributed to the increase in the crystallite size due to particle sintering,¹⁹² the disintegration of the catalyst into fine powder, and the change in the face planes of the metal atoms occurring during the regeneration.¹⁹⁴ The disintegration of the catalyst may also be related to the destruction of the porous support during the filament growth.¹⁹⁴ The combustion of carbon involves an exothermic reaction so that the release of heat can give rise to high temperatures in the reactor and harm the catalyst.¹⁹⁴ To avoid damaging the catalyst the regeneration with air should be accomplished in a fluidized-bed reactor since in a fixed-bed reactor some hot spots may be formed.¹⁹⁵ Using a low oxygen concentration can also help to avoid high temperatures in the reactor.¹⁹⁷ The heat released during the oxidation of the carbon can be used to thermally sustain the endothermic reaction of methane decomposition.^{193,195} The regeneration with air is much faster than with steam or CO₂,^{195,196} but unlike these techniques, the initial metallic nickel is converted to nickel oxide during air combustion and the catalyst has to be reduced again before the next reaction cycle.^{191,192,195,196} In the gasification process with steam, carbon reacts with water steam, and a gaseous mixture composed of CO_x and H₂ is obtained. One advantage of this procedure is the avoidance of a new reduction step because the metallic nickel form is preserved.^{191,195} Furthermore, additional hydrogen can be

Table 3. Determining Factors of the Activity and Stability of Carbon Catalysts

determining factors of activity	ref	determining factors of stability	ref
defect concentration	68,69,144,201,203–206,210–215	total surface area	217,218
surface area	68,69,204,211–213,215	external surface area	69,129,207,209,212
concentration of surface oxygenated groups released as CO and CO ₂	206,217,218	pore volume	201,208,213,221
concentration of surface oxygenated groups desorbed as CO	208	structure (interconnected mesoporosity)	69,129,207,209

produced by steam gasification, which leads to higher global hydrogen yields.^{191,198} However, the regeneration with steam requires long times and not all carbon species can be removed.¹⁹⁵ Although a small amount of carbon deposits is not eliminated with steam, neither structural changes in the nickel particles nor a significant loss of catalytic activity occur after several successive decomposition–regeneration cycles.¹⁹⁸ The reactivation process by CO₂ gasification results in the formation of CO. This method preserves the reduced state of the metal^{195,196} but also requires long regeneration times.¹⁹⁵ The application of CO₂ regeneration is limited by the low carbon removal rate and the high endothermicity of the reaction.¹⁹⁶

All the regeneration methods described above lead to the formation of CO_x products, which is an important drawback taking into account the clean nature of methane pyrolysis. In addition to this, the carbon byproduct is destroyed, and the carbon nanotubes cannot be recovered. An additional technique to overcome these problems is catalyst regeneration by using an acid or a base.⁹⁴ This procedure enables not only the separation, purification, and generation of highly pure and crystalline carbon products, but also the reactivation of metal catalysts. The formation of base-grown instead of tip-grown carbon nanotubes is required to avoid catalyst damage. If the metal particles were located at the tip of the carbon nanotubes, they would be dissolved in the acid or base and the catalyst would be destroyed. Contrary to tip-grown carbon nanotubes, base-grown carbon nanotubes, where the metal particles remain attached to the support, can be easily harvested without sacrificing the catalyst. Nevertheless, the use of homogeneous acids to remove the carbon deposits is contraindicated at the industrial level and should be avoided.

The regeneration of the spent catalyst may improve the economics of the process, but constitutes a real challenge for scaling-up. The reactivation technique should be energy efficient and environmentally friendly, with short regeneration times, and generate a catalyst with good catalytic performance. Nevertheless, none of the state-of-the-art methods meet these requirements²² and more in-depth studies are essential to advance the development of the pyrolysis process on a large-scale.

4.2. Carbon Catalysts. Carbon materials are usually less active than metal catalysts and require higher reaction temperatures, normally between 800 and 1000 °C, depending on the type of carbon.^{6,9,176} However, carbon catalysts are more stable and exhibit longer catalyst lifetimes. The application of carbon materials in methane pyrolysis has been widely investigated in recent years due to their significant advantages over metal catalysts for the industrialization of the process. Compared to metal catalysts, carbon materials are significantly cheaper. In addition, the resulting carbon product may also have catalytic effects so that the decomposition of methane could be sustained for longer times without an important activity decay. In this case, the carbon catalyst would

be required only for the initiation of the reaction, and the separation of the carbon product from the carbon catalyst may not be essential. Consequently, CO₂ emissions resulting from the regeneration process could be prevented. Carbons are also resistant to sulfur and other impurities contained in natural gas, and hence, it would not be necessary to purify the feed gas before entering the reactor. The nontoxicity of the resulting carbon after reaction and the possibility of its subsequent use or secure storage are additional determining factors for the industrial implementation of methane pyrolysis based on carbon catalysts.

Activated carbons and carbon blacks are the most common carbon materials, but some others, such as graphite, diamond powder, carbon nanotubes, glassy carbon, fullerene soot, fullerenes C_{60/70}, acetylene black, coal char and ordered mesoporous carbons (CMK materials), have also been investigated.⁶⁸ Amorphous carbons (activated carbon, carbon black, acetylene black, coal char) have a disordered structure with a large number of high-energy sites (HES) on their surface. HES include dislocations, low-coordination sites, vacancies, atoms with free valences, discontinuities, edges, defects, and other energetic abnormalities. It is generally accepted that HES constitute the main fraction of active sites in carbon catalysts so that the number of HES determines their catalytic activity. For this reason, amorphous carbons, which have a high defect concentration, are usually more active than well-ordered materials. The carbon atoms in HES react with methane molecules in order to compensate their charge and stabilize themselves energetically, giving rise to the decomposition of methane.

Among the amorphous structures, activated carbons and carbon blacks are the most used materials due to their high activity.^{6,7,9,33,201} Although activated carbons are initially more active than carbon blacks, carbon blacks are more stable and show longer catalyst lifetimes.^{68,69,144,202–211} Different catalyst properties determine the activity and stability of carbon materials, as shown in Table 3.

4.2.1. Activity of Carbon Catalysts. The threshold temperature, which defines the temperature at which hydrogen starts to be produced, has been used as a measure of the initial activity of carbon catalysts.^{69,144,207,209,212} Low threshold temperatures are equivalent to high catalytic activities. Activated carbons (mesoporous and microporous), carbon blacks (black pearls 2000 and Vulcan XC72) and CMK catalysts (CMK-3 and CMK-5) exhibit the lowest threshold temperatures, and hence, the highest initial activity. Their high initial activity is linked to the large density of graphene defects, which are preferential sites for methane adsorption and dissociation. A direct linear relationship exists between the amount of defects on the graphene layers and the threshold temperature^{69,144} as well as the initial reaction rate.²¹³ This fact strongly supports that the surface defects are the main active sites of carbon catalysts. Additionally, the defect concentration and the degree of order, that is, the crystallinity of the carbons,

are correlated parameters. Disordered structures, such as activated carbons and carbon blacks, usually have a high defect concentration and low crystallinity.^{68,129,144,206,209,214} However, CMK materials present a special behavior since, despite having a high density of carbon defects, they show an intermediate crystallinity.⁶⁹ The initial activity has not only been related to the threshold temperature but also to the initial methane decomposition rate at constant temperature. Despite this difference in the measure of initial activity, there is general agreement that carbons with a greater number of surface defects are catalytically more active.^{68,201,203–206,210,211,213–215}

Although the defect concentration of the carbon structure seems to be the most important parameter affecting the catalytic activity, other factors, such as the specific surface area and the concentration of oxygenated groups, can also influence the catalyst performance. For instance, carbons with higher surface areas usually exhibit superior catalytic activities than poor surface area materials.^{68,204,215} An approximately linear relationship in logarithmic scale has been established between the initial activity of different carbon samples and their surface areas. In other cases, despite the greater catalytic activity of carbons with larger surface areas, the relationship between both parameters is not linear.^{69,211–213} Hence, the surface area cannot be the only determining factor, and the number of defects also plays a crucial role. The increase in surface area results in an increment of the number of active sites (defect concentration).^{68,69,205} However, the catalytic activity correlates quantitatively better with the defect concentration in the graphene layers rather than with the surface area.⁶⁹ Contrary to these results, different activated carbons exhibit similar initial activities regardless of the surface area. This suggests that only a part of the surface area is involved in the decomposition of methane.²¹⁴ In other studies, carbons with comparable surface areas show very different catalytic activities, which also indicates an apparent nonrelationship between the surface area and the activity.^{68,204,215} This was observed when comparing carbons of a different nature. For instance, activated carbon from hardwood displays a higher activity than carbon black (black pearls 2000) despite their similar surface areas. The same tendency was detected with structurally close carbons with the same surface area, such as carbon black and acetylene black.^{68,204,215} The higher activity of carbon black is attributed in this case to the larger amount of oxygenated surface groups. Different trends were observed when analyzing the activity of several coal chars and activated carbons.²¹⁶ When only coal chars are compared, an increase in the surface area leads to an increase in the initial activity for methane decomposition, although the relation is not linear. However, coal chars and activated carbons with very different specific surface areas can show similar activities. Here, the nature of the carbon plays a decisive role.

The concentration of oxygenated groups on the surface of carbon catalysts may also have an effect on the initial activity. Two different mechanisms explain their influence. Oxygenated groups can react directly with methane, or can be released as CO and/or CO₂, which are active reaction sites for methane decomposition.²¹⁷ An approximately linear correlation between the initial methane conversion rate and the concentration of oxygenated groups desorbed as CO and CO₂ has been reported.^{206,217,218} Also, a good correlation has been established between the initial reaction rate and the concentration of oxygenated groups desorbed only as CO, whereas those groups released as CO₂ do not show any

influence.²⁰⁸ The exponential decay of the reaction rate during the initial period of the reaction may be due to the decrease of the surface oxygenated groups²¹⁹ but also to the partial coverage of defects (active sites) by the carbon formed during the first stages of methane decomposition.¹²⁹ Most of the oxygenated groups should be removed during the heating process before the reaction begins,¹²⁹ so that the initial activity cannot be attributed exclusively to them.^{69,129} Although oxygen groups may have an impact on the initial activity, surface defects constitute the main part of active sites.⁶⁸

4.2.2. Stability and Deactivation of Carbon Catalysts. Although carbon materials usually display longer catalyst lifetimes and higher resistance to carbon coking and poisoning than metal catalysts, they also become gradually deactivated. The long-term efficiency and stability of carbon catalysts are often evaluated from their capacity for carbon accumulation before deactivation.²¹⁷ Catalysts able to accumulate larger carbon amounts provide a more stable and sustained hydrogen production for longer times. The stability of carbon catalysts may be determined by a combination of pore size distribution and specific surface area. Mesoporous carbons with high surface areas often lead to a more sustainable hydrogen production because of their larger capacities for carbon deposition. On the contrary, the catalytic activity over microporous carbons decays more rapidly due to the lower carbon capacity and the greater mass transport limitations occurring in micropores. Even if the pores are not completely filled with carbon deposits, the narrowing of the pore mouth can also prevent the diffusion of methane molecules into the pores leading to the decrease of the catalytic activity.^{68,201} Additionally, a more or less linear relationship exists between the surface area of the fresh catalyst and the stability, that is, catalysts with higher surface areas can accommodate higher carbon amounts before deactivation, and thus, provide long-term efficiency and sustainability.^{217,218} According to the evolution of the conversion of methane and the surface area over time, which show the same trend (initial drop followed by shallow decline),⁶⁸ the catalyst deactivation may occur as a consequence of the loss in surface area.^{68,201,202,217} Contrary to these results, no relationship was found between the surface area and the long-term sustainability in other works. Therefore, catalysts with similar surface areas would not necessarily accumulate the same amount of carbon deposits.^{206,213} In this case, the pore size distribution plays a decisive role.²¹³ Carbon catalysts may also lose their activity by the progressive filling and blockage of the pores.^{144,209,217,220} For this reason, the pore volume is an important parameter that affects the catalyst lifetime since a bigger pore volume offers a larger space to accommodate carbon deposits.^{201,208,213,221} The pore volume defines the maximum amount of carbon deposits before deactivation and determines the maximum hydrogen production per mass of catalyst.²²¹ There is actually a linear correlation between the catalyst pore volume and the mass of carbon accumulated until deactivation²⁰⁸ as well as the total hydrogen production.²¹³ Furthermore, the deactivation of carbon catalysts may be partly explained by the loss of oxygenated groups on the surface over reaction time.²²¹ Before catalyst deactivation the carbon product derived from methane decomposition may also have some catalytic effects. This fact is revealed by several kinetic studies, in which the carbon deposition rates are calculated throughout the reaction.^{129,208,219} Three different zones are identified along the reaction rate curves from the start of the reaction to catalyst

deactivation. The first zone corresponds to an exponential decay of the catalytic activity, attributed to the removal of oxygenated groups from the catalyst surface,^{208,219} or to the partial coverage of defect sites by the carbon product.¹²⁹ The second zone is characterized by an increase in the reaction rate. This fact denotes an autocatalytic effect, which indicates that the carbon produced from methane is also catalytically active. Nevertheless, the activity of these new active sites is clearly lower than the active sites in the fresh sample. In the last part of the kinetic curve, the reaction rate decreases until the catalyst completely deactivates. This zone may correspond to the deactivation of the new active sites¹²⁹ or the drop in the effective surface area and pore volume.^{208,219}

CMK materials, which are ordered mesoporous catalysts, and carbon blacks show the highest stability among carbon catalysts. Carbon blacks have well-defined concentric graphene layers that generate large interparticle spaces.¹⁴⁴ In addition to this, although some carbon blacks have a significant contribution of micropores to the overall surface area, they possess a high external surface area.^{207,209,212} Depending on the catalyst nature and pore structure, the carbon product remains within the pores, causing their blockage and leading to catalyst deactivation, or leaves the pores and grows to the outer part of the catalyst particles.⁶⁹ The latter mechanism is expected to occur in catalysts with a high proportion of external surface area (carbon blacks)^{69,129,207,209,212} or an ordered and interconnected mesoporosity (CMKs).^{69,129,207,209} The ability of carbon deposits to move and grow toward the outside part of the particles avoids pore blockage and improves the accessibility of methane molecules even after the deposition of significant amounts of carbon. All this explains the higher resistance of CMK materials and carbon blacks to carbon deactivation. Activated carbons have been widely investigated for methane pyrolysis due to their high initial activity. However, they show a poor long-term stability. Microporous activated carbons are quickly deactivated due to the micropore blockage caused by carbon deposits.^{69,207,209,212} Mesoporous activated carbons exhibit longer lifetimes than microporous materials, but the activity decay is relatively faster in comparison to carbon blacks.^{144,209} The reasons for the low stability of mesoporous activated carbons despite the high contribution of mesopores and the high share of external surface area remain unclear.

4.2.3. Regeneration of Carbon Catalysts. Different regeneration methods can restore the original activity of carbon catalysts. The regeneration techniques include combustion with oxygen or air²²² and gasification with CO₂^{218,223,224} or steam.^{225,226} The activity of carbon catalysts can be partially recovered by burning the carbon deposits with highly diluted oxygen in nitrogen. Nevertheless, the catalyst itself can also react with oxygen because it is usually more reactive than the carbon byproduct, resulting in the loss of a part of the original catalyst.²²² Via a CO₂ gasification regeneration process, the initial catalytic activity and the carbon accumulation decrease after each reactivation cycle.^{218,224} The reduction of the surface area and the concentration of surface oxygenated groups occur after each reaction–CO₂ regeneration cycle.²¹⁸ This may be due to the removal of a part of the initial catalyst, which is less resistant to CO₂ gasification than the carbon deposits. In fact, after several reaction–regeneration cycles the carbon catalyst consists mainly of carbon derived from the reaction itself, whereas the initial catalyst has been gasified. The decrease of surface

oxygenated groups would reduce the initial methane decomposition rate, and the lower surface area would decrease the capacity for carbon accumulation and shorten the catalyst lifetime. Concerning the steam gasification process, this method significantly increases the surface area of the deactivated carbon catalyst, which allows almost complete restoration of the original activity.^{225,226} Even after several reaction–regeneration cycles the initial activity is completely recovered by means of the steam activation procedure.²²⁵ In this case, the disordered and highly reactive pyrolytic carbon deposits obtained during methane decomposition are more easily oxidized than the catalyst itself.²²⁶ Therefore, steam gasification seems to be the most suitable regeneration technique to recover the initial catalytic activity of carbon catalysts. Furthermore, additional hydrogen is produced during the reactivation with steam, and thus, the overall hydrogen yield is enhanced.⁶ The activity of carbon catalysts is partially or completely recovered by the previous regeneration procedures. Nevertheless, CO_x emissions are generated in all cases. Therefore, the commercialization or storage of the resulting mixture of catalyst and carbon coproduct are the most suitable options to prevent any CO₂ emissions. Unlike nickel and cobalt catalysts, carbon materials are cheaper and nontoxic, which are important advantages over these metal catalysts to industrialize the process.

4.2.4. Co-feeding as a Way to Extend the Lifetime of Carbon Catalysts. Co-feeding of methane with minor amounts of other hydrocarbons can improve the catalytic activity of carbon materials and partially overcome deactivation problems. The addition of a second compound to the methane feed gas aims to generate a catalytically active carbon product to keep a good activity for longer times.^{68,202,227–232} Methane has been co-fed with saturated (propane), aromatic (benzene), and unsaturated (acetylene, ethylene) hydrocarbons.^{68,202} An accelerating effect on the decomposition rate of methane takes place when aromatic and unsaturated hydrocarbons are introduced. Moreover, a steady-state hydrogen production is achieved. Carbons produced from ethylene and especially from acetylene and benzene are catalytically more active for the decomposition of methane than the carbon derived from methane itself. There is a good correlation between the activity and the crystallite size of the carbon product. The smaller crystallites produced from benzene, acetylene, and ethylene possess a higher surface concentration of HES and consequently lead to greater catalytic activities. Nevertheless, carbon deposits from propane display a similar activity to that of methane-derived carbon and its incorporation does not result in a significant stability improvement.⁶⁸ This may be due to the comparable size and structure of the carbon products derived from the same family of saturated hydrocarbons (methane and propane).²⁰² In contrast, a beneficial effect of adding alkanes, such as ethane, has been observed in the noncatalytic methane pyrolysis.²³³ Here, the activation of methane and the subsequent formation of methyl radicals occur by the attack of radical species generated from the pyrolysis of ethane. These methyl radicals are successively incorporated into the pyrolysis products via radical reactions. Thus, methane can be activated by radicals generated from coexisting molecules without the use of a catalyst or operation at extremely high temperatures. The incorporation of an inert gas causes an analogous effect.⁵⁶ In this case, the activation of methane molecules occurs upon collision with the molecules of the inert gas, which accelerates the overall reaction. The co-

feeding with propylene,²²⁸ ethylene,^{227,229} and ethanol²³¹ can also reduce the deactivation of carbon catalysts and stabilize the catalytic activity for longer times. CO₂ as a co-fed gas allows the partial regeneration of the deactivated catalyst by *in situ* carbon gasification. Although CO₂ leads to the stabilization of carbon catalysts, its incorporation is not favorable from the energetic and environmental point of view.²³⁰

The co-feeding of methane is questionable for the industrialization of the process. The viability may be determined by the cost and the required amount of the co-fed compounds.⁶ Depending on the final hydrogen application, the feasibility of the industrial implementation may be conditioned if additional purification steps are necessary to remove the unconverted co-fed compounds from the final gaseous product.⁹ Therefore, further research is needed to elucidate whether the addition of a second compound to the methane feed gas is worthwhile on an industrial level.

5. OPERATING CONDITIONS

The decomposition of methane involves an endothermic reaction, and hence, the conversion of methane and the production of hydrogen are favored by high temperatures (Figure 5).^{7,9} However, an increase in methane conversion also

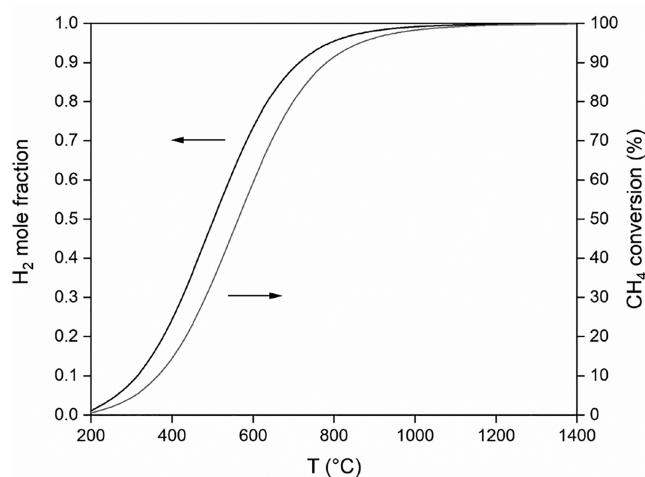


Figure 5. Hydrogen mole fraction (in the gas phase excluding carbon) and methane conversion in the thermodynamic equilibrium of methane pyrolysis at 1 bar and different temperatures (calculated using Aspen Plus software).

leads to a higher carbon production rate. In the catalytic decomposition of methane, this results in an imbalance between the carbon production and the carbon migration rates through the catalyst particles, which consequently accelerates the deactivation of the catalyst.^{125,130} Any factor that increases the rate of methane decomposition without an equivalent improvement in the rate of carbon transfer promotes the rapid loss of catalytic activity.¹³⁰ In the case of metal catalysts, the particles can sinter at high temperatures, which also favors the catalyst deactivation.^{124,127,162,167,174,234–241}

Carbon materials are less active than metal catalysts and require higher operating temperatures, usually between 800 and 1000 °C (Figure 6). There are also differences in the optimum operating temperature range depending on the type of metal catalyst. Nickel catalysts are more active but

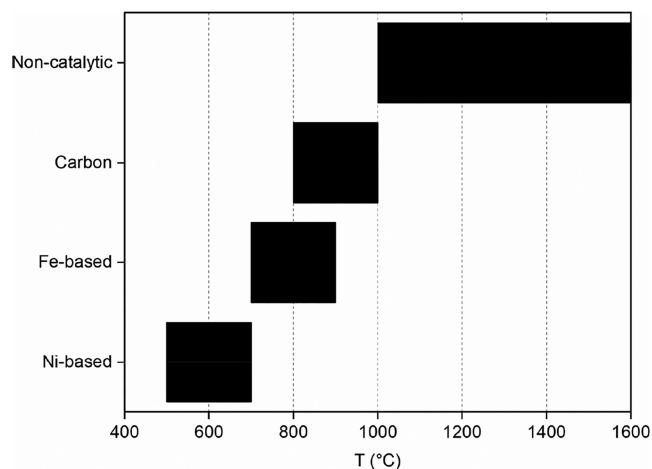


Figure 6. Temperature range of applicability of different catalysts for methane pyrolysis according to ref 22.

deactivate more rapidly than iron catalysts at high temperatures. For this reason, experiments over nickel materials are carried out in a lower temperature range (500–700 °C) than iron catalysts (700–900 °C) (Figure 6).²²

According to Le Chatelier's Principle, lower reaction pressures shift the equilibrium toward the formation of hydrogen, giving rise to a gas product with a higher hydrogen mole concentration (Figure 7A). Since keeping pressures lower than atmospheric is costly and complex, an inert gas, such as nitrogen or argon, is usually incorporated to the feed gas (Figure 7B). The addition of an inert gas decreases the partial pressure of methane, while the total pressure is maintained at 1 bar.¹⁰ At constant temperature and for the same amount of catalyst, the mass of carbon deposited per mass of catalyst decreases with a reduction in the partial pressure of methane due to a dilution effect.^{242–244} Therefore, the incorporation of an inert gas has a positive effect on hydrogen production and catalyst stability. Nevertheless, the main disadvantage is the requirement of additional separation and purification processes,¹⁰ and thus, dilution with an inert gas may not be feasible for the industrialization of methane pyrolysis.

High gas hourly space velocities (GHSVs) lead to short residence times and low contact efficiencies between the gas molecules and the catalyst. As a consequence, the amount of methane adsorbed on the catalytic active sites as well as methane conversion rate decreases.^{125,130,131,164,167,245–248} High GHSVs also cause an imbalance between the rates of carbon formation and diffusion through the catalyst particles, which favors the carbon accumulation²⁴⁹ and accelerates the catalyst deactivation.^{167,181,247} For instance, in a fluidized-bed reactor an increase in GHSV promotes the mixing between methane and the catalyst particles due to the better gas–solid contact. Nevertheless, excessive values give rise to the formation of more and bigger bubbles, which affects negatively the interaction between the reactants and the catalyst. Therefore, a compromise between a good mixing and the formation of bubbles must be found.²³⁵

Despite the numerous investigations on the effect of different operating conditions, they all focus on research at the academic level. As there are no industrially developed processes, the operating conditions are still unknown for industrial application. Further studies are required to find

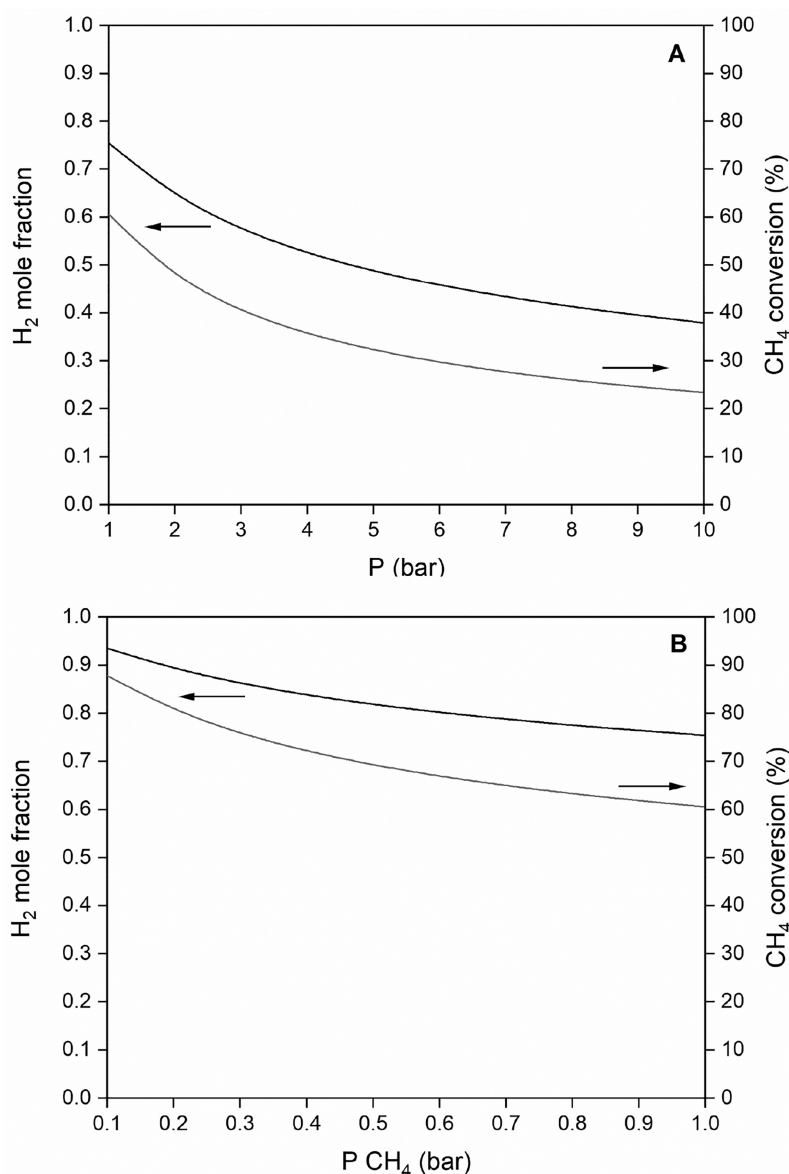


Figure 7. Hydrogen mole fraction (in the gas phase excluding carbon and nitrogen) and methane conversion in the thermodynamic equilibrium of methane pyrolysis at 600 °C at (A) different total pressures and (B) different methane partial pressures (total pressure = 1 bar, pressure balanced with nitrogen) (calculated using Aspen Plus software).

suitable experimental conditions for the implementation of an economic process on a large scale.

6. INDUSTRIALIZATION OF METHANE PYROLYSIS

The implementation of methane pyrolysis on an industrial scale requires the use of natural gas as a feed gas instead of pure methane. Research is usually limited to the use of methane as a single component, and the challenges associated with the operation with natural gas are not addressed in depth.⁴³ Therefore, the first issue to be elucidated is how the minor components of natural gas can affect the catalytic activity and stability. If they have a negative effect, a purification pretreatment will be necessary. Depending on the origin of natural gas, the minor compounds as well as their concentration may vary. Some of these impurities include ethane, propane, ethylene, H₂S, CO₂, and nitrogen.²⁵⁰ Experiments with mixtures simulating a natural gas composition (85% methane, 10% ethane, 5% propane) have been

carried out at 900 °C over carbon catalysts.²⁵⁰ The resulting gas product is only composed of unconverted methane and hydrogen, indicating the complete conversion of ethane and propane and the prevention of secondary gaseous products. In comparison to the experiments conducted with methane/nitrogen mixtures (85/15), the hydrogen concentration at the outlet improves using the simulated natural gas due to the additional hydrogen obtained from the decomposition of ethane and propane. The most important implication derived from this study is that the carbon product from these alkanes does not deactivate the carbon catalyst and the pyrolysis of methane is not negatively affected. Moreover, no extra purification post-treatments to remove ethane and propane are required since their decomposition is complete under such reaction conditions. However, it should be noted that a cleaning process may be necessary to remove possible minor compounds obtained as reaction intermediates. The presence of H₂S impurities in natural gas may also be favorable.^{250,251}

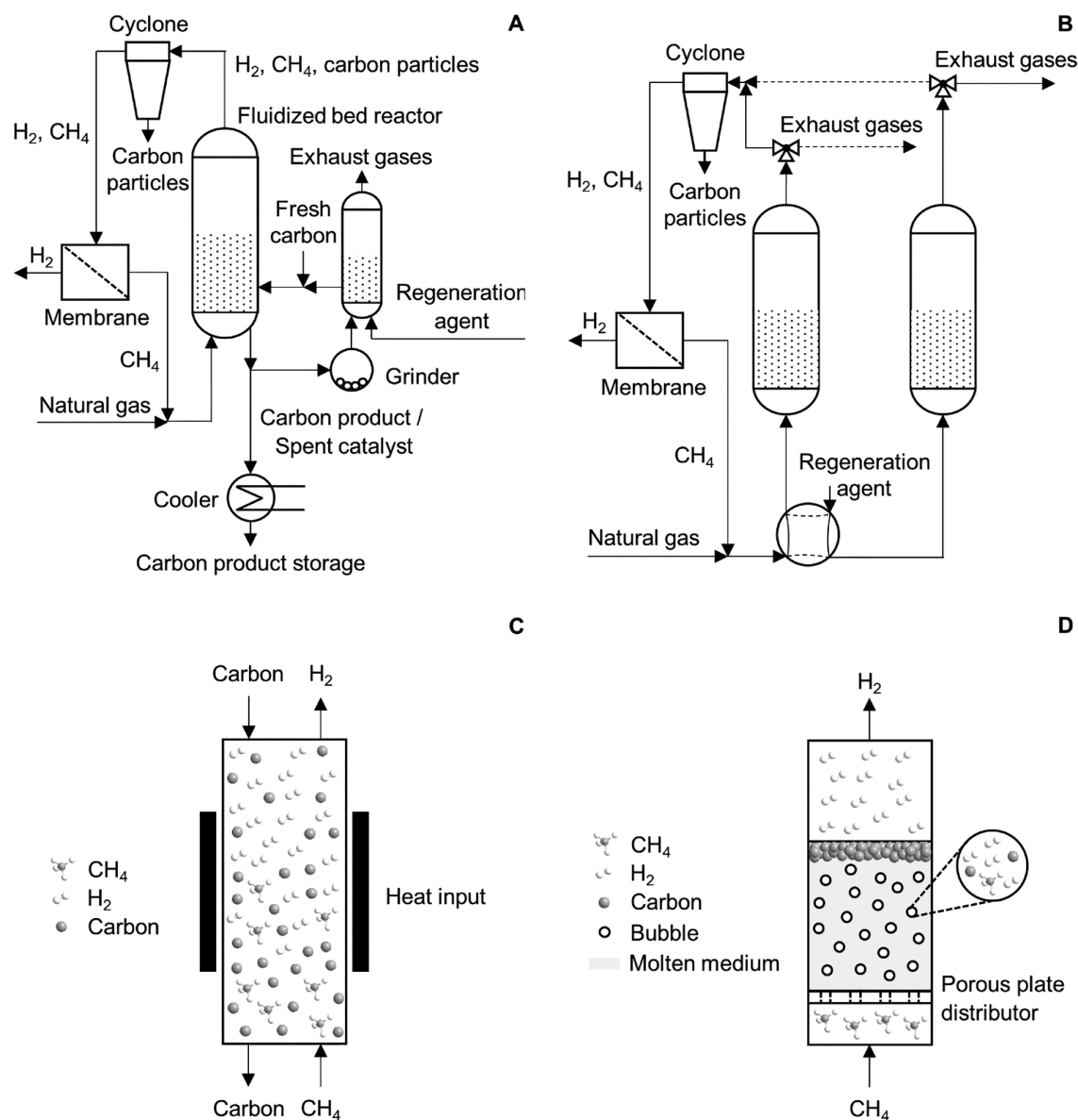


Figure 8. Potential reactor configurations for the industrial implementation of methane pyrolysis. (A) Fluidized-bed reactor with a catalyst regeneration unit according to refs 204 and 215. (B) Parallel reactors operating in a cyclic reaction-regeneration mode according to ref 199. (C) Moving-bed reactor according to ref 265. (D) Liquid bubble column reactor according to ref 263.

Carbon catalysts are not deactivated by small amounts of H₂S (up to ca. 1 vol %), but such impurities have a positive catalytic effect on the methane decomposition rate. The intermediate HS· radicals formed are able to attack methane molecules. This results in the formation of methyl radicals, which is followed by the stepwise decomposition to hydrogen and solid carbon. The resistance to H₂S deactivation is an important advantage of carbon materials over metal catalysts. Metal catalysts undergo severe deactivation in the presence of sulfur compounds and a purification treatment of natural gas becomes essential prior to the reaction.

6.1. Process Concepts for Industrial Application.

Concerning the technical implementation of methane pyrolysis on an industrial scale, different configurations may be possible, such as fluidized-bed reactors,²⁰⁴ moving-bed reactors,²⁵² or liquid bubble column reactors.^{29,31,253–263} Fixed-bed reactors are usually the preferred option on a laboratory scale. They are simple to operate and provide a better understanding of

catalyst performance, reaction kinetics, and the effect of different operating conditions.²⁶⁴ However, the main drawback is the filling of the reactor with the carbon product during long-term experiments. This increases the pressure drop and eventually blocks the gas flow.^{7,9}

Fluidized-bed reactors overcome this problem and provide additional advantages that are crucial for the industrial operation. For instance, a continuous addition and withdrawal of catalyst particles is possible in a fluidized-bed reactor. Therefore, the pressure drop does not increase significantly and the operation for longer times is possible. Additionally, the vigorous movement of the particles allows the efficient heat and mass transfer between the gas and the solid catalyst. Consequently, the temperature can be successfully controlled and the formation of hot spots is prevented.^{7,9} A potential configuration for the industrial operation with a carbon catalyst using a fluidized-bed reactor is presented in Figure 8A.^{204,215} Natural gas is introduced at the bottom of the reactor

containing the carbon catalyst particles. The outlet gas, which is composed of unconverted methane and hydrogen, is passed first through a cyclone to remove the possible entrained carbon particles. Afterward, the gaseous product stream flows through a membrane to separate methane and hydrogen. The recovered methane is recirculated and fed back to the reactor together with a fresh natural gas stream. The carbon catalyst and carbon deposits are collected at the reactor bottom, cooled, and stored. A small part of the carbon product can be introduced into the reactor after grinding and/or reactivation via a regeneration method. Another possible configuration consists of two parallel reactors (Figure 8B).¹⁹⁹ These reactors operate in a cyclic mode by switching the natural gas feed and the regeneration agent stream (air, steam) between the two reactors. Methane pyrolysis takes place in the first reactor, whereas the catalyst in the second reactor is regenerated. After a certain time natural gas is fed into the second reactor, where the pyrolysis occurs over a regenerated catalyst. In the same way, the regeneration agent is introduced in the first reactor to recover the activity of the corresponding spent catalyst. Therefore, the operation in both reactors alternates between methane pyrolysis and catalyst regeneration. Despite the promising results obtained after catalyst reactivation, the existing regeneration techniques result in undesirable CO_x emissions and should be avoided industrially. For this reason, the resulting carbon product should be intended for further applications or stored until other regeneration methods are available. In any case, obtaining a safe carbon product has to be guaranteed, and thus, toxic metal catalysts such as nickel or cobalt must be avoided. Iron and carbon catalysts are therefore the best choice to industrialize the pyrolysis process of methane.

An interesting reactor concept from the industrial point of view is the moving-bed reactor (Figure 8C) developed by different partners in a recent BMBF-funded joint project.²⁶⁵ In a moving-bed reactor natural gas and carbon granules flow in countercurrent throughout the reactor. Natural gas is fed at the bottom of the reactor, and carbon particles are fed at the top. The carbon is electrically heated by a direct current in the reaction zone. This heat is released and transferred to the feed gas. Consequently, the pyrolysis of methane takes place. The carbon originating from the reaction is accumulated on the carbon particles and continuously removed at the reactor bottom. The gaseous product is cooled down at the reactor top upon contact with the cold fresh carbon. As a consequence, the carbon is preheated by the outlet gas before entering the reaction zone and being electrically heated. The moving-bed reactor has important advantages. This kind of reactor provides a very good heat transfer between the gas and the solid catalyst. In addition, there is no back-mixing, and the residence time can be controlled for both phases. The counterflow operation allows the energy integration of the reactor, and the excellent heat transfer between the gas and the solid particles guarantees a thermally efficient process.²⁵² Although methane pyrolysis for hydrogen production is still not industrialized,⁴³ BASF plans to build a large-scale plant by 2030. They have investigated methane pyrolysis since 2010, and between 2013 and 2017 were part of the mentioned BMBF joint project based on a moving-bed reactor. Currently BASF is working on a test facility, the results of which will determine if methane pyrolysis can also succeed on an industrial scale.^{266,267}

A reactor design that is gaining importance for methane pyrolysis in recent years is the liquid bubble column reactor

(Figure 8D). This kind of reactor operates with molten media, such as molten metals (Ti, Pb, Sn, Ga), molten metal alloys (Ni–Bi, Cu–Bi) or molten salts (KBr, NaBr, NaCl, NaF, MnCl₂, KCl).^{29,31,253–263,268} Molten metals and salts act as heat transfer fluids^{254,256,259,263} and avoid temperature losses or gradients along the reactor.²⁶³ Furthermore, they could also serve as potential catalysts for the reaction.^{254,260,263} The main advantage of liquid bubble column reactors is the easy separation of the carbon byproduct from the liquid medium due to density differences.²⁹ Moreover, the low volatility and the solubility of carbon in liquids enable its deposition on the top of the molten medium and facilitate its separation and handling.²⁶³ The preferred liquid medium is based on molten metals since their density is very different from that of carbon, and thus, the carbon separation is more feasible.³¹ However, compared to molten metals, molten salts are less expensive, and are being further investigated in this field.²⁶³ The operation of liquid bubble column reactors is based on the formation of bubbles by the contact between the uprising methane gas and the liquid medium. The pyrolysis reaction occurs at the gas–liquid interface between the bubbles and the molten metal or salt. The bubbles ascend through the reactor and their size increases as a consequence of the molar expansion caused by the production of hydrogen and due to bubble coalescence. At the same time the resulting carbon is deposited at the gas–liquid interface. When the bubbles reach the surface of the molten medium, they open and release both, hydrogen and carbon. Hydrogen leaves the reactor, whereas carbon is accumulated in layers on top of the molten metal/salt bath. High residence times of the gas in the liquid and the use of a porous plate distributor are key parameters in the design of liquid bubble column reactors. The porous plate distributes homogeneously the gas phase along the reactor and produces small bubbles that increase the gas–liquid interfaces for the reaction, and consequently, the conversion of methane is improved.²⁶³ The constant removal of carbon from the liquid medium is possible in a bubble column configuration, so that blockage of the reactor due to carbon agglomeration is avoided.^{31,254,261} Additionally, the molten metal/salt is neither contaminated nor deactivated with the carbon product.^{29,260,262} This is an important advantage over solid catalysts. Solid catalysts deactivate, and to be reused a regeneration process to burn the carbon deposits is needed, which generates undesirable CO₂ emissions.²⁹ According to a life cycle assessment to evaluate the environmental impacts of the liquid-metal technology, the pyrolysis of methane could reduce the global warming impact by up to 64% compared to the steam reforming process.²⁶⁹ Although this technology bears good prospects for the future and may be competitive with steam methane reforming,²⁶³ the industrial scale implementation is still a challenge. One important drawback is the limited stability of the molten media at the required high operating temperatures (>900–1000 °C).³¹ Also, the corrosion at such high temperatures, especially in steel-based material reactors, limits the applicability of molten metals and salts.²⁵⁷

6.2. Perspectives of the Carbon Coproduct. The quality and sale of the carbon coproduct are aspects that may improve the economic efficiency of the industrial pyrolysis of methane. The characteristics of the carbon depend on the catalyst used and the reaction conditions. The formation of carbon nanotubes and nanofibers usually occurs over metal catalysts. At high operating temperatures the diameter and

length of the carbon nanofilaments decrease,^{125,130,131} and their crystallinity and graphitization degree increase.²³⁸ Carbons with different morphologies are obtained in carbon-catalyzed reactions. The morphology of carbon deposits over carbon materials depends on the catalyst nature. The formation of carbon blacks takes place over activated carbons, whereas carbon blacks produce amorphous turbostratic structures. The use of carbon nanotubes as a catalyst favors the growth of their walls, leading to the formation of multiwalled carbon nanotubes.¹⁴⁴ Carbon products derived from methane pyrolysis, such as carbon black, carbon fibers, and carbon nanotubes, have different applications and markets (Table 4).²⁷⁰ Carbon black is mainly composed of carbon

Table 4. Global Market and Price for Potential Carbon Products²⁷⁰

carbon product	global market (metric tons)	expected price (\$/ton)
carbon black	12,000,000 (2014)	400–2,000
	16,400,000 (2022)	
carbon fibers	70,000 (2016)	25,000–113,000
	100,000 (2020)	
carbon nanotubes	5,000 (2014)	100,000–600,000,000
	20,000 (2022)	

(≥97 wt %) in the form of colloidal particles. Approximately 90% of the total carbon black is used in rubber applications (as a filler and a strengthening/reinforcing agent in the manufacture of tires and other rubber and plastic products), 9% as a pigment (to enhance formulations and coatings) and the remaining 1% for diverse applications. Carbon black is also a valuable product for the metallurgical industry and can be used as a reducing agent for the production of SiC and as a carbon additive/carburizer in the steel industry.²⁰² Although the price of carbon black depends on its features, a range can be established depending on the quality and final use.²⁷⁰ For instance, the price of ASTM-grade carbon black for use in tires ranges from 400 \$ to over 1000 \$ per ton, whereas the price of specialty grade carbon black can exceed 2000 \$ per ton. The global demand for carbon black, which was nearly 12 million metric tons in 2014, is expected to increase up to 16.4 million metric tons by 2022. In the case of carbon fibers, they are polycrystalline, two-dimensional planar hexagonal networks of carbon containing 92–100% carbon by weight. They have applications in many fields, such as aerospace, automobiles, carbon-reinforced composite materials and textiles. Carbon nanofibers are also used as hydrogen storage materials and have applications in nanoelectrical devices, nanowires, and nanosensors.¹⁵¹ The global market demand for carbon fibers was 70 000 t in 2016 and is projected to exceed 100 000 t in 2020.²⁷⁰ Carbon nanotubes (single-walled and multiwalled carbon nanotubes) find applications in polymers, electronics, plastics, and energy storage. They are mostly intended to improve the thermal, electrical, and mechanical properties of polymers, although they are getting special attention for their applications in lithium-ion batteries and renewable energy storage. The global market demand for carbon nanotubes was slightly over 5000 tons in 2014 and is projected to surpass 20 000 tons by 2022.²⁷⁰

The commercialization of the carbon byproduct may positively influence the economics of the global process by reducing the hydrogen costs. This would be possible if the global market could absorb the huge amounts of the carbon

product resulting from the pyrolysis process to meet the corresponding hydrogen demand.²⁷⁰ If the annual global production of hydrogen (ca. 60 million tons in 2017) comes from methane pyrolysis, close to 180 million tons of carbon would be generated.²⁷¹ From a different point of view, if only the hydrogen production from steam methane reforming (ca. 48% of the total hydrogen production) is replaced by methane pyrolysis, approximately 86 million tons of carbon would be obtained yearly.²⁶³ Since the current world consumption of all carbon products is only 15–20 million tons per year,²⁷¹ in none of the previous cases would the market be able to accommodate such amounts of carbon. The only realistic application for such quantities of carbon is its use in the area of soil amendment and environmental remediation, although its suitability has yet to be proven.²⁷ The use of carbon for the amelioration of soil may accommodate large amounts of carbon²⁸ and provide a virtually unlimited market for the methane pyrolysis carbon coproduct.²⁷ The addition of carbonaceous products to soil can significantly improve seed germination, plant growth and crop yields. The application of carbon to soil increases the nutrient and water retention capacity as well as the microbial abundance. Carbon can store nutrients from the soil and serve as a potential slow-release fertilizer. For this reason, the amount of fertilizers applied to soil could be significantly decreased. Furthermore, the addition of carbon to soil may reduce the CO₂ in the atmosphere by enhancing its sequestration and by reducing the CO₂ emissions from the soil to the environment. Therefore, carbon would act as a long-term CO₂ sink.^{23,27} The structure of the amorphous carbons obtained in methane pyrolysis under certain operating conditions is similar to that of the carbons commonly used for soil amendment, and thus, they are expected to have a positive effect on plant growth. Nevertheless, further investigations are required to validate the suitability of the carbon coproduct of methane pyrolysis for soil amendment and environmental cleanup.²⁷ The application in this area requires that the carbon from the decomposition of methane is not poisoned with toxic metals, such as nickel or cobalt. Consequently, the use of iron and carbon catalysts is the only possibility to obtain a carbon product free of harmful compounds with a potential application for soil improvement and environmental remediation. Carbon storage as a back-up energy source for the future is another alternative solution for the carbon byproduct.²⁶³ Unlike the CO₂ capture and sequestration systems required in the steam methane reforming process, no significant energy consumption is expected from carbon storage.²¹⁵ Furthermore, for the same hydrogen production the volume required for the storage of CO₂ in liquid form obtained via SMR would be 10 times larger than the volume needed to store the carbon produced by methane pyrolysis.²²

Methane pyrolysis has a good outlook for future as a zero-emission technology for hydrogen production. Nevertheless, at present there are still many open questions for its industrial implementation. For instance, the role of the impurities of natural gas in the catalytic performance needs to be unraveled. In addition, a suitable experimental setup must still be found to industrialize the process, and the possible commercialization or storage of the carbon product, as well as its impact on the economics of the process, must be ascertained.

7. CONCLUSIONS


The present strict regulations to reduce greenhouse gas emissions are forcing the development of a sustainable low-

carbon economy. In this context, hydrogen plays a key role in the transition to clean energy. Hydrogen has received special attention as a zero-emission fuel in fuel cells and internal combustion engines. In addition, hydrogen is essential for converting industrial CO₂ emissions into platform chemicals such as methanol, which prevents CO₂ from being released into the atmosphere. Most of the current global hydrogen production comes from coal gasification and steam methane reforming. However, both processes are accompanied by large CO₂ emissions and must be avoided to comply with restrictions on GHG emissions. Water electrolysis based on renewable energies is the greenest technology for hydrogen production, but the total dependence on renewables is not possible, at least, in the near future. Consequently, alternative fossil fuel-based processes with a low carbon footprint become essential. Methane pyrolysis is a suitable technology for converting natural gas into hydrogen without CO₂ emissions. Although methane pyrolysis is not a sustainable process due to the depletion of natural gas reserves, it can be an appropriate temporary solution until renewable energies are well established. The decomposition of methane has been extensively studied over different metal (Ni, Co, Fe) and carbon catalysts. From an industrial point of view, only the use of iron and carbon catalysts is viable due to their nontoxicity. This allows a safe storage of the carbon product or its potential application, for example, for soil amendment and environmental remediation. Nevertheless, severe temperatures are required to obtain satisfying hydrogen yields over iron and carbon catalysts. Although the reaction mechanism has been widely investigated, no clear conclusions have been drawn on the elementary reactions and the rate-limiting step. Therefore, further research is needed to elucidate these issues. This will enable the development of suitable catalysts to optimize the activity under milder operating conditions. Furthermore, the role of natural gas impurities in the production of hydrogen has to be investigated in more detail. Finding an adequate reactor configuration and a thorough understanding of how the sale of the carbon product may affect the economics of the process are additional issues that will determine the industrial implementation. Although the industrialization of methane pyrolysis still has to overcome many challenges, this CO₂-free technology is a promising process that can serve as a bridge in the evolution toward a sustainable hydrogen production based on renewable energies.

AUTHOR INFORMATION

Corresponding Authors

Nuria Sánchez-Bastardo – Max Planck Institute for Chemical Energy Conversion, 45470 Mülheim an der Ruhr, Germany;
Email: nuria.sanchez-bastardo@cec.mpg.de

Holger Ruland – Max Planck Institute for Chemical Energy Conversion, 45470 Mülheim an der Ruhr, Germany;
 orcid.org/0000-0001-5530-1458;
Email: holger.ruland@cec.mpg.de

Author

Robert Schlögl – Max Planck Institute for Chemical Energy Conversion, 45470 Mülheim an der Ruhr, Germany; Max Planck Society, Fritz Haber Institute, 14195 Berlin, Germany

Complete contact information is available at:
<https://pubs.acs.org/10.1021/acs.iecr.1c01679>

Funding

Bundesministerium für Bildung und Forschung, BMBF, Verbundvorhaben Carbon2Chem, support code: 03EK3037C. Open access funded by Max Planck Society.

Notes

The authors declare no competing financial interest.

ACKNOWLEDGMENTS

The authors would like to thank the Max Planck Society for financial support as well as the Federal Ministry of Education and Research (Bundesministerium für Bildung und Forschung, BMBF, Verbundvorhaben Carbon2Chem, support code: 03EK3037C) for funding.

ABBREVIATIONS

BMBF = Bundesministeriums für Bildung und Forschung
CCS = carbon capture and storage
ETEM = environmental transmission electron microscopy
GHG = greenhouse gas
GHSV = gas hourly space velocity
HES = high-energy sites
HREELS = high-resolution electron energy loss spectroscopy
NIST = National Institute of Standards and Technology
SMR = steam methane reforming
TEM = Transmission electron microscopy
VLS = vapor–liquid–solid
WGS = water-gas shift
XPS = X-ray photoelectron spectroscopy
XRD = X-ray diffraction

REFERENCES

- (1) *Paris Agreement to the United Nations Framework Convention on Climate Change*; United Nations, Paris, 2015.
- (2) *Kyoto Protocol to the United Nations Framework Convention on Climate Change*; United Nations, Kyoto, 1997.
- (3) <https://www.umweltbundesamt.de/daten/klima/treibhausgasemissionen-in-deutschland#emissionsentwicklung> (accessed 2021-03-18).
- (4) *CO₂ emissions from fuel combustion. Highlights*; International Energy Agency, 2018.
- (5) Viswanathan, B. *Hydrogen as an energy carrier Energy Sources: Fundamentals of chemical conversion processes and applications*; Elsevier Science Bv: Amsterdam, 2017.
- (6) Ashik, U. P. M.; Daud, W. M. A. W.; Abbas, H. F. Production of greenhouse gas free hydrogen by thermocatalytic decomposition of methane - A review. *Renewable Sustainable Energy Rev.* **2015**, *44*, 221–256.
- (7) Abbas, H. F.; Daud, W. M. A. W. Hydrogen production by methane decomposition: A review. *Int. J. Hydrogen Energy* **2010**, *35* (3), 1160–1190.
- (8) Karchiyappan, T. A review on hydrogen energy production from electrochemical system: Benefits and challenges. *Energy Sources, Part A* **2019**, *41* (7), 902–909.
- (9) Zhang, J. B.; Li, X.; Chen, H. Y.; Qi, M.; Zhang, G. R.; Hu, H. Q.; Ma, X. X. Hydrogen production by catalytic methane decomposition: Carbon materials as catalysts or catalyst supports. *Int. J. Hydrogen Energy* **2017**, *42* (31), 19755–19775.
- (10) Younessi-Sinaki, M.; Matida, E. A.; Hamdullahpur, F. Kinetic model of homogeneous thermal decomposition of methane and ethane. *Int. J. Hydrogen Energy* **2009**, *34* (9), 3710–3716.
- (11) Zhang, J. B.; Li, X.; Xie, W. T.; Hao, Q. Q.; Chen, H. Y.; Ma, X. X. K₂CO₃-promoted methane pyrolysis on nickel/coal-char hybrids. *J. Anal. Appl. Pyrolysis* **2018**, *136*, 53–61.

- (12) Deerberg, G.; Oles, M.; Schlögl, R. The Project Carbon2-Chem®. *Chem. Ing. Tech.* **2018**, *90* (10), 1365–1368.
- (13) Schittkowski, J.; Ruland, H.; Laudenschleger, D.; Girod, K.; Kähler, K.; Kaluza, S.; Muhler, M.; Schlögl, R. Methanol synthesis from steel mill exhaust gases: Challenges for the industrial Cu/ZnO/Al₂O₃ catalyst. *Chem. Ing. Tech.* **2018**, *90* (10), 1419–1429.
- (14) Dawood, F.; Anda, M.; Shafiqullah, G. M. Hydrogen production for energy: An overview. *Int. J. Hydrogen Energy* **2020**, *45* (7), 3847–3869.
- (15) *BP Energy Outlook: 2019 ed.*; BP p.l.c.: London, 2019.
- (16) Eerkens, J. W. *The nuclear imperative: A critical look at the approaching energy crisis*, 2nd ed.; Springer: Dordrecht, 2010.
- (17) Grosspietsch, D.; Saenger, M.; Girod, B. Matching decentralized energy production and local consumption: A review of renewable energy systems with conversion and storage technologies. *Wiley Interdiscip. Rev.: Energy Environ.* **2019**, *8* (4), 18.
- (18) <https://www.bdew.de/service/daten-und-grafiken/jahresvolllaststunden/> (accessed 2021-03-18).
- (19) O'Dwyer, C.; Ryan, L.; Flynn, D. Efficient large-scale energy storage dispatch: Challenges in future high renewable systems. *IEEE Trans. Power Syst.* **2017**, *32* (5), 3439–3450.
- (20) Abdalla, A. M.; Hossain, S.; Nisfindy, O. B.; Azad, A. T.; Dawood, M.; Azad, A. K. Hydrogen production, storage, transportation and key challenges with applications: A review. *Energy Convers. Manage.* **2018**, *165*, 602–627.
- (21) Weger, L.; Abánades, A.; Butler, T. Methane cracking as a bridge technology to the hydrogen economy. *Int. J. Hydrogen Energy* **2017**, *42* (1), 720–731.
- (22) Abánades, A. In *Production of Hydrogen from Renewable Resources*; Fang, Z.; Smith, J. R. L.; Qi, X., Eds.; Springer: Dordrecht, 2015.
- (23) Muradov, N. Z.; Veziroğlu, T. N. Green[®] path from fossil-based to hydrogen economy: An overview of carbon-neutral technologies. *Int. J. Hydrogen Energy* **2008**, *33* (23), 6804–6839.
- (24) Abánades, A.; Rubbia, C.; Salmieri, D. Technological challenges for industrial development of hydrogen production based on methane cracking. *Energy* **2012**, *46* (1), 359–363.
- (25) Keipi, T.; Hankalin, V.; Nummelin, J.; Raiko, R. Techno-economic analysis of four concepts for thermal decomposition of methane: Reduction of CO₂ emissions in natural gas combustion. *Energy Convers. Manage.* **2016**, *110*, 1–12.
- (26) Parkinson, B.; Tabatabaei, M.; Upham, D. C.; Ballinger, B.; Greig, C.; Smart, S.; McFarland, E. Hydrogen production using methane: Techno-economics of decarbonizing fuels and chemicals. *Int. J. Hydrogen Energy* **2018**, *43* (5), 2540–2555.
- (27) Muradov, N. Z.; Veziroğlu, T. N. From hydrocarbon to hydrogen-carbon to hydrogen economy. *Int. J. Hydrogen Energy* **2005**, *30* (3), 225–237.
- (28) Steinberg, M. Fossil fuel decarbonization technology for mitigating global warming. *Int. J. Hydrogen Energy* **1999**, *24* (8), 771–777.
- (29) Kang, D.; Palmer, C.; Mannini, D.; Rahimi, N.; Gordon, M. J.; Metiu, H.; McFarland, E. W. Catalytic methane pyrolysis in molten alkali chloride salts containing iron. *ACS Catal.* **2020**, *10* (13), 7032–7042.
- (30) Machhammer, O.; Bode, A.; Hormuth, W. Financial and ecological evaluation of hydrogen production processes on large scale. *Chem. Eng. Technol.* **2016**, *39* (6), 1185–1193.
- (31) Abánades, A.; Rubbia, C.; Salmieri, D. Thermal cracking of methane into hydrogen for a CO₂-free utilization of natural gas. *Int. J. Hydrogen Energy* **2013**, *38* (20), 8491–8496.
- (32) Dufour, J.; Serrano, D. P.; Galvez, J. L.; Moreno, J.; Garcia, C. Life cycle assessment of processes for hydrogen production. Environmental feasibility and reduction of greenhouse gases emissions. *Int. J. Hydrogen Energy* **2009**, *34* (3), 1370–1376.
- (33) Fidalgo, B.; Menéndez, J. A. Carbon materials as catalysts for decomposition and CO₂ reforming of methane: A review. *Chin. J. Catal.* **2011**, *32* (2), 207–216.
- (34) Richardson, Y.; Drobek, M.; Julbe, A.; Blin, J.; Pinta, F. In *Recent Advances in Thermochemical Conversion of Biomass*; Pandey, A., Bhaskar, T., Stöcker, M., Sukumaran, R. K., Eds.; Elsevier: Amsterdam, 2015.
- (35) Lu, Y. J.; Zhu, L. Y.; Agrafiotis, C.; Vieten, J.; Roeb, M.; Sattler, C. Solar fuels production: Two-step thermochemical cycles with cerium-based oxides. *Prog. Energy Combust. Sci.* **2019**, *75*, 49.
- (36) Chi, J.; Yu, H. M. Water electrolysis based on renewable energy for hydrogen production. *Chin. J. Catal.* **2018**, *39* (3), 390–394.
- (37) El-Emam, R. S.; Özcan, H. Comprehensive review on the techno-economics of sustainable large-scale clean hydrogen production. *J. Cleaner Prod.* **2019**, *220*, 593–609.
- (38) Von Wald, G. A.; Masnadi, M. S.; Upham, D. C.; Brandt, A. R. Optimization-based technoeconomic analysis of molten-media methane pyrolysis for reducing industrial sector CO₂ emissions. *Sustainable Energy Fuels* **2020**, *4* (9), 4598–4613.
- (39) Laugs, G. A. H.; Benders, R. M. J.; Moll, H. C. Balancing responsibilities: Effects of growth of variable renewable energy, storage, and undue grid interaction. *Energy Policy* **2020**, *139*, 111203.
- (40) Kalamaras, C. M.; Efstathiou, A. M. Hydrogen production technologies: Current state and future developments. *Conference Papers in Energy* **2013**, *2013*, 690627.
- (41) Pinsky, R.; Sabharwall, P.; Hartvigsen, J.; O'Brien, J. Comparative review of hydrogen production technologies for nuclear hybrid energy systems. *Prog. Nucl. Energy* **2020**, *123*, 103317.
- (42) Pudukudy, M.; Yaakob, Z.; Jia, Q. M.; Takriff, M. S. Catalytic decomposition of undiluted methane into hydrogen and carbon nanotubes over Pt promoted Ni/CeO₂ catalysts. *New J. Chem.* **2018**, *42* (18), 14843–14856.
- (43) Schneider, S.; Bajohr, S.; Graf, F.; Kolb, T. State of the art of hydrogen production via pyrolysis of natural gas. *ChemBioEng Rev.* **2020**, *7* (5), 150–158.
- (44) Blanksby, S. J.; Ellison, G. B. Bond dissociation energies of organic molecules. *Acc. Chem. Res.* **2003**, *36* (4), 255–263.
- (45) Skinner, G. B.; Ruehrwein, R. A. Shock tube studies on the pyrolysis and oxidation of methane. *J. Phys. Chem.* **1959**, *63* (10), 1736–1742.
- (46) Kevorkian, V.; Heath, C. E.; Boudart, M. The decomposition of methane in shock waves. *J. Phys. Chem.* **1960**, *64* (8), 964–968.
- (47) Kozlov, G. I.; Knorre, V. G. Single-pulse shock tube studies on kinetics of thermal decomposition of methane. *Combust. Flame* **1962**, *6* (4), 253–263.
- (48) Yano, T.; Kuratani, K. Initiation step of methane pyrolysis. *Bull. Chem. Soc. Jpn.* **1968**, *41* (4), 799–802.
- (49) Napier, D. H.; Subrahmanyam, N. Pyrolysis of methane in a single pulse shock tube. *J. Appl. Chem. Biotechnol.* **1972**, *22* (3), 303–317.
- (50) Palmer, H. B.; Lahaye, J.; Hou, K. C. Kinetics and mechanism of the thermal decomposition of methane in a flow system. *J. Phys. Chem.* **1968**, *72* (1), 348–353.
- (51) Yano, T. Initiation step of methane pyrolysis. Further studies on initiation step of methane pyrolysis. *Bull. Chem. Soc. Jpn.* **1973**, *46* (6), 1619–1623.
- (52) Chen, C.-J.; Back, M. H.; Back, R. A. The thermal decomposition of methane. I. Kinetics of the primary decomposition to C₂H₆ + H₂; rate constant for the homogeneous unimolecular dissociation of methane and its pressure dependence. *Can. J. Chem.* **1975**, *53* (23), 3580–3590.
- (53) Chen, C.-J.; Back, M. H.; Back, R. A. The thermal decomposition of methane. II. Secondary reactions, autocatalysis and carbon formation; non-Arrhenius behaviour in the reaction of CH₃ with ethane. *Can. J. Chem.* **1976**, *54* (20), 3175–3184.
- (54) Chen, C.-J.; Back, M. H.; Back, R. A. Mechanism of the Thermal Decomposition of Methane. *ACS Symposium Series* **1976**, *32*, 1 DOI: 10.1021/bk-1976-0032.ch001.
- (55) Roscoe, J. M.; Thompson, M. J. Thermal decomposition of methane: Autocatalysis. *Int. J. Chem. Kinet.* **1985**, *17* (9), 967–990.
- (56) Benzinger, W.; Becker, A.; Hüttinger, K. J. Chemistry and kinetics of chemical vapour deposition of pyrocarbon: I. Fundamen-

tals of kinetics and chemical reaction engineering. *Carbon* **1996**, *34* (8), 957–966.

(57) Khan, M. S.; Crynes, B. L. Survey of recent methane pyrolysis literature. *Ind. Eng. Chem.* **1970**, *62* (10), 54–59.

(58) Grabke, H. J. Evidence on the surface concentration of carbon on gamma iron from the kinetics of the carburization in CH₄-H₂. *Metall. Trans.* **1970**, *1* (10), 2972–2975.

(59) Snoeck, J.-W.; Froment, G. F.; Fowles, M. Kinetic study of the carbon filament formation by methane cracking on a nickel catalyst. *J. Catal.* **1997**, *169* (1), 250–262.

(60) Sharif Zein, S. H.; Mohamed, A. R.; Talpa Sai, P. S. Kinetic studies on catalytic decomposition of methane to hydrogen and carbon over Ni/TiO₂ catalyst. *Ind. Eng. Chem. Res.* **2004**, *43* (16), 4864–4870.

(61) Zavarukhin, S. G.; Kuvshinov, G. G. The kinetic model of formation of nanofibrous carbon from CH₄-H₂ mixture over a high-loaded nickel catalyst with consideration for the catalyst deactivation. *Appl. Catal., A* **2004**, *272* (1), 219–227.

(62) Suelves, L.; Pinilla, J. L.; Lázaro, M. J.; Moliner, R.; Palacios, J. M. Effects of reaction conditions on hydrogen production and carbon nanofiber properties generated by methane decomposition in a fixed bed reactor using a NiCuAl catalyst. *J. Power Sources* **2009**, *192* (1), 35–42.

(63) Saraswat, S. K.; Sinha, B.; Pant, K. K.; Gupta, R. B. Kinetic study and modeling of homogeneous thermocatalytic decomposition of methane over a Ni-Cu-Zn/Al₂O₃ catalyst for the production of hydrogen and bamboo-shaped carbon nanotubes. *Ind. Eng. Chem. Res.* **2016**, *55* (45), 11672–11680.

(64) Alstrup, I.; Tavares, M. T. The kinetics of carbon formation from CH₄ + H₂ on a silica-supported nickel catalyst. *J. Catal.* **1992**, *135* (1), 147–155.

(65) Alstrup, I.; Tavares, M. T. Kinetics of carbon formation from CH₄ + H₂ on silica-supported nickel and Ni-Cu catalysts. *J. Catal.* **1993**, *139* (2), 513–524.

(66) Zadeh, J. S. M.; Smith, K. J. Kinetics of CH₄ decomposition on supported cobalt catalysts. *J. Catal.* **1998**, *176* (1), 115–124.

(67) Zhang, Y.; Smith, K. J. A kinetic model of CH₄ decomposition and filamentous carbon formation on supported Co catalysts. *J. Catal.* **2005**, *231* (2), 354–364.

(68) Muradov, N.; Smith, F.; T-Raissi, A. Catalytic activity of carbons for methane decomposition reaction. *Catal. Today* **2005**, *102–103*, 225–233.

(69) Serrano, D. P.; Botas, J. A.; Fierro, J. L. G.; Guil-López, R.; Pizarro, P.; Gómez, G. Hydrogen production by methane decomposition: Origin of the catalytic activity of carbon materials. *Fuel* **2010**, *89* (6), 1241–1248.

(70) Douven, S.; Pirard, S. L.; Heyen, G.; Toye, D.; Pirard, J.-P. Kinetic study of double-walled carbon nanotube synthesis by catalytic chemical vapour deposition over an Fe-Mo/MgO catalyst using methane as the carbon source. *Chem. Eng. J.* **2011**, *175*, 396–407.

(71) Yeheskel, J.; Epstein, M. Thermolysis of methane in a solar reactor for mass-production of hydrogen and carbon nano-materials. *Carbon* **2011**, *49* (14), 4695–4703.

(72) Yadav, M. D.; Dasgupta, K.; Patwardhan, A. W.; Kaushal, A.; Joshi, J. B. Kinetic study of single-walled carbon nanotube synthesis by thermocatalytic decomposition of methane using floating catalyst chemical vapour deposition. *Chem. Eng. Sci.* **2019**, *196*, 91–103.

(73) Yadav, M. D.; Patwardhan, A. W.; Joshi, J. B.; Dasgupta, K. Kinetic study of multi-walled carbon nanotube synthesis by thermocatalytic decomposition of methane using floating catalyst chemical vapour deposition. *Chem. Eng. J.* **2019**, *377*, 119895.

(74) Wang, J.; Li, X.; Zhou, Y.; Yu, G.; Jin, L.; Hu, H. Mechanism of methane decomposition with hydrogen addition over activated carbon via in-situ pyrolysis-electron impact ionization time-of-flight mass spectrometry. *Fuel* **2020**, *263*, 116734.

(75) Chen, Q.; Lua, A. C. Kinetic reaction and deactivation studies on thermocatalytic decomposition of methane by electroless nickel plating catalyst. *Chem. Eng. J.* **2020**, *389*, 124366.

(76) Ceyer, S. T.; Yang, Q. Y.; Lee, M. B.; Beckerle, J. D.; Johnson, A. D. In *Studies in Surface Science and Catalysis*; Bibby, D. M.; Chang, C. D.; Howe, R. F.; Yurchak, S., Eds.; Elsevier: Amsterdam, 1988.

(77) Lee, M. B.; Yang, Q. Y.; Tang, S. L.; Ceyer, S. T. Activated dissociative chemisorption of CH₄ on Ni(111): Observation of a methyl radical and implication for the pressure gap in catalysis. *J. Chem. Phys.* **1986**, *85* (3), 1693–1694.

(78) Lee, M. B.; Yang, Q. Y.; Ceyer, S. T. Dynamics of the activated dissociative chemisorption of CH₄ and implication for the pressure gap in catalysis: A molecular beam–high resolution electron energy loss study. *J. Chem. Phys.* **1987**, *87* (5), 2724–2741.

(79) Wagner, R. S.; Ellis, W. C. Vapor-Liquid-Solid mechanism of single crystal growth. *Appl. Phys. Lett.* **1964**, *4* (5), 89–90.

(80) Baker, R. T. K.; Barber, M. A.; Harris, P. S.; Feates, F. S.; Waite, R. J. Nucleation and growth of carbon deposits from the nickel catalyzed decomposition of acetylene. *J. Catal.* **1972**, *26* (1), 51–62.

(81) Baker, R. T. K. Catalytic growth of carbon filaments. *Carbon* **1989**, *27* (3), 315–323.

(82) Baker, R. T. K.; Harris, P. S.; Thomas, R. B.; Waite, R. J. Formation of filamentous carbon from iron, cobalt and chromium catalyzed decomposition of acetylene. *J. Catal.* **1973**, *30* (1), 86–95.

(83) Rostrup-Nielsen, J. R.; Trimm, D. L. Mechanisms of carbon formation on nickel-containing catalysts. *J. Catal.* **1977**, *48* (1), 155–165.

(84) Snoeck, J. W.; Froment, G. F.; Fowles, M. Filamentous carbon formation and gasification: Thermodynamics, driving force, nucleation, and steady-state growth. *J. Catal.* **1997**, *169* (1), 240–249.

(85) Klinke, C.; Bonard, J.-M.; Kern, K. Thermodynamic calculations on the catalytic growth of multiwall carbon nanotubes. *Phys. Rev. B: Condens. Matter Mater. Phys.* **2005**, *71* (3), 035403.

(86) Baird, T.; Fryer, J. R.; Grant, B. Carbon formation on iron and nickel foils by hydrocarbon pyrolysis—reactions at 700°C. *Carbon* **1974**, *12* (5), 591–602.

(87) Oberlin, A.; Endo, M.; Koyama, T. Filamentous growth of carbon through benzene decomposition. *J. Cryst. Growth* **1976**, *32* (3), 335–349.

(88) Helveg, S.; López-Cartes, C.; Sehested, J.; Hansen, P. L.; Clausen, B. S.; Rostrup-Nielsen, J. R.; Abild-Pedersen, F.; Nørskov, J. K. Atomic-scale imaging of carbon nanofibre growth. *Nature* **2004**, *427* (6973), 426–429.

(89) Hofmann, S.; Csányi, G.; Ferrari, A. C.; Payne, M. C.; Robertson, J. Surface diffusion: The low activation energy path for nanotube growth. *Phys. Rev. Lett.* **2005**, *95* (3), No. 036101, DOI: 10.1103/PhysRevLett.95.036101.

(90) Raty, J.-Y.; Gygi, F.; Galli, G. Growth of carbon nanotubes on metal nanoparticles: A microscopic mechanism from ab initio molecular dynamics simulations. *Phys. Rev. Lett.* **2005**, *95*, 096103.

(91) Rinaldi, A.; Tessonnier, J.-P.; Schuster, M. E.; Blume, R.; Girgsdies, F.; Zhang, Q.; Jacob, T.; Hamid, S. B. A.; Su, D. S.; Schlögl, R. Dissolved carbon controls the initial stages of nanocarbon growth. *Angew. Chem., Int. Ed.* **2011**, *50* (14), 3313–3317.

(92) Kumar, M. *Carbon nanotube synthesis and growth mechanism Carbon Nanotubes - Synthesis, Characterization, Applications*; IntechOpen: Rijeka, Croatia, 2011.

(93) Kutteri, D. A.; Wang, I.-W.; Samanta, A.; Li, L. L.; Hu, J. L. Methane decomposition to tip and base grown carbon nanotubes and CO_x-free H₂ over mono- and bimetallic 3d transition metal catalysts. *Catal. Sci. Technol.* **2018**, *8* (3), 858–869.

(94) Wang, I.-W.; Kutteri, D. A.; Gao, B. Y.; Tian, H. J.; Hu, J. L. Methane pyrolysis for carbon nanotubes and CO_x-Free H₂ over transition-metal catalysts. *Energy Fuels* **2019**, *33* (1), 197–205.

(95) Kharlamova, M. V. Investigation of growth dynamics of carbon nanotubes. *Beilstein J. Nanotechnol.* **2017**, *8*, 826–856.

(96) Chesnokov, V. V.; Buyanov, R. A. Mechanism for the formation of carbon deposits from benzene on iron and nickel. *Kinet. Catal.* **1987**, *28* (2), 353–357.

(97) Chesnokov, V. V.; Buyanov, R. A. The formation of carbon filaments upon decomposition of hydrocarbons catalysed by iron

subgroup metals and their alloys. *Russ. Chem. Rev.* **2000**, *69* (7), 623–638.

(98) Zaikovskii, V. I.; Chesnokov, V. V.; Buyanov, R. A. The relationship between the state of active species in a Ni/Al₂O₃ catalyst and the mechanism of growth of filamentous carbon. *Kinet. Catal.* **2001**, *42* (6), 813–820.

(99) Buyanov, R. A.; Chesnokov, V. V. On the processes that occur in the metal particles with their use in catalytic decomposition of hydrocarbons through the carbide cycle mechanism. *Chem. Sustainable Dev.* **2005**, *13*, 37–40.

(100) Ni, L.; Kuroda, K.; Zhou, L.-P.; Ohta, K.; Matsuishi, K.; Nakamura, J. Decomposition of metal carbides as an elementary step of carbon nanotube synthesis. *Carbon* **2009**, *47* (13), 3054–3062.

(101) Esconjauregui, S.; Whelan, C. M.; Maex, K. The reasons why metals catalyze the nucleation and growth of carbon nanotubes and other carbon nanomorphologies. *Carbon* **2009**, *47* (3), 659–669.

(102) Narkiewicz, U.; Podsiadly, M.; Jędrzejewski, R.; Pelech, I. Catalytic decomposition of hydrocarbons on cobalt, nickel and iron catalysts to obtain carbon nanomaterials. *Appl. Catal., A* **2010**, *384* (1), 27–35.

(103) Podsiadly, M.; Pelech, I.; Narkiewicz, U. Synthesis of nanocrystalline nickel and iron carbides by decomposition of hydrocarbons. *Mater. Sci.-Pol.* **2013**, *31* (1), 65–70.

(104) Wirth, C. T.; Hofmann, S.; Robertson, J. State of the catalyst during carbon nanotube growth. *Diamond Relat. Mater.* **2009**, *18* (5–8), 940–945.

(105) Weatherup, R. S.; Bayer, B. C.; Blume, R.; Ducati, C.; Baetz, C.; Schlögl, R.; Hofmann, S. In situ characterization of alloy catalysts for low-temperature graphene growth. *Nano Lett.* **2011**, *11* (10), 4154–4160.

(106) Weatherup, R. S.; Bayer, B. C.; Blume, R.; Baetz, C.; Kidambi, P. R.; Fouquet, M.; Wirth, C. T.; Schlögl, R.; Hofmann, S. On the mechanisms of Ni-catalysed graphene chemical vapour deposition. *ChemPhysChem* **2012**, *13* (10), 2544–2549.

(107) Alstrup, I. A new model explaining carbon filament growth on nickel, iron, and Ni-Cu alloy catalysts. *J. Catal.* **1988**, *109* (2), 241–251.

(108) Emmenegger, C.; Bonard, J. M.; Mauron, P.; Sudan, P.; Lepora, A.; Grobety, B.; Züttel, A.; Schlapbach, L. Synthesis of carbon nanotubes over Fe catalyst on aluminium and suggested growth mechanism. *Carbon* **2003**, *41* (3), 539–547.

(109) Pérez-Cabero, M.; Rodríguez-Ramos, I.; Guerrero-Ruñz, A. Characterization of carbon nanotubes and carbon nanofibers prepared by catalytic decomposition of acetylene in a fluidized bed reactor. *J. Catal.* **2003**, *215* (2), 305–316.

(110) Schaper, A. K.; Hou, H.; Greiner, A.; Philipp, F. The role of iron carbide in multiwalled carbon nanotube growth. *J. Catal.* **2004**, *222* (1), 250–254.

(111) Perez-Cabero, M.; Romeo, E.; Royo, C.; Monzon, A.; Guerrero-Ruiz, A.; Rodriguez-Ramos, I. Growing mechanism of CNTs: a kinetic approach. *J. Catal.* **2004**, *224* (1), 197–205.

(112) Nishimura, K.; Okazaki, N.; Pan, L.; Nakayama, Y. In situ study of iron catalysts for carbon nanotube growth using X-ray diffraction analysis. *Jpn. J. Appl. Phys.* **2004**, *43*, L471–L474.

(113) Yoshida, H.; Takeda, S.; Uchiyama, T.; Kohno, H.; Homma, Y. Atomic-scale in-situ observation of carbon nanotube growth from solid state iron carbide nanoparticles. *Nano Lett.* **2008**, *8* (7), 2082–2086.

(114) Philippe, R.; Caussat, B.; Falqui, A.; Kihn, Y.; Kalck, P.; Bordère, S.; Plee, D.; Gaillard, P.; Bernard, D.; Serp, P. An original growth mode of MWCNTs on alumina supported iron catalysts. *J. Catal.* **2009**, *263* (2), 345–358.

(115) Sharma, R.; Moore, E.; Rez, P.; Treacy, M. M. J. Site-specific fabrication of Fe particles for carbon nanotube growth. *Nano Lett.* **2009**, *9* (2), 689–694.

(116) He, Z.; Maurice, J.-L.; Gohier, A.; Lee, C. S.; Pribat, D.; Cojocaru, C. S. Iron catalysts for the growth of carbon nanofibers: Fe, Fe₃C or Both? *Chem. Mater.* **2011**, *23* (24), 5379–5387.

(117) Wirth, C. T.; Bayer, B. C.; Gamalski, A. D.; Esconjauregui, S.; Weatherup, R. S.; Ducati, C.; Baetz, C.; Robertson, J.; Hofmann, S. The phase of iron catalyst nanoparticles during carbon nanotube growth. *Chem. Mater.* **2012**, *24* (24), 4633–4640.

(118) Reddy Enakonda, L.; Zhou, L.; Saih, Y.; Ould-Chikh, S.; Lopatin, S.; Gary, D.; Del-Gallo, P.; Basset, J.-M. Methane-induced activation mechanism of fused ferric oxide–alumina catalysts during methane decomposition. *ChemSusChem* **2016**, *9* (15), 1911–1915.

(119) Zhou, L.; Enakonda, L. R.; Harb, M.; Saih, Y.; Aguilar-Tapia, A.; Ould-Chikh, S.; Hazemann, J.-L.; Li, J.; Wei, N.; Gary, D.; Del-Gallo, P.; Basset, J.-M. Fe catalysts for methane decomposition to produce hydrogen and carbon nano materials. *Appl. Catal., B* **2017**, *208*, 44–59.

(120) Hofmann, S.; Blume, R.; Wirth, C. T.; Cantoro, M.; Sharma, R.; Ducati, C.; Hävecker, M.; Zafeiratos, S.; Schnoerch, P.; Oestereich, A.; Teschner, D.; Albrecht, M.; Knop-Gericke, A.; Schlögl, R.; Robertson, J. State of transition metal catalysts during carbon nanotube growth. *J. Phys. Chem. C* **2009**, *113* (5), 1648–1656.

(121) Cooper, B. J.; Trimm, D. L. Carbon deposition from propylene on polycrystalline and single crystal iron. *J. Catal.* **1980**, *62* (1), 35–43.

(122) Amin, A. M.; Croiset, E.; Epling, W. Review of methane catalytic cracking for hydrogen production. *Int. J. Hydrogen Energy* **2011**, *36* (4), 2904–2935.

(123) Avdeeva, L. B.; Reshetenko, T. V.; Ismagilov, Z. R.; Likholobov, V. A. Iron-containing catalysts of methane decomposition: accumulation of filamentous carbon. *Appl. Catal., A* **2002**, *228* (1–2), 53–63.

(124) Bayat, N.; Rezaei, M.; Meshkani, F. CO_x-free hydrogen and carbon nanofibers production by methane decomposition over nickel-alumina catalysts. *Korean J. Chem. Eng.* **2016**, *33* (2), 490–499.

(125) Bayat, N.; Rezaei, M.; Meshkani, F. Hydrogen and carbon nanofibers synthesis by methane decomposition over Ni-Pd/Al₂O₃ catalyst. *Int. J. Hydrogen Energy* **2016**, *41* (12), 5494–5503.

(126) Fakeeha, A. H.; Ibrahim, A. A.; Khan, W. U.; Seshan, K.; Al-Otaibi, R. L.; Al-Fatesh, A. S. Hydrogen production via catalytic methane decomposition over alumina supported iron catalyst. *Arabian J. Chem.* **2018**, *11* (3), 405–414.

(127) Rastegarpanah, A.; Rezaei, M.; Meshkani, F.; Zhang, K. F.; Zhao, X. T.; Pei, W. B.; Liu, Y. X.; Deng, J. G.; Arandiyani, H.; Dai, H. X. Mesoporous Ni/MeO_x (Me = Al, Mg, Ti, and Si): Highly efficient catalysts in the decomposition of methane for hydrogen production. *Appl. Surf. Sci.* **2019**, *478*, 581–593.

(128) Torres, D.; Pinilla, J. L.; Suelves, I. Co-, Cu- and Fe-doped Ni/Al₂O₃ catalysts for the catalytic decomposition of methane into hydrogen and carbon nanofibers. *Catalysts* **2018**, *8* (8), 1–15.

(129) Serrano, D. P.; Botas, J. A.; Pizarro, P.; Gómez, G. Kinetic and autocatalytic effects during the hydrogen production by methane decomposition over carbonaceous catalysts. *Int. J. Hydrogen Energy* **2013**, *38* (14), 5671–5683.

(130) Bayat, N.; Rezaei, M.; Meshkani, F. Methane decomposition over Ni-Fe/Al₂O₃ catalysts for production of CO_x-free hydrogen and carbon nanofiber. *Int. J. Hydrogen Energy* **2016**, *41* (3), 1574–1584.

(131) Bayat, N.; Meshkani, F.; Rezaei, M. Thermocatalytic decomposition of methane to CO_x-free hydrogen and carbon over Ni-Fe-Cu/Al₂O₃ catalysts. *Int. J. Hydrogen Energy* **2016**, *41* (30), 13039–13049.

(132) Wang, D.; Zhang, J.; Sun, J. B.; Gao, W. M.; Cui, Y. B. Effect of metal additives on the catalytic performance of Ni/Al₂O₃ catalyst in thermocatalytic decomposition of methane. *Int. J. Hydrogen Energy* **2019**, *44* (14), 7205–7215.

(133) Silva, R. R. C. M.; Oliveira, H. A.; Guarino, A. C. P. F.; Toledo, B. B.; Moura, M. B. T.; Oliveira, B. T. M.; Passos, F. B. Effect of support on methane decomposition for hydrogen production over cobalt catalysts. *Int. J. Hydrogen Energy* **2016**, *41* (16), 6763–6772.

(134) Pudukudy, M.; Yaakob, Z. Methane decomposition over Ni, Co and Fe based monometallic catalysts supported on sol gel derived SiO₂ microflakes. *Chem. Eng. J.* **2015**, *262*, 1009–1021.

- (135) Ibrahim, A. A.; Al-Fatesh, A. S.; Khan, W. U.; Soliman, M. A.; Al-Otaibi, R. L.; Fakeeha, A. H. Thermo-catalytic methane decomposition: A review of state of the art of catalysts. *J. Chem. Soc. Pak.* **2015**, *37* (6), 1269–1297.
- (136) Al-Fatesh, A. S.; Amin, A.; Ibrahim, A. A.; Khan, W. U.; Soliman, M. A.; Al-Otaibi, R. L.; Fakeeha, A. H. Effect of Ce and Co addition to Fe/Al₂O₃ for catalytic methane decomposition. *Catalysts* **2016**, *6* (3), 15.
- (137) Al-Fatesh, A. S.; Fakeeha, A. H.; Khan, W. U.; Ibrahim, A. A.; He, S. B.; Seshan, K. Production of hydrogen by catalytic methane decomposition over alumina supported mono-, bi- and tri-metallic catalysts. *Int. J. Hydrogen Energy* **2016**, *41* (48), 22932–22940.
- (138) Al-Fatesh, A. S.; Barama, S.; Ibrahim, A. A.; Barama, A.; Khan, W. U.; Fakeeha, A. Study of methane decomposition on Fe/MgO-based catalyst modified by Ni, Co, and Mn additives. *Chem. Eng. Commun.* **2017**, *204* (7), 739–749.
- (139) Pudukudy, M.; Yaakob, Z.; Takriff, M. S. Methane decomposition into CO_x free hydrogen and multiwalled carbon nanotubes over ceria, zirconia and lanthana supported nickel catalysts prepared via a facile solid state citrate fusion method. *Energy Convers. Manage.* **2016**, *126*, 302–315.
- (140) Awadallah, A. E.; Solyman, S. M.; Aboul-Enein, A. A.; Ahmed, H. A.; Aboul-Gheit, N. A. K.; Hassan, S. A. Effect of combining Al, Mg, Ce or La oxides to extracted rice husk nanosilica on the catalytic performance of NiO during CO_x-free hydrogen production via methane decomposition. *Int. J. Hydrogen Energy* **2017**, *42* (15), 9858–9872.
- (141) Pudukudy, M.; Yaakob, Z.; Jia, Q. M.; Takriff, M. S. Catalytic decomposition of methane over rare earth metal (Ce and La) oxides supported iron catalysts. *Appl. Surf. Sci.* **2019**, *467*, 236–248.
- (142) Ermakova, M. A.; Ermakov, D. Y. Ni/SiO₂ and Fe/SiO₂ catalysts for production of hydrogen and filamentous carbon via methane decomposition. *Catal. Today* **2002**, *77* (3), 225–235.
- (143) Ouyang, M. Z.; Boldrin, P.; Maher, R. C.; Chen, X. L.; Liu, X. H.; Cohen, L. F.; Brandon, N. P. A mechanistic study of the interactions between methane and nickel supported on doped ceria. *Appl. Catal., B* **2019**, *248*, 332–340.
- (144) Guil-López, R.; Botas, J. A.; Fierro, J. L. G.; Serrano, D. P. Comparison of metal and carbon catalysts for hydrogen production by methane decomposition. *Appl. Catal., A* **2011**, *396* (1–2), 40–51.
- (145) Li, J. M.; Zhao, L. J.; He, J. C.; Dong, L.; Xiong, L. P.; Du, Y.; Yang, Y.; Wang, H. Y.; Peng, S. M. Methane decomposition over high-loaded Ni-Cu-SiO₂ catalysts. *Fusion Eng. Des.* **2016**, *113*, 279–287.
- (146) Berndt, F. M.; Perez-Lopez, O. W. Catalytic decomposition of methane over Ni/SiO₂: influence of Cu addition. *React. Kinet., Mech. Catal.* **2017**, *120* (1), 181–193.
- (147) Al-Fatesh, A. S.; Fakeeha, A. H.; Ibrahim, A. A.; Khan, W. U.; Atia, H.; Eckelt, R.; Seshan, K.; Chowdhury, B. Decomposition of methane over alumina supported Fe and Ni-Fe bimetallic catalyst: Effect of preparation procedure and calcination temperature. *J. Saudi Chem. Soc.* **2018**, *22* (2), 239–247.
- (148) Rastegarpanah, A.; Rezaei, M.; Meshkani, F.; Zhang, K. F.; Zhao, X. T.; Pei, W. B.; Liu, Y. X.; Deng, J. G.; Arandiyani, H.; Dai, H. X. Influence of group VIB metals on activity of the Ni/MgO catalysts for methane decomposition. *Appl. Catal., B* **2019**, *248*, 515–525.
- (149) Pudukudy, M.; Yaakob, Z.; Mazuki, M. Z.; Takriff, M. S.; Jahaya, S. S. One-pot sol-gel synthesis of MgO nanoparticles supported nickel and iron catalysts for undiluted methane decomposition into CO_x free hydrogen and nanocarbon. *Appl. Catal., B* **2017**, *218*, 298–316.
- (150) Takenaka, S.; Ogihara, H.; Yamanaka, I.; Otsuka, K. Decomposition of methane over supported-Ni catalysts: effects of the supports on the catalytic lifetime. *Appl. Catal., A* **2001**, *217* (1–2), 101–110.
- (151) Takenaka, S.; Shigeta, Y.; Tanabe, E.; Otsuka, K. Methane decomposition into hydrogen and carbon nanofibers over supported Pd-Ni catalysts. *J. Catal.* **2003**, *220* (2), 468–477.
- (152) Garcia-Sancho, C.; Guil-López, R.; Sebastian-Lopez, A.; Navarro, R. M.; Fierro, J. L. G. Hydrogen production by methane decomposition: A comparative study of supported and bulk ex-hydrocalcite mixed oxide catalysts with Ni, Mg and Al. *Int. J. Hydrogen Energy* **2018**, *43* (20), 9607–9621.
- (153) Awadallah, A. E.; Mostafa, M. S.; Aboul-Enein, A. A.; Hanafi, S. A. Hydrogen production via methane decomposition over Al₂O₃-TiO₂ binary oxides supported Ni catalysts: Effect of Ti content on the catalytic efficiency. *Fuel* **2014**, *129*, 68–77.
- (154) Ahmed, W.; Awadallah, A. E.; Aboul-Enein, A. A. Ni/CeO₂-Al₂O₃ catalysts for methane thermo-catalytic decomposition to CO_x-free H₂ production. *Int. J. Hydrogen Energy* **2016**, *41* (41), 18484–18493.
- (155) Li, Y.; Li, D.; Wang, G. Methane decomposition to CO_x-free hydrogen and nano-carbon material on group 8–10 base metal catalysts: A review. *Catal. Today* **2011**, *162* (1), 1–48.
- (156) Naresh, G.; Kumar, V. V.; Anjaneyulu, C.; Tardio, J.; Bhargava, S. K.; Patel, J.; Venugopal, A. Nano size H beta zeolite as an effective support for Ni and Ni-Cu for CO_x free hydrogen production by catalytic decomposition of methane. *Int. J. Hydrogen Energy* **2016**, *41* (44), 19855–19862.
- (157) Shen, Y.; Lua, A. C. Synthesis of Ni and Ni-Cu supported on carbon nanotubes for hydrogen and carbon production by catalytic decomposition of methane. *Appl. Catal., B* **2015**, *164*, 61–69.
- (158) Torres, D.; Pinilla, J. L.; Suelves, I. Screening of Ni-Cu bimetallic catalysts for hydrogen and carbon nanofilaments production via catalytic decomposition of methane. *Appl. Catal., A* **2018**, *559*, 10–19.
- (159) Rai, R. K.; Gupta, K.; Tyagi, D.; Mahata, A.; Behrens, S.; Yang, X.; Xu, Q.; Pathak, B.; Singh, S. K. Access to highly active Ni-Pd bimetallic nanoparticle catalysts for C-C coupling reactions. *Catal. Sci. Technol.* **2016**, *6* (14), 5567–5579.
- (160) Huynh, T.-T.; Tsai, M.-C.; Pan, C.-J.; Su, W.-N.; Chan, T.-S.; Lee, J.-F.; Hwang, B.-J. Synergetic electrocatalytic activities towards hydrogen peroxide: Understanding the ordered structure of PdNi bimetallic nanocatalysts. *Electrochem. Commun.* **2019**, *101*, 93–98.
- (161) Miao, C.; Zhou, G.; Chen, S.; Xie, H.; Zhang, X. Synergistic effects between Cu and Ni species in NiCu/γ-Al₂O₃ catalysts for hydrodeoxygenation of methyl laurate. *Renewable Energy* **2020**, *153*, 1439–1454.
- (162) Wang, H. Y.; Lua, A. C. Methane decomposition using Ni-Cu alloy nano-particle catalysts and catalyst deactivation studies. *Chem. Eng. J.* **2015**, *262*, 1077–1089.
- (163) Echevoyen, Y.; Suelves, I.; Lázaro, M. J.; Moliner, R.; Palacios, J. M. Hydrogen production by thermocatalytic decomposition of methane over Ni-Al and Ni-Cu-Al catalysts: Effect of calcination temperature. *J. Power Sources* **2007**, *169* (1), 150–157.
- (164) Saraswat, S. K.; Pant, K. K. Ni-Cu-Zn/MCM-22 catalysts for simultaneous production of hydrogen and multiwall carbon nanotubes via thermo-catalytic decomposition of methane. *Int. J. Hydrogen Energy* **2011**, *36* (21), 13352–13360.
- (165) Pudukudy, M.; Yaakob, Z.; Akmal, Z. S. Direct decomposition of methane over Pd promoted Ni/SBA-15 catalysts. *Appl. Surf. Sci.* **2015**, *353*, 127–136.
- (166) Pudukudy, M.; Yaakob, Z.; Takriff, M. S. Methane decomposition over Pd promoted Ni/MgAl₂O₄ catalysts for the production of CO_x free hydrogen and multiwalled carbon nanotubes. *Appl. Surf. Sci.* **2015**, *356*, 1320–1326.
- (167) Rastegarpanah, A.; Meshkani, F.; Rezaei, M. Thermocatalytic decomposition of methane over mesoporous nanocrystalline promoted Ni/MgO-Al₂O₃ catalysts. *Int. J. Hydrogen Energy* **2017**, *42* (26), 16476–16488.
- (168) Ashok, J.; Reddy, P. S.; Raju, G.; Subrahmanyam, M.; Venugopal, A. Catalytic decomposition of methane to hydrogen and carbon nanofibers over Ni-Cu-SiO₂ catalysts. *Energy Fuels* **2009**, *23* (1), 5–13.
- (169) Wang, J. F.; Jin, L. J.; Li, Y.; Hu, H. Q. Preparation of Fe-doped carbon catalyst for methane decomposition to hydrogen. *Ind. Eng. Chem. Res.* **2017**, *56* (39), 11021–11027.
- (170) Ibrahim, A. A.; Fakeeha, A. H.; Al-Fatesh, A. S.; Abasaheed, A. E.; Khan, W. U. Methane decomposition over iron catalyst for

hydrogen production. *Int. J. Hydrogen Energy* **2015**, *40* (24), 7593–7600.

(171) Cunha, A. F.; Orfão, J. J. M.; Figueiredo, J. L. Methane decomposition on Fe-Cu Raney-type catalysts. *Fuel Process. Technol.* **2009**, *90* (10), 1234–1240.

(172) Al-Fatesh, A. S.; Abu-Dahrieh, J.; Ibrahim, A. A.; Fakeeha, A. H.; Khan, W. U. Coproduction of hydrogen and carbon filaments from methane decomposition over Fe/La₂O₃ Catalysts. *J. Chem. Soc. Pak.* **2016**, *38* (6), 1104–1111.

(173) Al-Fatesh, A. S.; Fakeeha, A. H.; Ibrahim, A. A.; Khan, W. U.; Atia, H.; Eckelt, R.; Chowdhury, B. Iron oxide supported on Al₂O₃ catalyst for methane decomposition reaction: Effect of MgO additive and calcination Temperature. *J. Chin. Chem. Soc.* **2016**, *63* (2), 205–212.

(174) Zhou, L.; Enakonda, L. R.; Saih, Y.; Loptain, S.; Gary, D.; Del-Gallo, P.; Basset, J.-M. Catalytic methane decomposition over Fe-Al₂O₃. *ChemSusChem* **2016**, *9* (11), 1243–1248.

(175) Zhou, L.; Enakonda, L. R.; Li, S.; Gary, D.; Del-Gallo, P.; Mennemann, C.; Basset, J.-M. Iron ore catalysts for methane decomposition to make CO_x free hydrogen and carbon nano material. *J. Taiwan Inst. Chem. Eng.* **2018**, *87*, 54–63.

(176) Sánchez-Bastardo, N.; Schlögl, R.; Ruland, H. Methane pyrolysis for CO₂-free H₂ production: A green process to overcome renewable energies unsteadiness. *Chem. Ing. Tech.* **2020**, *92* (10), 1596–1609.

(177) Shah, N.; Pattanaik, S.; Huggins, F. E.; Panjala, D.; Huffman, G. P. XAFS and Mössbauer spectroscopy characterization of supported binary catalysts for nonoxidative dehydrogenation of methane. *Fuel Process. Technol.* **2003**, *83* (1), 163–173.

(178) Punnoose, A.; Shah, N.; Huffman, G. P.; Seehra, M. S. X-ray diffraction and electron magnetic resonance studies of M/Fe/Al₂O₃ (M = Ni, Mo and Pd) catalysts for CH₄ to H₂ conversion. *Fuel Process. Technol.* **2003**, *83* (1), 263–273.

(179) Awadallah, A. E.; Aboul-Enein, A. A.; Azab, M. A.; Abdel-Monem, Y. K. Influence of Mo or Cu doping in Fe/MgO catalyst for synthesis of single-walled carbon nanotubes by catalytic chemical vapor deposition of methane. *Fullerenes, Nanotubes, Carbon Nanostruct.* **2017**, *25* (4), 256–264.

(180) Fakeeha, A. H.; Al-Fatesh, A. S.; Chowdhury, B.; Ibrahim, A. A.; Khan, W. U.; Hassan, S.; Sasudeen, K.; Abasaeed, A. E. Bi-metallic catalysts of mesoporous Al₂O₃ supported on Fe, Ni and Mn for methane decomposition: Effect of activation temperature. *Chin. J. Chem. Eng.* **2018**, *26* (9), 1904–1911.

(181) Pinilla, J. L.; Utrilla, R.; Karn, R. K.; Suelves, I.; Lázaro, M. J.; Moliner, R.; García, A. B.; Rouzaud, J. N. High temperature iron-based catalysts for hydrogen and nanostructured carbon production by methane decomposition. *Int. J. Hydrogen Energy* **2011**, *36* (13), 7832–7843.

(182) Ramasubramanian, V.; Ramsurn, H.; Price, G. L. Hydrogen production by catalytic decomposition of methane over Fe based bi-metallic catalysts supported on CeO₂-ZrO₂. *Int. J. Hydrogen Energy* **2020**, *45* (21), 12026–12036.

(183) Calafat, A.; Sanchez, N. Production of carbon nanotubes through combination of catalyst reduction and methane decomposition over Fe-Ni/ZrO₂ catalysts prepared by the citrate method. *Appl. Catal., A* **2016**, *528*, 14–23.

(184) Tang, L.; Yamaguchi, D.; Burke, N.; Trimm, D.; Chiang, K. Methane decomposition over ceria modified iron catalysts. *Catal. Commun.* **2010**, *11* (15), 1215–1219.

(185) Barreiro, A.; Hampel, S.; Rümmeli, M. H.; Kramberger, C.; Grüneis, A.; Biedermann, K.; Leonhardt, A.; Gemming, T.; Büchner, B.; Bachtold, A.; Pichler, T. Thermal decomposition of ferrocene as a method for production of single-walled carbon nanotubes without additional carbon sources. *J. Phys. Chem. B* **2006**, *110* (42), 20973–20977.

(186) Huang, G.; Weng, J. Syntheses of carbon nanomaterials by ferrocene. *Curr. Org. Chem.* **2011**, *15* (21), 3653–3666.

(187) Rao, C. N. R.; Sen, R.; Satishkumar, B. C.; Govindaraj, A. Large aligned-nanotube bundles from ferrocene pyrolysis. *Chem. Commun.* **1998**, *15*, 1525–1526.

(188) Satishkumar, B. C.; Govindaraj, A.; Rao, C. N. R. Bundles of aligned carbon nanotubes obtained by the pyrolysis of ferrocene-hydrocarbon mixtures: role of the metal nanoparticles produced in situ. *Chem. Phys. Lett.* **1999**, *307* (3), 158–162.

(189) Rao, C. N. R.; Govindaraj, A. Carbon nanotubes from organometallic precursors. *Acc. Chem. Res.* **2002**, *35* (12), 998–1007.

(190) Leonhardt, A.; Ritschel, M.; Elefant, D.; Mattern, N.; Biedermann, K.; Hampel, S.; Müller, C.; Gemming, T.; Büchner, B. Enhanced magnetism in Fe-filled carbon nanotubes produced by pyrolysis of ferrocene. *J. Appl. Phys.* **2005**, *98* (7), 074315.

(191) Zhang, T. J.; Amiridis, M. D. Hydrogen production via the direct cracking of methane over silica-supported nickel catalysts. *Appl. Catal., A* **1998**, *167* (2), 161–172.

(192) Villacampa, J. I.; Royo, C.; Romeo, E.; Montoya, J. A.; Del Angel, P.; Monzón, A. Catalytic decomposition of methane over Ni-Al₂O₃ coprecipitated catalysts: Reaction and regeneration studies. *Appl. Catal., A* **2003**, *252* (2), 363–383.

(193) Otsuka, K.; Takenaka, S.; Ohtsuki, H. Production of pure hydrogen by cyclic decomposition of methane and oxidative elimination of carbon nanofibers on supported-Ni-based catalysts. *Appl. Catal., A* **2004**, *273* (1), 113–124.

(194) Rahman, M. S.; Croiset, E.; Hudgins, R. R. Catalytic decomposition of methane for hydrogen production. *Top. Catal.* **2006**, *37* (2), 137–145.

(195) Ammendola, P.; Chirone, R.; Ruoppolo, G.; Russo, G. Regeneration strategies of deactivated catalysts for thermo-catalytic decomposition process in a fluidized bed reactor. *Combust. Sci. Technol.* **2008**, *180* (5), 869–882.

(196) Li, J.; Smith, K. J. Methane decomposition and catalyst regeneration in a cyclic mode over supported Co and Ni catalysts. *Appl. Catal., A* **2008**, *349* (1), 116–124.

(197) Saraswat, S. K.; Pant, K. K. Synthesis of hydrogen and carbon nanotubes over copper promoted Ni/SiO₂ catalyst by thermocatalytic decomposition of methane. *J. Nat. Gas Sci. Eng.* **2013**, *13*, 52–59.

(198) Aiello, R.; Fiscus, J. E.; zur Loye, H.-C.; Amiridis, M. D. Hydrogen production via the direct cracking of methane over Ni/SiO₂ catalyst deactivation and regeneration. *Appl. Catal., A* **2000**, *192* (2), 227–234.

(199) Choudhary, V. R.; Banerjee, S.; Rajput, A. M. Continuous production of H₂ at low temperature from methane decomposition over Ni-containing catalyst followed by gasification by steam of the carbon on the catalyst in two parallel reactors operated in cyclic manner. *J. Catal.* **2001**, *198* (1), 136–141.

(200) Takenaka, S.; Tomikubo, Y.; Kato, E.; Otsuka, K. Sequential production of H₂ and CO over supported Ni catalysts. *Fuel* **2004**, *83* (1), 47–57.

(201) Al-Hassani, A. A.; Abbas, H. F.; Daud, W. M. A. W. Production of CO_x-free hydrogen by the thermal decomposition of methane over activated carbon: Catalyst deactivation. *Int. J. Hydrogen Energy* **2014**, *39* (27), 14783–14791.

(202) Muradov, N. Z. CO₂-free production of hydrogen by catalytic pyrolysis of hydrocarbon fuel. *Energy Fuels* **1998**, *12* (1), 41–48.

(203) Muradov, N. Catalysis of methane decomposition over elemental carbon. *Catal. Commun.* **2001**, *2* (3–4), 89–94.

(204) Muradov, N. Hydrogen via methane decomposition: An application for decarbonization of fossil fuels. *Int. J. Hydrogen Energy* **2001**, *26* (11), 1165–1175.

(205) Ryu, B. H.; Lee, S. Y.; Lee, D. H.; Han, G. Y.; Lee, T.-J.; Yoon, K. J. Catalytic characteristics of various rubber-reinforcing carbon blacks in decomposition of methane for hydrogen production. *Catal. Today* **2007**, *123* (1–4), 303–309.

(206) Suelves, I.; Lázaro, M. J.; Moliner, R.; Pinilla, J. L.; Cubero, H. Hydrogen production by methane decarbonization: Carbonaceous catalysts. *Int. J. Hydrogen Energy* **2007**, *32* (15), 3320–3326.

(207) Serrano, D. P.; Botas, J. A.; Pizarro, P.; Guil-López, R.; Gómez, G. Ordered mesoporous carbons as highly active catalysts for

hydrogen production by CH₄ decomposition. *Chem. Commun.* **2008**, 48, 6585–6587.

(208) Suelves, I.; Pinilla, J. L.; Lázaro, M. J.; Moliner, R. Carbonaceous materials as catalysts for decomposition of methane. *Chem. Eng. J.* **2008**, *140* (1–3), 432–438.

(209) Botas, J. A.; Serrano, D. P.; Guil-López, R.; Pizarro, P.; Gómez, G. Methane catalytic decomposition over ordered mesoporous carbons: A promising route for hydrogen production. *Int. J. Hydrogen Energy* **2010**, *35* (18), 9788–9794.

(210) Ghani, S. A.; Al Saraj, M. A. A.; Razaq, G. H. A. Catalytic production of CO_x free hydrogen by methane decomposition over activated carbons. *Energy Sources, Part A* **2015**, *37* (3), 326–333.

(211) Nishii, H.; Miyamoto, D.; Umeda, Y.; Hamaguchi, H.; Suzuki, M.; Tanimoto, T.; Harigai, T.; Takikawa, H.; Suda, Y. Catalytic activity of several carbons with different structures for methane decomposition and by-produced carbons. *Appl. Surf. Sci.* **2019**, *473*, 291–297.

(212) Serrano, D. P.; Botas, J. A.; Guil-López, R. H₂ production from methane pyrolysis over commercial carbon catalysts: Kinetic and deactivation study. *Int. J. Hydrogen Energy* **2009**, *34* (10), 4488–4494.

(213) Wang, H. Y.; Lua, A. C. Hydrogen production by thermocatalytic methane decomposition. *Heat Transfer Eng.* **2013**, *34* (11–12), 896–903.

(214) Krzyżyński, S.; Kozłowski, M. Activated carbons as catalysts for hydrogen production via methane decomposition. *Int. J. Hydrogen Energy* **2008**, *33* (21), 6172–6177.

(215) Muradov, N. *Thermocatalytic CO₂-free production of hydrogen from hydrocarbon fuels Proceedings of the 2000 Hydrogen Program Review*; NREL/CP-570–28890, National Renewable Energy Laboratory: Golden CO, 2000.

(216) Bai, Z. Q.; Chen, H. K.; Li, W.; Li, B. Q. Hydrogen production by methane decomposition over coal char. *Int. J. Hydrogen Energy* **2006**, *31* (7), 899–905.

(217) Moliner, R.; Suelves, I.; Lázaro, M. J.; Moreno, O. Thermocatalytic decomposition of methane over activated carbons: influence of textural properties and surface chemistry. *Int. J. Hydrogen Energy* **2005**, *30* (3), 293–300.

(218) Pinilla, J. L.; Suelves, I.; Utrilla, R.; Gálvez, M. E.; Lázaro, M. J.; Moliner, R. Hydrogen production by thermo-catalytic decomposition of methane: Regeneration of active carbons using CO₂. *J. Power Sources* **2007**, *169* (1), 103–109.

(219) Pinilla, J. L.; Suelves, I.; Lázaro, M. J.; Moliner, R. Kinetic study of the thermal decomposition of methane using carbonaceous catalysts. *Chem. Eng. J.* **2008**, *138* (1), 301–306.

(220) Bai, Z. Q.; Chen, H.; Li, B. Q.; Li, W. Catalytic decomposition of methane over activated carbon. *J. Anal. Appl. Pyrolysis* **2005**, *73* (2), 335–341.

(221) Lázaro, M. J.; Pinilla, J. L.; Suelves, I.; Moliner, R. Study of the deactivation mechanism of carbon blacks used in methane decomposition. *Int. J. Hydrogen Energy* **2008**, *33* (15), 4104–4111.

(222) Sun, Z.-Q.; Wu, J.-H.; Haghghi, M.; Bromly, J.; Ng, E.; Wee, H. L.; Wang, Y.; Zhang, D.-K. Methane cracking over a bituminous coal char. *Energy Fuels* **2007**, *21* (3), 1601–1605.

(223) Abbas, H. F.; Daud, W. M. A. W. Thermocatalytic decomposition of methane for hydrogen production using activated carbon catalyst: Regeneration and characterization studies. *Int. J. Hydrogen Energy* **2009**, *34* (19), 8034–8045.

(224) Abbas, H. F.; Daud, W. M. A. W. An experimental investigation into the CO₂ gasification of deactivated activated-carbon catalyst used for methane decomposition to produce hydrogen. *Int. J. Hydrogen Energy* **2010**, *35* (1), 141–150.

(225) Muradov, N.; Chen, Z.; Smith, F. Fossil hydrogen with reduced CO₂ emission: Modeling thermocatalytic decomposition of methane in a fluidized bed of carbon particles. *Int. J. Hydrogen Energy* **2005**, *30* (10), 1149–1158.

(226) Dufour, A.; Celzard, A.; Fierro, V.; Broust, F.; Courson, C.; Zoulalian, A.; Rouzaud, J. N. Catalytic conversion of methane over a biomass char for hydrogen production: deactivation and regeneration by steam gasification. *Appl. Catal., A* **2015**, *490*, 170–180.

(227) Malaika, A.; Kozłowski, M. Influence of ethylene on carbon-catalysed decomposition of methane. *Int. J. Hydrogen Energy* **2009**, *34* (6), 2600–2605.

(228) Malaika, A.; Kozłowski, M. Hydrogen production by propylene-assisted decomposition of methane over activated carbon catalysts. *Int. J. Hydrogen Energy* **2010**, *35* (19), 10302–10310.

(229) Malaika, A.; Krzyżynska, B.; Kozłowski, M. Catalytic decomposition of methane in the presence of in situ obtained ethylene as a method of hydrogen production. *Int. J. Hydrogen Energy* **2010**, *35* (14), 7470–7475.

(230) Adamska, A.; Malaika, A.; Kozłowski, M. Carbon-catalysed decomposition of methane in the presence of carbon dioxide. *Energy Fuels* **2010**, *24* (6), 3307–3312.

(231) Rechnia, P.; Malaika, A.; Krzyżynska, B.; Kozłowski, M. Decomposition of methane in the presence of ethanol over activated carbon catalyst. *Int. J. Hydrogen Energy* **2012**, *37* (19), 14178–14186.

(232) Rechnia, P.; Malaika, A.; Najder-Kozdrowska, L.; Kozłowski, M. The effect of ethanol on carbon-catalysed decomposition of methane. *Int. J. Hydrogen Energy* **2012**, *37* (9), 7512–7520.

(233) Ogihara, H.; Tajima, H.; Kurokawa, H. Pyrolysis of mixtures of methane and ethane: activation of methane with the aid of radicals generated from ethane. *React. Chem. Eng.* **2020**, *5* (1), 145–153.

(234) Bai, Z. Q.; Chen, H. K.; Li, B. Q.; Li, W. Methane decomposition over Ni loaded activated carbon for hydrogen production and the formation of filamentous carbon. *Int. J. Hydrogen Energy* **2007**, *32* (1), 32–37.

(235) Pinilla, J. L.; Suelves, I.; Lázaro, M. J.; Moliner, R.; Palacios, J. M. Parametric study of the decomposition of methane using a NiCu/Al₂O₃ catalyst in a fluidized bed reactor. *Int. J. Hydrogen Energy* **2010**, *35* (18), 9801–9809.

(236) Szymańska, M.; Malaika, A.; Rechnia, P.; Miklaszewska, A.; Kozłowski, M. Metal/activated carbon systems as catalysts of methane decomposition reaction. *Catal. Today* **2015**, *249*, 94–102.

(237) Nasir Uddin, M.; Wan Daud, W.M.A.; Abbas, H. F. Co-production of hydrogen and carbon nanofibers from methane decomposition over zeolite Y supported Ni catalysts. *Energy Convers. Manage.* **2015**, *90*, 218–229.

(238) Pudukudy, M.; Yaakob, Z.; Takriff, M. S. Methane decomposition over unsupported mesoporous nickel ferrites: effect of reaction temperature on the catalytic activity and properties of the produced nanocarbon. *RSC Adv.* **2016**, *6* (72), 68081–68091.

(239) Salipira, K.; Coville, N. J.; Scurrell, M. S. Carbon produced by the catalytic decomposition of methane on nickel: Carbon yields and carbon structure as a function of catalyst properties. *J. Nat. Gas Sci. Eng.* **2016**, *32*, 501–511.

(240) Ashik, U.P.M.; Wan Daud, W.M.A.; Abbas, H. F. Methane decomposition kinetics and reaction rate over Ni/SiO₂ nanocatalyst produced through co-precipitation cum modified Stober method. *Int. J. Hydrogen Energy* **2017**, *42* (2), 938–952.

(241) Urdiana, G.; Valdez, R.; Lastra, G.; Valenzuela, M. Á.; Olivas, A. Production of hydrogen and carbon nanomaterials using transition metal catalysts through methane decomposition. *Mater. Lett.* **2018**, *217*, 9–12.

(242) Abbas, H. F.; Daud, W. M. A. W. Deactivation of palm shell-based activated carbon catalyst used for hydrogen production by thermocatalytic decomposition of methane. *Int. J. Hydrogen Energy* **2009**, *34* (15), 6231–6241.

(243) Abbas, H. F.; Baker, I. F. Thermocatalytic decomposition of methane using activated carbon: Studying the influence of process parameters using factorial design. *Int. J. Hydrogen Energy* **2011**, *36* (15), 8985–8993.

(244) Shilapuram, V.; Ozalp, N.; Oschatz, M.; Borchardt, L.; Kaskel, S. Hydrogen production from catalytic decomposition of methane over ordered mesoporous carbons (CMK-3) and carbide-derived carbon (DUT-19). *Carbon* **2014**, *67*, 377–389.

(245) Fakeeha, A. H.; Khan, W. U.; Al-Fatesh, A. S.; Abasaheed, A. E.; Naem, M. A. Production of hydrogen and carbon nanofibers from methane over Ni-Co-Al catalysts. *Int. J. Hydrogen Energy* **2015**, *40* (4), 1774–1781.

- (246) Pudukudy, M.; Yaakob, Z.; Kadier, A.; Takriff, M. S.; Hassan, N. S. M. One-pot sol-gel synthesis of Ni/TiO₂ catalysts for methane decomposition into CO_x free hydrogen and multiwalled carbon nanotubes. *Int. J. Hydrogen Energy* **2017**, *42* (26), 16495–16513.
- (247) Rastegarpanah, A.; Meshkani, F.; Rezaei, M. CO_x-free hydrogen and carbon nanofibers production by thermocatalytic decomposition of methane over mesoporous MgO·Al₂O₃ nanopowder-supported nickel catalysts. *Fuel Process. Technol.* **2017**, *167*, 250–262.
- (248) Tezel, E.; Figen, H. E.; Baykara, S. Z. Hydrogen production by methane decomposition using bimetallic Ni-Fe catalysts. *Int. J. Hydrogen Energy* **2019**, *44*, 9930–9940.
- (249) Zhang, W.; Ge, Q. J.; Xu, H. Y. Influences of reaction conditions on methane decomposition over non-supported Ni catalyst. *J. Nat. Gas Chem.* **2011**, *20* (4), 339–344.
- (250) Pinilla, J. L.; Suelves, I.; Lázaro, M. J.; Moliner, R. Influence on hydrogen production of the minor components of natural gas during its decomposition using carbonaceous catalysts. *J. Power Sources* **2009**, *192* (1), 100–106.
- (251) Fidalgo, B.; Muradov, N.; Menéndez, J. A. Effect of H₂S on carbon-catalyzed methane decomposition and CO₂ reforming reactions. *Int. J. Hydrogen Energy* **2012**, *37* (19), 14187–14194.
- (252) Munera Parra, A. A., Reactor design, modeling and optimization for the high-temperature methane pyrolysis and the reverse water-gas shift reaction. Ph.D, Thesis Fakultät Bio- und Chemieingenieurwesen der Technischen Universität: Dortmund, 2018.
- (253) Serban, M.; Lewis, M. A.; Marshall, C. L.; Doctor, R. D. Hydrogen production by direct contact pyrolysis of natural gas. *Energy Fuels* **2003**, *17* (3), 705–713.
- (254) Geißler, T.; Plevan, M.; Abánades, A.; Heinzl, A.; Mehravarán, K.; Rathnam, R. K.; Rubbia, C.; Salmieri, D.; Stoppel, L.; Stückrad, S.; Weisenburger, A.; Wenninger, H.; Wetzl, T. Experimental investigation and thermo-chemical modeling of methane pyrolysis in a liquid metal bubble column reactor with a packed bed. *Int. J. Hydrogen Energy* **2015**, *40* (41), 14134–14146.
- (255) Plevan, M.; Geißler, T.; Abánades, A.; Mehravarán, K.; Rathnam, R. K.; Rubbia, C.; Salmieri, D.; Stoppel, L.; Stückrad, S.; Wetzl, T. Thermal cracking of methane in a liquid metal bubble column reactor: Experiments and kinetic analysis. *Int. J. Hydrogen Energy* **2015**, *40* (25), 8020–8033.
- (256) Geißler, T.; Abánades, A.; Heinzl, A.; Mehravarán, K.; Müller, G.; Rathnam, R. K.; Rubbia, C.; Salmieri, D.; Stoppel, L.; Stückrad, S.; Weisenburger, A.; Wenninger, H.; Wetzl, T. Hydrogen production via methane pyrolysis in a liquid metal bubble column reactor with a packed bed. *Chem. Eng. J.* **2016**, *299*, 192–200.
- (257) Abánades, A.; Rathnam, R. K.; Geißler, T.; Heinzl, A.; Mehravarán, K.; Müller, G.; Plevan, M.; Rubbia, C.; Salmieri, D.; Stoppel, L.; Stückrad, S.; Weisenburger, A.; Wenninger, H.; Wetzl, T. Development of methane decarbonisation based on liquid metal technology for CO₂-free production of hydrogen. *Int. J. Hydrogen Energy* **2016**, *41* (19), 8159–8167.
- (258) Upham, D. C.; Agarwal, V.; Khechfe, A.; Snodgrass, Z. R.; Gordon, M. J.; Metiu, H.; McFarland, E. W. Catalytic molten metals for the direct conversion of methane to hydrogen and separable carbon. *Science* **2017**, *358* (6365), 917–920.
- (259) Munera Parra, A. A.; Agar, D. W. Molten metal capillary reactor for the high-temperature pyrolysis of methane. *Int. J. Hydrogen Energy* **2017**, *42* (19), 13641–13648.
- (260) Kang, D.; Rahimi, N.; Gordon, M. J.; Metiu, H.; McFarland, E. W. Catalytic methane pyrolysis in molten MnCl₂-KCl. *Appl. Catal., B* **2019**, *254*, 659–666.
- (261) Rahimi, N.; Kang, D.; Gelinas, J.; Menon, A.; Gordon, M. J.; Metiu, H.; McFarland, E. W. Solid carbon production and recovery from high temperature methane pyrolysis in bubble columns containing molten metals and molten salts. *Carbon* **2019**, *151*, 181–191.
- (262) Palmer, C.; Tarazkar, M.; Kristoffersen, H. H.; Gelinas, J.; Gordon, M. J.; McFarland, E. W.; Metiu, H. Methane pyrolysis with a molten Cu-Bi alloy catalyst. *ACS Catal.* **2019**, *9* (9), 8337–8345.
- (263) Leal Pérez, B. J.; Medrano Jiménez, J. A.; Bhardwaj, R.; Goetheer, E.; van Sint Annaland, M.; Gallucci, F. Methane pyrolysis in a molten gallium bubble column reactor for sustainable hydrogen production: Proof of concept & techno-economic assessment. *Int. J. Hydrogen Energy* **2021**, *46* (7), 4917–4935.
- (264) Yan, W.; Hoekman, S. K. Production of CO₂-free hydrogen from methane dissociation: A review. *Environ. Prog. Sustainable Energy* **2014**, *33* (1), 213–219.
- (265) Bode, A.; Anderlohr, C.; Bernnat, J.; Flick, D.; Glenk, F.; Klinger, D.; Kolios, G.; Scheiff, F.; Wechsung, A.; Hensmann, M.; Möhring, S.; Stubbe, G.; Lizandara, C.; Lange de Oliveira, A.; Schunk, S. A.; Göke, V.; Hunfeld, J.; Mihailowitsch, D.; Pleintinger, S.; Posselt, H.; Weikl, M. C.; Zander, H.-J.; Antweiler, N.; Büker, K.; Eckbauer, M.; Krüger, M.; Marek, P.; Rodermund, K.; Janhsen, U.; Mittelstädt, H.; Möllers, C.; Agar, D. W.; Munera-Parra, A. A. *Feste und fluide Produkte aus Gas – FfPaG*; Schlussbericht BMBF FKZ 033RC1301 A-G: März, 2018.
- (266) <https://www.basf.com/global/en/who-we-are/sustainability/we-produce-safely-and-efficiently/energy-and-climate-protection/carbon-management/innovations-for-a-climate-friendly-chemical-production.html> (accessed on 2021-03-18).
- (267) <https://www.basf.com/global/en/who-we-are/sustainability/we-produce-safely-and-efficiently/energy-and-climate-protection/carbon-management/interview-methane-pyrolysis.html> (accessed on 2021-03-18).
- (268) Palmer, C.; Bunyan, E.; Gelinas, J.; Gordon, M. J.; Metiu, H.; McFarland, E. W. CO₂-free hydrogen production by catalytic pyrolysis of hydrocarbon feedstocks in molten Ni–Bi. *Energy Fuels* **2020**, *34* (12), 16073–16080.
- (269) Postels, S.; Abánades, A.; von der Assen, N.; Rathnam, R. K.; Stückrad, S.; Bardow, A. Life cycle assessment of hydrogen production by thermal cracking of methane based on liquid-metal technology. *Int. J. Hydrogen Energy* **2016**, *41* (48), 23204–23212.
- (270) Dagle, R. A.; Dagle, V.; Bearden, M. D.; Holladay, J. D.; Krause, T. R.; Ahmed, S. *An overview of natural gas conversion technologies for co-production of hydrogen and value-added solid carbon products*; USDOE Office of Energy Efficiency and Renewable Energy (EERE), Transportation Office. Fuel Cell Technologies Office, 2017. DOI: 10.2172/1411934
- (271) Muradov, N. Low to near-zero CO₂ production of hydrogen from fossil fuels: Status and perspectives. *Int. J. Hydrogen Energy* **2017**, *42* (20), 14058–14088.

A Nonpremixed Annular Jet Vortex Chamber Reactor for Methane Pyrolysis under Oxygen-Enriched Conditions

Lei Chen,^{*,†} Santosh Shanbhogue,[†] Sreekanth Pannala, Vladimir Shtern, Ahmed Ghoniem, and David West

Cite This: *Ind. Eng. Chem. Res.* 2021, 60, 7443–7453

Read Online

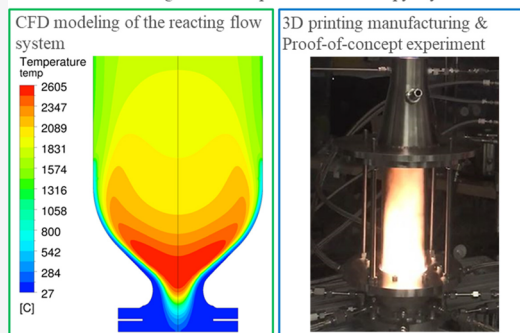
ACCESS |

Metrics & More

Article Recommendations

ABSTRACT: A novel high-swirl reactor ANJEVOC-CP (annular jet vortex chamber for combustion pyrolysis) was designed for producing high-value chemicals such as alkynes and olefins from natural gas. In such a single-stage nonpremixed combustion pyrolysis process, methane and oxygen streams are spirally conveyed into the ANJEVOC-CP burner creating high-swirl annular jets around an internal recirculation zone, leading to a compact nonpremixed fuel-rich flame for methane pyrolysis. Computational fluid dynamics (CFD) simulations of this reactor concept indicate the potential for high alkyne yield due to the rapid mixing of combustion products with CH₄ under a broad range of operating conditions; and this was experimentally verified in a lab-scale reactor under a subset of conditions (enriched oxygen concentration from 21% to 60% by volume and equivalence ratio from 1.28 to 2.4). The experimental studies showed 10.4 mol % carbon-based overall acetylene yield with up to 60% enriched oxygen molar concentration in the oxidizer stream in the lab-scale experiment. The CFD simulation predictions of the fluid flow and reactor performance are in reasonable agreement with the experimental observations and provided complementary insights into the respective roles of high swirl, species and thermal transport, and reaction kinetics that contribute to the high performance. Using a reduced GRI-Mech 3.0 and a modified GRI mechanism, the model predicted 20–25% overall acetylene yield at the same scale with higher enriched oxygen concentration. Considering the fact that excessive heat loss due to the high surface-area-to-volume ratio in the small lab-scale prototype with inert gas dilution could degrade performance, ANJEVOC-CP is a promising methane conversion technology for acetylene production and deserves further investigation at larger scales.

ANJEVOC-CP: A high swirl non-premixed methane pyrolysis reactor



1. INTRODUCTION

The growing abundance of natural gas resources from the shale gas revolution and their potential competitive cost advantage with respect to other light paraffinic hydrocarbons make the production of chemical intermediates and other high value chemicals from natural gas an attractive option. There are numerous methods for converting methane to higher molecular weight olefins and alkynes, and the most prevalent methods involve oxidative coupling, partial oxidation, or pyrolysis. Of all these approaches, high-temperature pyrolysis of methane for production of acetylene is promising for its high productivity, catalyst-free use, and high per-pass conversion.

Thermal pyrolysis of methane in inert environment yields high acetylene conversion at temperatures above 1600 °C.¹ Experimental studies have demonstrated 80% methane conversion and 80% acetylene selectivity through methane thermal pyrolysis on an electrical heated tungsten wire at coil temperatures of 1800–2000 °C.² In industrial scale reactors, the necessary endothermic heat of pyrolysis is usually supplied by combustion using enriched or pure oxygen that leads to

synthesis gas (carbon monoxide and hydrogen) production, limiting acetylene selectivity.

Depending on the mode of combustion and heat supply, methane pyrolysis technology pathways can be broadly classified into premixed and nonpremixed processes. The most representative single-stage premixed process has been commercialized by BASF³ producing 50 kTA acetylene since the 1950s. Preheated natural gas and pure oxygen are mixed in a diffuser, and partial oxidation reactions are carried out using a burner block. In the non-premixed two-stage acetylene production processes first developed by HOECHST,^{4,5} and later further developed by Synfuels⁶ and SABIC,⁷ near-stoichiometric oxy-fuel combustion produces high temperature gas in a first stage combustor, which supplies thermal energy

Received: January 11, 2021

Revised: April 26, 2021

Accepted: April 27, 2021

Published: May 3, 2021



for pyrolysis of raw natural gas in a second stage mixer and pyrolysis reactor. One advantage of the nonpremixed method is that it decouples combustion and pyrolysis reactions into two separate reactors with more degrees of freedom in operation, such as combustion in the first stage using fuel gas that is lower cost compared with purified natural gas or other cracking feedstock used as feed in the second stage.

Under an oxidizing environment in the combustion pyrolysis process, fast mixing of the hot combustion gases and the feedstock is critical in improving C2 (including C₂H₂, C₂H₄, and C₂H₆) selectivity as a high-value chemical product. Bartholomé⁸ reviewed previous nonpremixed single-stage combustion pyrolysis processes and suggested that since the mixing time scale of oxygen and hydrocarbons (usually in the order of millisecond) is higher than the lifetime of the acetylene formed in the reaction zone, acetylene undergoes subsequent cracking, reforming, and/or growth to soot precursors lowering its yield. Therefore, methods of enhancing mixing have been investigated in the nonpremixed combustion pyrolysis process. Zhang et al.⁹ investigated the impact of mixing ratio and reactor design parameters (nozzle number and reactor size) of a two-stage jet-in-cross-flow (JICF) reactor using computational fluid dynamics (CFD) simulations. Their study found that the C₂H₂ yield is greatly affected by mixing: C2 yield is negatively impacted when the reactor is scaled up at the same mixing ratio, because of the longer mixing time scale. Most recently, Chen et al.¹⁰ experimentally investigated natural gas conversion in a two-stage combustion pyrolysis reactor, with kinetics and CFD models developed for understanding the role of mixing. Their results showed that the overall carbon-based C2 yield decreases from ~36 mol % for an instantaneous mixing scenario to ~21 mol % for scenarios with realistic mixing time scales.

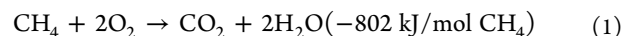
Swirling flow facilitates fast mixing and was utilized in industrial applications such as combustion, gasification, and reforming.¹¹ Shtern and Hussain¹² reviewed the characteristics of swirling flow and developed a mathematical model using full Navier–Stokes equations. Their theory predicts a thin annular high-speed jet near the wall with large recirculation region and intense mixing features beneficial for the current application. The theory also suggests an optimal design of a vortex burner with a converging-diverging nozzle which provides the stable and firmly anchored flame safely separated from the burner walls. These beneficial features were experimentally confirmed¹³ and served as the basis for the development of the reactor in this study.

The ANJEVOC-CP (annular jet vortex chamber for combustion pyrolysis) reactor is a novel device conceived with the goal of achieving fast mixing with high swirl. The “mixing while burning” concept is achieved by utilizing the annular high swirl jet and its unique fluid-dynamics characteristics.¹⁴ Its shorter mixing time scale and higher turbulent intensity compared with the cross-flow mixing methods improves acetylene selectivity by avoiding highly oxidizing environment while reducing CO formation. It differs from the BASF single-stage partial oxidation which uses a premixed flame, whereas the ANJEVOC-CP reactor features a compact and stable nonpremixed flame, which has improved the operational safety in contrast to the premixed partial oxidation concept. A lab-scale reactor was developed and optimized using CFD simulations for high performance and safe operation within the constraints of a laboratory setup. The modeling and simulations are used to derisk the experimenta-

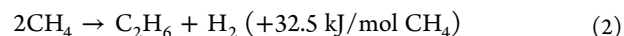
tion of this novel reactor concept and screen the operating condition design space for a reduced number of Design of Experiments (DOE) points. The optimized CAD model was 3D-printed and experiments were performed to obtain proof-of-concept results for a viability study of this high swirl nonpremixed reactor concept.

2. METHANE CONVERSION CHEMISTRY

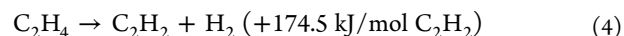
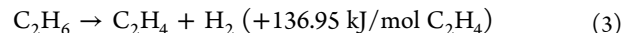
The complete combustion of methane in pure oxygen requires CH₄/O₂ molar ratio of 0.5 according to the following stoichiometric reaction:



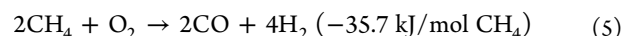
In the present single-stage combustion pyrolysis process, an extremely fuel-rich CH₄/O₂ molar ratio of 1.6–2 is used, with the excess methane serving as the “feed gas for cracking”. The feed gas is converted to C2 chemicals through a global endothermic coupling reaction as follows:



This is followed by rapid dehydrogenation reactions at high temperature to form C₂H₄ and C₂H₂.



Due to the highly endothermic nature of these coupling and dehydrogenation reactions, high initial temperatures (around 1600–1800 °C) are required to achieve significant C2 yield. The thermal energy at this high temperature is supplied by the nonpremixed flame located near the throat of the ANJEVOC-CP burner. On the other hand, the feed gas can also undergo parallel partial oxidation reactions to form synthesis gas primarily by reacting with oxidants present, such as O₂, OH, and O radicals. The following global reaction represents this alternative reaction pathway:



In order to improve the efficiency of conversion and economics of the process, the reactor should be designed and operated to preferentially promote the C–C coupling reaction in eq 2 rather than the competing partial oxidation reaction in eq 5 in order to maximize C2 selectivity. The partial oxidation pathway is dominant at high temperatures above 1900 °C and, thus, fast mixing of the excess methane into hot combustion product gases to achieve a mixing temperature below 1900 °C, preferably within 100 μs, could mitigate CO formation and improve C2 yield.¹⁰ Additionally, the effluent needs to be quenched within a few milliseconds (preferably below 10 ms) downstream of the pyrolysis reactor in order to freeze unsaturated alkene and alkyne products and minimize formation of heavy hydrocarbons and soot.

3. THE CONCEPT OF THE ANJEVOC-CP REACTOR

Figure 1 schematically depicts key elements of the ANJEVOC-CP reactor. The reactor consists of two circular disk distributors with tangential inlets for fuel/feed (methane) and oxidizer (oxygen with nitrogen dilution in the present study), fixed guide vanes to form a high-swirling flow, a converging-diverging nozzle, a tubular pyrolysis reactor, and a convergent section with secondary burner downstream. The converging-diverging nozzle geometry was designed based on

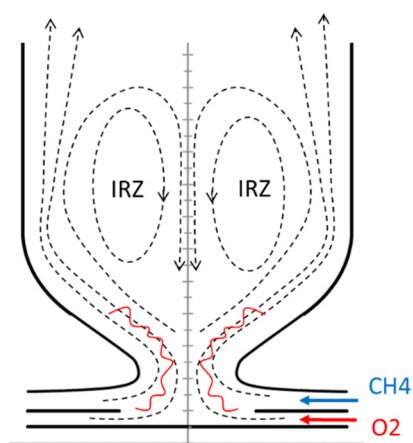


Figure 1. Schematic of ANJEVOC-CP burner section geometry and flow patterns within.

the analysis of swirling conical jets of a viscous incompressible fluid developed by Shtern and Hussain.¹²

Methane and oxidizer streams enter the circular disc distributors, and then flow across the tilted guide vanes with desired tangential to radial velocity ratio (preferably equal to or larger than 3). The difference in the inlet velocities of methane and oxygen creates a shear layer subject to the Kelvin–Helmholtz instability and thus enhances the mixing and combustion.

Due to vortex breakdown, the high swirl flow generates annular swirling jets at the converging-diverging nozzle, and an internal circulation zone (IRZ) centered around the nozzle axis and the outside flow. The large internal recirculation region aids in preheating the incoming oxygen and methane and anchoring a nonpremixed flame (shown as the red wrinkled curves) at the throat of the burner. Compared to other mixing strategies such as the cross-jet-flow or counter-jet-flow, the turbulence intensity in swirling flow is higher due to the Kelvin–Helmholtz instability in the counter current flow between recirculated hot combustion gas and “feed gas” that bypasses the combustion zone through the annular jet, which leads to shorter mixing time scales.

4. EXPERIMENTAL SETUP

A lab-scale ANJEVOC-CP reactor was designed and optimized based on the reacting flow CFD simulations of the process gas coupled with conjugate heat transfer of the cooling system. Figure 2 shows the section view of the ANJEVOC-CP reactor (to scale) consisting of four key components: (1) a gas feeding system with multiple volute inlets and tangential tilted guide vanes to generate high swirl flows; (2) a converging-diverging nozzle; (3) a tubular pyrolysis section; and (4) a convergent section as well as a secondary burner to completely oxidize all the effluent gases before discharging into a hood system located above the reactor. The hood flow rates are designed such that the temperature of the effluent gases diluted with entrained air is within the safety limits of the ducts and venting systems.

The inlet section consists of two vertically stacked sections, each containing gas entry fittings, a volute shape disk distributor, and guide vanes as shown in detail in Figure 3. There are four tangential 1/4 in. inlet ports in the bottom section and eight elbowed, 1/4 in. inlet ports on the top. They are optimized using CFD simulations to avoid any flow

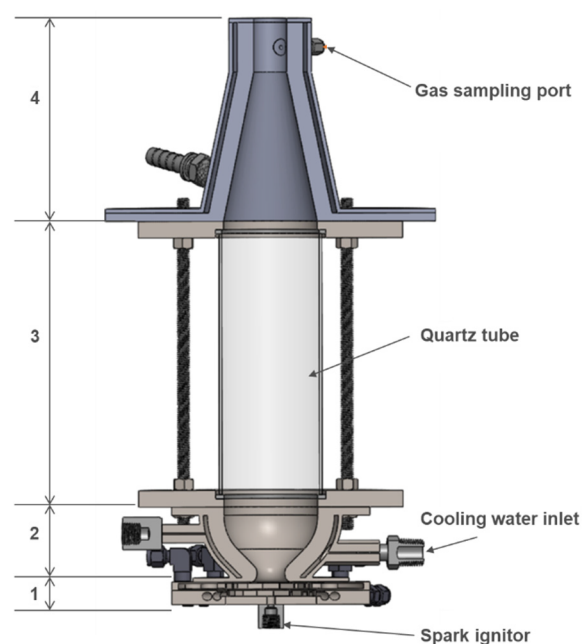


Figure 2. Schematic of the ANJEVOC-CP reactor with a quartz tube allowing for flow/flame visualization. Remarks for each section: (1) gas inlets and swirlers, (2) convergent–divergent nozzle, (3) pyrolysis section, (4) convergent section and secondary burner.

inhomogeneities around the circumference. Fourteen guide vanes that are 72° angles with regard to the radial direction were arranged in each section to ensure a high tangential to radial velocity ratio of approximately 3:1. The entire assembly including the gas feed system and convergent-divergent nozzle shape burner were 3D printed using SS316 powder. The burner section has a water-cooling jacket in order to protect the wall from high temperature. Downstream of the nozzle, a 3 in. i.d. transparent quartz tube was used in the tubular pyrolysis section for flow and flame visualization. Further downstream of the reactor has a convergent section to ensure a sufficiently high exit velocity to prevent any reverse flow. It also functions as a secondary flare burner for complete combustion of the gas products before safe discharge into the hood above the reactor. Gas samples were extracted from a wall-mounted sampling port at the end of the reactor and analyzed by a gas chromatograph (GC). Because the gas mixture comprises of flammable species (CO, H₂, C₂H₂, etc.) above the autoignition temperature, the effluent gases are immediately ignited at the outlet of the reactor with entrained air from ambient. This complete combustion of the process gas eliminates the flow of combustible and toxic gases into the exhaust ducts for a safe operation.

During the experiments, gases were sampled from the reactor using a custom-built sampling system consisting of 1 mm i.d. quartz tube, a 1000 cc/min sampling pump (Cole-Parmer), and a Valco 6-port, two-position switching valve. The sampling pump continuously draws a sample from a reactor and stores it in a 10 mL loop. When the recording is initiated, the stored sample is pushed into the GC using a separate helium tank connected to the switching valve. The whole process is controlled electronically and was calibrated to ensure that no leftover gases were collected in the system or contaminated the measurements. The sample gas temperature is estimated to be cooled below 500 °C within 0.1 ms due to

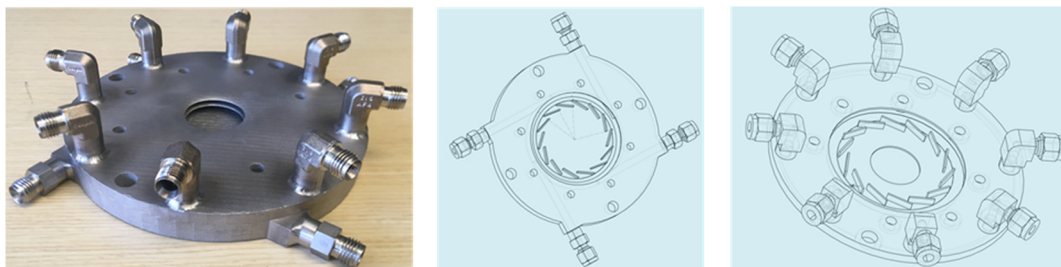


Figure 3. Three-dimensional metal printed gas feed system with volute inlets and guide vanes in order to generate high swirl flow. The two figures on the right show the CAD model of the oxidizer and methane feed layers, respectively.

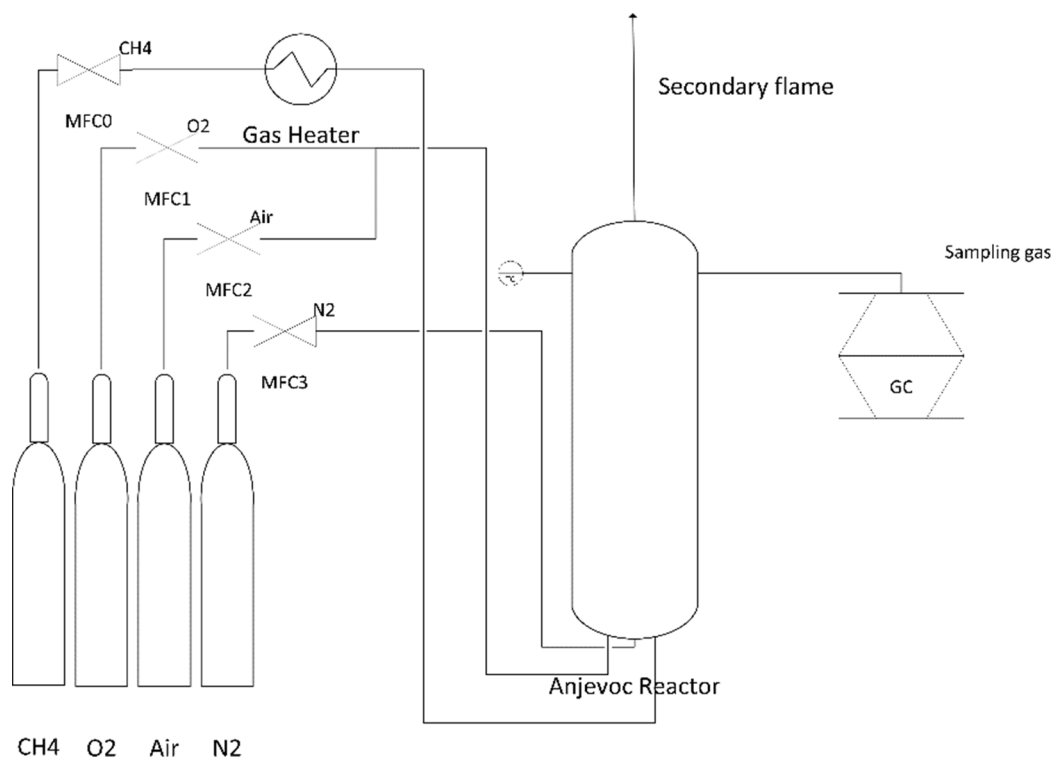


Figure 4. Schematic of the experimental system.

Table 1. Operating Conditions and Product Gas Compositions of the Pyrolysis Experiments

test no.	feeding flow rates (slm ^a), oxygen concentration, and overall ϕ					product gas dry mole fraction (%), balanced by N ₂					
	air	O ₂	CH ₄	O ₂ %	ϕ	CH ₄	H ₂	CO	CO ₂	C ₂ H ₂	C ₂ H ₄
1	150	0	20	21	1.28	0.29	5.3	5.74	7.68	0.12	0.064
2	150	7.86	30	25	1.52	1.26	12.16	10	6.55	0.41	0.099
3	150	19	43.5	30	1.73	2.23	13.82	13.4	6.51	0.577	0.108
4	75	23.39	40.27	40	2.07	4.675	23.52	18.69	6.589	1.14	0.262
5	42.2	41.16	60	60	2.4	6.257	28.26	21.25	5.81	1.64	0.3025

^aFlow rate unit is standard liters per minute (slm).

the small tubing diameter and large specific area/volume ratio, minimizing any secondary reactions before the GC analysis. When the sample was ready for analysis, helium gas was used to push the stored sample into the GC. The GC used for analysis was an Agilent 5890B, with six columns (HayeSep, MolSieve, and Innowax) fitted with two TCD detectors. Helium and nitrogen were used as carrier gases. The analysis time was 15 min. With these columns and detectors, the GC was calibrated daily using multiple cylinders of calibration gases to detect H₂, CH₄, C₂H₂, C₂H₄, C₂H₆, CO, and CO₂, from ppm to percent levels.

Figure 4 shows the experimental system setup with gas feeding and flow control, ANJEVOC-CP reactor, gas temperature measurement, gas sampling and GC system, etc.

The material property of quartz tube and the vertical clearance for the exit flame sets up certain constraints for reactor operation. Since quartz glows at around 500 °C, with a safe operating temperature up to 900 °C, pyrolysis tests were conducted with nitrogen as the dilution gas to reduce the maximum gas temperature within the reactor and the experiments were performed for short duration (around 1–2 min) to avoid heating the walls to unsafe temperatures and

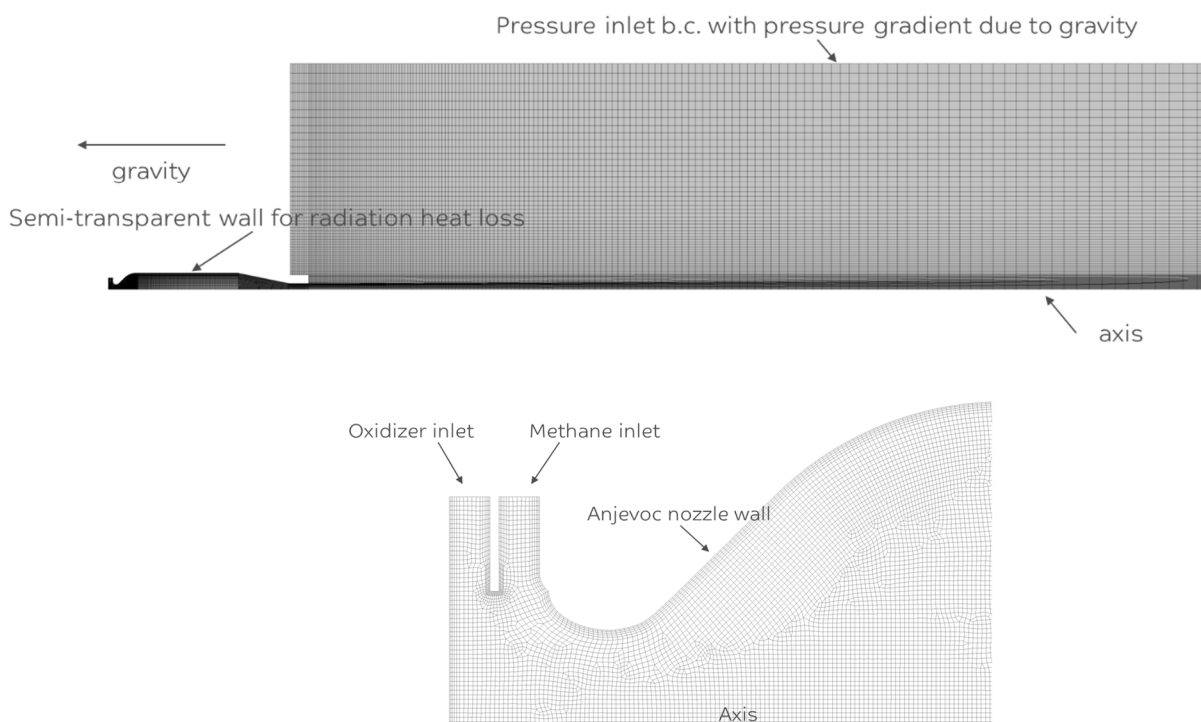


Figure 5. Two-dimensional axisymmetric CFD computational grid for the ANJEVOC-CP reactor and downstream secondary flame, with the lower figure showing mesh details of the reactor nozzle area.

ensure reactor integrity. A set of experiments were conducted by varying the enriched oxygen concentration (from 21 to 60 vol % by mixing pure oxygen and air) and fuel/oxygen equivalence ratios, maintaining adiabatic flame temperature of around 1700–1800 °C at which acetylene is the favorable product.¹⁰ The fuel/oxygen equivalence ratio (ϕ , or phi) is defined as

$$\phi = \frac{x_{\text{fuel}}/x_{\text{oxygen}}}{(x_{\text{fuel}}/x_{\text{oxygen}})_{st}} \quad (6)$$

where x_{fuel} is the fuel mole fraction, x_{oxygen} is the oxygen mole fraction, and suffix *st* stands for stoichiometric condition.

Higher enriched oxygen concentration allows for higher equivalence ratio operations (fuel rich conditions) while remaining in stable combustion regime. Gradually increasing oxygen concentration also shows the effect of inert gas dilution on pyrolysis performance. The operating conditions for the pyrolysis tests are summarized in Table 1 along with the product gas composition as measured by GC.

5. CFD MODELING APPROACHES

In order to model the complex interactions between the fluid dynamics, heat and mass transfer, mixing, and reactions in this novel reactor, CFD simulations were performed for the fully integrated domain including the ANJEVOC burner, the pyrolysis reactor, as well as the downstream open flame using ANSYS FLUENT 19.1. Figure 5 shows the two-dimensional axisymmetric computational grid used in this study, it consists of 29600 cells with near wall refinements to capture the boundary layers. The computational domain contains a 1 m diameter cylindrical open area following the end of the reactor, where the secondary diffusion flame is calculated to provide a natural boundary condition to the reactor outlet. The open boundaries are modeled taking into

account the buoyancy force and air entrainment from the surrounding space with appropriate pressure boundary conditions. The reason for modeling the downstream flame and open domain is 2-fold: (a) to capture the effect of the reactor outlet boundary conditions as high swirl flows could have toroidal inversion and the solutions in the reactor could be sensitive to the boundary conditions and (b) to derisk the experimental setup as there was limited clearance in the laboratory between the reactor and the hood. For this particular setup, the influence from the boundary is found to be minimal, and the simulations of the reactor alone with pressure boundary conditions were almost identical to the full simulations with downstream included.

Table 2 lists all the modeling options exercised. The simulation challenges are partially due to the highly turbulent and swirling nature of the flow with large gradients near the wall due to the annular jets and the complex interaction between fluid dynamics and chemistry occurring over a wide range of spatiotemporal scales. The accurate prediction of the

Table 2. Submodels Used in the CFD Simulations

physics	modeling approaches or submodels
turbulence	steady-state RANS (Reynolds stress model)
turbulence–chemistry interaction	Eddy dissipation concept with ISAT algorithm ²⁵
reaction mechanism	reduced GRI-Mech 3.0 (w/o N-species and reactions) ^{22,10} and reduced and modified GRI-Mech (w/reaction constant proposed by Liu et al. ²⁴)
gas thermodynamics properties	compressible ideal gas model with NACA thermodynamic database
radiation	discrete ordinate model with weighted-sum-of-gray-gas model for radiative properties
geometry discretization	two-dimensional axisymmetric grid containing 29579 cells

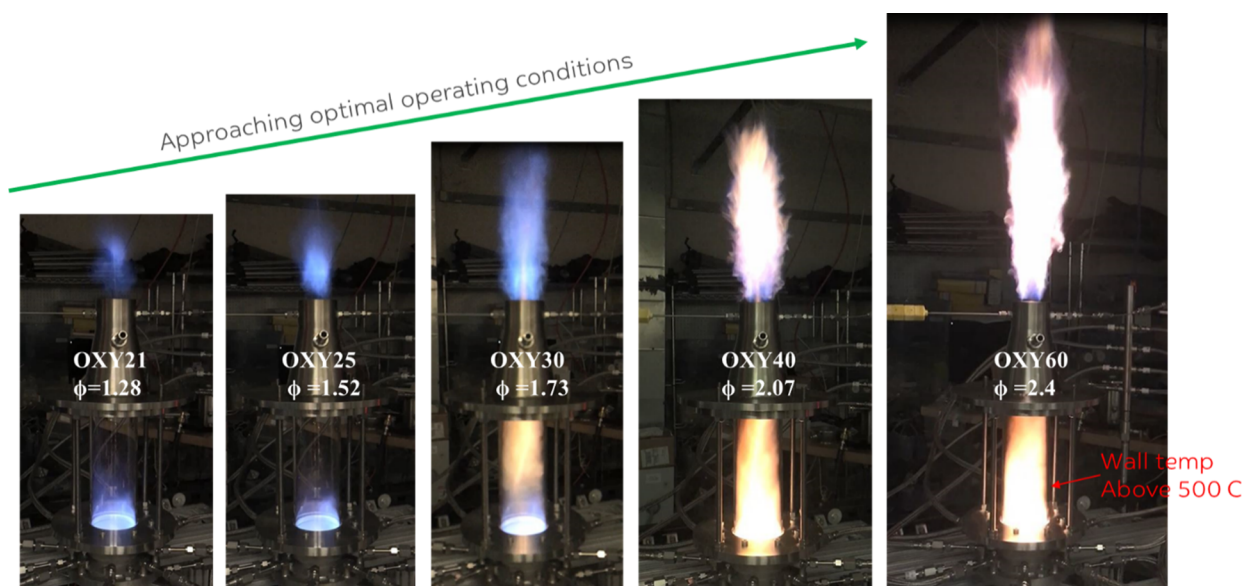


Figure 6. Snapshots of the ANJEVOC-CP reactor combustion pyrolysis test under varying enriched oxygen concentration (21%, 25%, 30%, 40%, and 60%) and equivalence ratio (1.28–2.4) conditions.

swirling flow and the corresponding internal recirculation zones in the burner throat region is critical to the mixing, heat and mass transfer, and reaction process.¹⁵ Previous studies demonstrated that the Reynolds stress model (RSM) performs better than the two-equation $k-\epsilon$ models in predicting the flow patterns¹⁶ for confined swirling flows in gas turbine combustor,¹⁷ industrial burner,¹⁸ and a vortex chamber.¹⁹ Therefore, in the current study, RSM with a linear pressure-strain model for the pressure-strain term was chosen to be the turbulence model to resolve the anisotropic turbulence properties in order to better predict the recirculation zones in high swirl flows.

Another challenge for the computation stems from the fact that the flow and chemical reactions cover a wide range of length and time scales. Specifically, the interactions between turbulence and chemistry are very different in the combustion and pyrolysis reactions as the temperature varies between 1200 to 2600 °C, and the reaction rates depend exponentially on the temperature. Combustion and oxidation at temperatures above 1800 °C takes less than 0.01 ms, and pyrolysis/reforming reaction is of the order of 2–4 ms,²⁰ while mixing can be in the order of 0.01–1 ms. This requires a turbulence-chemistry interaction model that takes into account the detailed reaction kinetics for important intermediate species and different reaction time scales for combustion and pyrolysis, while having high-resolution discretization of the space domain. The Eddy Dissipation Concept (EDC) model²¹ was used for turbulence–chemistry interactions with default model constants in FLUENT. The GRI-Mech 3.0 reaction mechanism²² was chosen in this study for an overall balance between accuracy and acceptable computational cost. In order to reduce the computational cost of the chemical kinetics calculation, all nitrogen species (except for N_2) and related reactions were removed from the original GRI-Mech, leading to a total of 36 species and 217 reactions (Reduced GRI-Mech 3.0) in the CFD simulations.¹⁰ It is noteworthy that the original GRI-Mech has been reported to overestimate the C_2H_2 selectivity in the postflame regions of one-dimensional premixed methane combustion.^{9,10,23,24} Therefore, we also used the modified

GRI-Mech (MGRI) with updated reaction constants proposed by Liu et al.²⁴ for the following elementary reaction:



Compared with the original GRI-Mech, this modified GRI-Mech is shown to improve predictions of C_2H_2 selectivity and yield under fuel-rich conditions, serving as a way to bound the uncertainty from simulations due to reaction kinetics.

Heat loss through the steel reactor and quartz tube walls was calculated using thin wall conduction model and convective cooling boundary conditions with an empirical convective heat transfer coefficient. A semitransparent wall boundary condition was used to model the radiation heat loss through the transparent quartz material.

Beyond all of the tested cases in the experimental studies, CFD simulations were performed with a wider range of equivalence ratios in order to investigate the sensitivity of reactor performance under tested enriched oxygen concentrations. The simulation results were analyzed and compared against the experimental data to gain insights into the thermochemical processes in the ANJEVOC-CP reactor.

6. RESULTS AND DISCUSSION

6.1. Flow and Flame Characteristics Observed in the ANJEVOC-CP Reactor. For swirling flows, the swirl number (S') is widely used to characterize the degree of swirl, with the definition of the angular momentum to axial momentum flux ratio as follows¹¹

$$S' \equiv \frac{G_\theta}{G_x} = \frac{\int_0^R (Wr)\rho U r \, dr}{R \int_0^R \rho U^2 r \, dr} \quad (8)$$

where G_θ is the axial flux of the tangential momentum, G_x is the axial flux of the axial momentum, R is the reactor inner diameter, ρ is the gas density, and W and U are the tangential and axial components of gas velocity, respectively. Based on the CFD simulation results of axial and tangential velocity distribution, the swirl number is about 0.61 at 2 diameter distance downstream the burner throat. A flow with this swirl

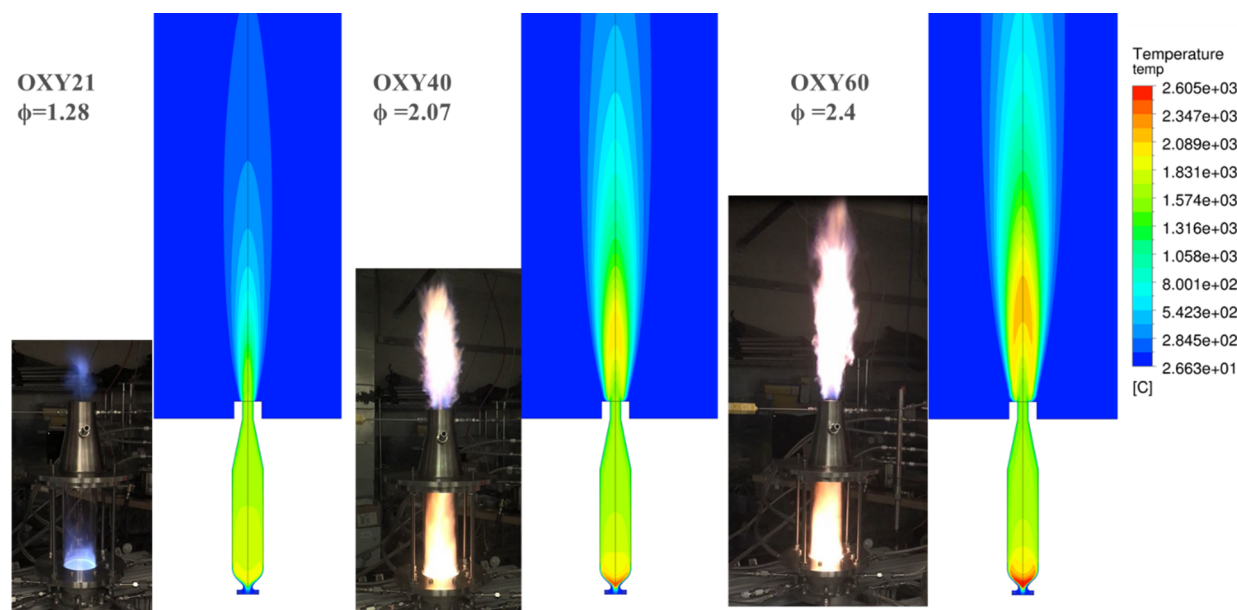


Figure 7. Comparison between the combustion pyrolysis test experimental images and CFD simulations results on temperature distribution, under 21%, 40%, and 60% enriched oxygen concentration. Results are predicted using reduced GRI-Mech 3.0.

number is characterized as a high swirl and is in agreement with the experimental study by Sheen et al.²⁶ using a radial-type swirl generator. The high swirl flow is essential for the formation of the annular jet flow pattern and intensive mixing desired in the ANJEVOC-CP reactor, leading to compact combustion and high C2 yield pyrolysis.

The combustion pyrolysis tests were conducted by progressively increasing the oxygen concentration and equivalence ratio toward what the simulations showed to be the optimal operating conditions. At higher oxygen concentration or less nitrogen dilution, the diffusion flame temperature increases, which enables higher equivalence ratios and accommodates the higher degree of endothermic reactions from pyrolysis. Under each enriched oxygen concentration condition, the equivalence ratio was chosen such that the overall equilibrium flame temperature were kept constant, similar to that of the fuel rich ($\phi = 1.28$) air combustion. This temperature is around 1700–1800 °C, at which acetylene is the more favored product as compared to carbon monoxide.¹⁰

Figure 6 shows snapshots of the ANJEVOC-CP reactor as a function of the increasing oxygen concentration levels and equivalence ratios. All cases are under fuel-rich conditions (equivalence ratio larger than unity); therefore, two flames were observed: a confined, nonpremixed flame anchored upstream at the swirl burner throat and a downstream secondary flame at the outlet of the reactor where the hot and combustible effluent gas instantly reacts with the entrained air upon mixing. The secondary flame was intentionally used as a safety measure to burn excess combustible gases before discharge. With the enriched oxygen concentration above 30% and equivalence ratio beyond 1.73, the burner flame color turned yellow and the length extended further downstream in the cylindrical section with intensive radiation through the quartz tube. The yellow flame was an indication of incomplete combustion with low flame temperature (around 1000 °C), usually accompanied with heavier hydrocarbon or soot formation/oxidation. Similarly, the secondary flame also turned from blue to yellow with extended length as enriched

oxygen concentration and equivalence ratio increased. As the enriched oxygen concentration reached 60% with equivalence ratio 2.4 (last image on Figure 6), the quartz tube wall started to glow at the stationary state, indicating the wall temperature crossed 500 °C.

It is noteworthy that the flame could become sooty with an even slightly higher equivalence ratio than the cases shown in Figure 6. A pyrolysis experiment with 40% oxygen concentration and equivalence ratio of 2.27 (not included in Table 1) showed significant soot formation as compared to the case with equivalence ratio of 2.07. In that case, even after a few minutes test, the sampling probe was clogged by the soot particles, and the inner wall of the quartz tube was coated by black soot. This observation indicated that there might be a limited operating window for high C2 yields due to soot formation, which needs to be further examined in future studies.

Although robust and anchored flames were observed under all tested conditions, some of the cases, especially at higher equivalence ratios, exhibited asymmetry with visual flow instabilities. The burner flame and downstream sooty cyclone behaved in helical or sloshing modes, with flame sheet bouncing across the shear layers leading to unstable operation. This flame instability can have a negative impact on the overall robustness and performance of the reactor. The details of this reacting flow dynamics can be quite interesting and could be a topic of later investigations.

Figure 7 compares the predicted temperature contours against the snapshots of pyrolysis experiments for selected operating conditions (enriched oxygen concentration of 21%, 40%, and 60%, with equivalence ratio of 1.28, 2.07, and 2.4, respectively). In order to compare the secondary diffusion flame length downstream the reactor outlet, all images are scaled to the same dimension. The CFD simulations can not only resolve the anchoring locations and shapes of the two separate flames that are observed in the experiments but also show a good qualitative match on the flame lengths characterized by the gas temperature. The current CFD model may overpredict the gas temperature as soot formation,

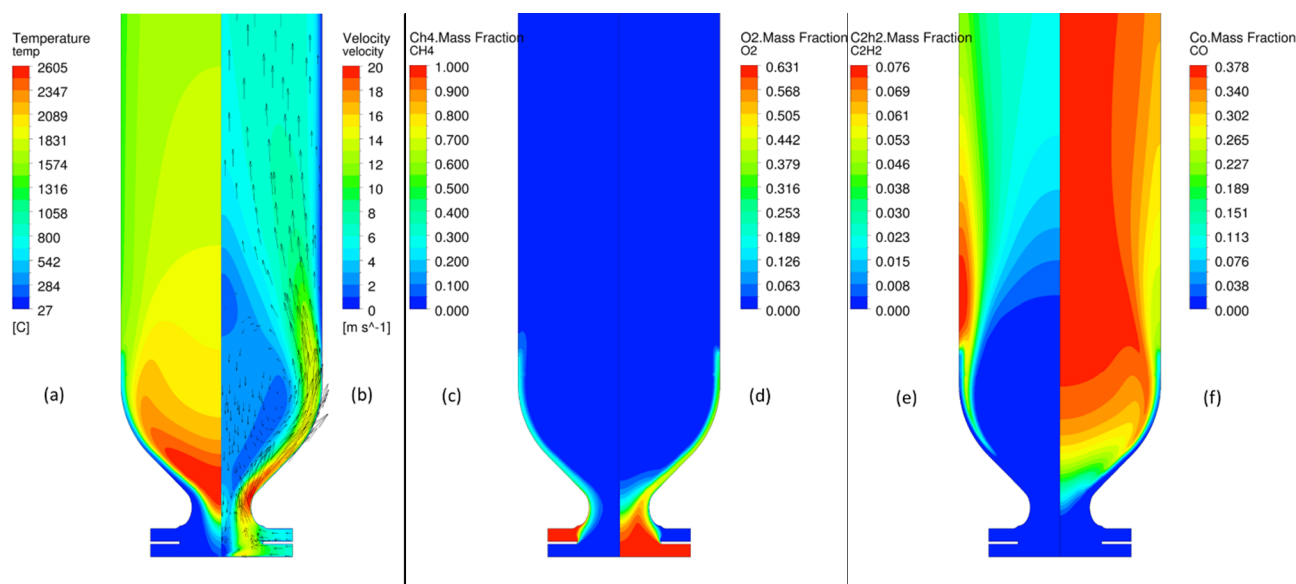


Figure 8. CFD predictions of (a) temperature, (b) velocity, (c) CH₄, (d) O₂, (e) C₂H₂, and (f) CO mass fraction, respectively, at 60% oxygen concentration and equivalence ratio of 2.4. Results are predicted using reduced GRI-Mech 3.0.

Table 3. Comparison of the Experimental and Simulation Results

test no.	exptl results (%)					CFD results ^b (%)				
	conversion	C2 yield	selectivity			conversion	C2 yield	selectivity		
			C2 ^a	CO	CO ₂			C2 ^a	CO	CO ₂
1	97.9	2.6	2.7	41.6	55.7	99.9	0.0	0.0	45.0	54.8
2	93.3	5.4	5.8	56.9	37.3	99.8	0.3	0.3	57.4	42.1
3	90.5	5.8	6.4	63.0	30.6	99.7	0.4	0.4	75.8	23.7
4	85.7	8.6	10.0	66.6	23.5	98.4	4.3	4.4	79.6	16.1
5	83.2	10.4	12.6	68.7	18.8	97.2	11.5	11.8	76.5	11.7

^aC2 includes C₂H₂ and C₂H₄ in the product gas compositions. ^bResults shown are CFD model predictions using reduced GRI-Mech 3.0.

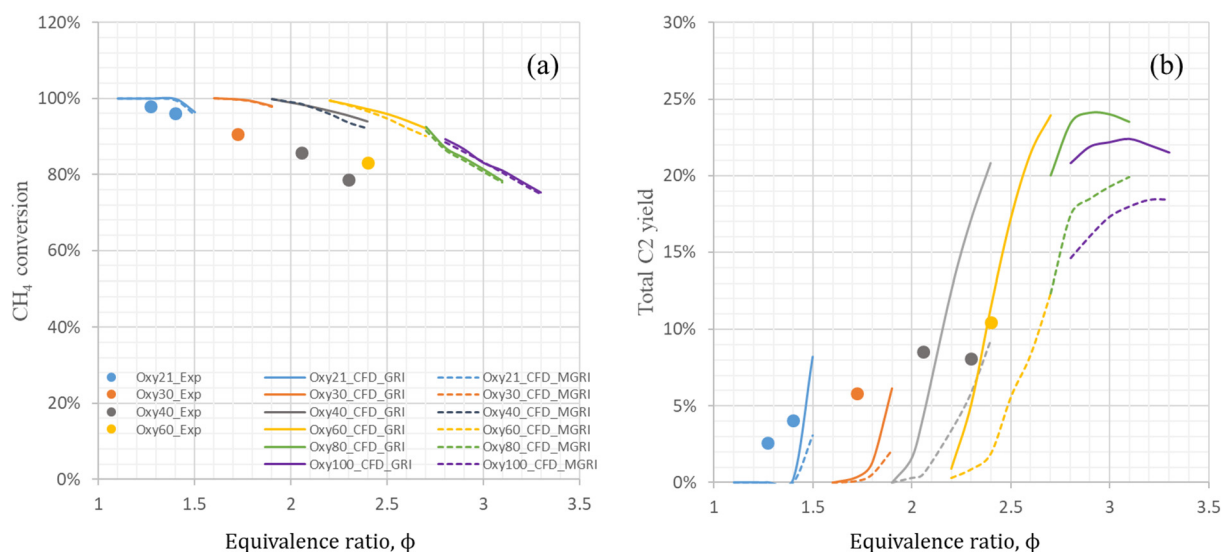


Figure 9. Comparison between experimental and CFD simulations on the (a) CH₄ conversion and (b) overall C₂ yield under varying operating conditions. Simulation results are predicted with both reduced GRI-Mech 3.0 (solid lines) and modified GRI (dash lines).

and its contribution to radiative heat transfer to the environment is not captured.

6.2. Conversion, Selectivity, and Yield of the Combustion Pyrolysis Tests. Figure 8 shows the CFD predicted temperature, velocity, and major gas species

distribution within the reactor at 60% oxygen concentration and an equivalence ratio of 2.4. The swirling flow forms an annular jet at the divergent burner wall with velocity magnitude up to 20 m/s, and an internal recirculation zone near the axis where hot combustion gas (up to 2600 °C) is

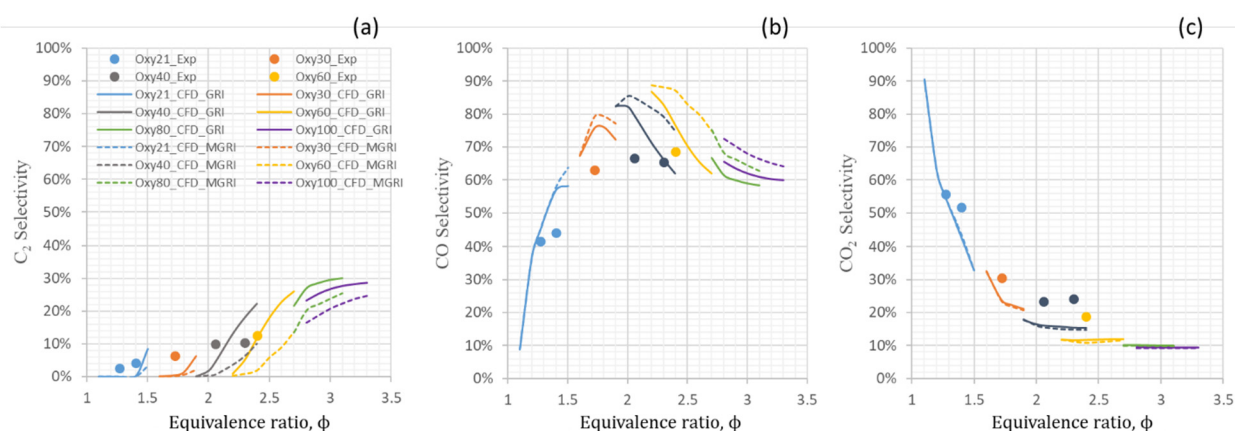


Figure 10. Comparison between experimental results and CFD simulations on the (a) C_2H_2 , (b) CO, and (c) CO_2 selectivity under varying operating conditions. Simulation results are predicted with both reduced GRI-Mech 3.0 (solid lines) and modified GRI (dash lines).

recirculated to stabilize the diffusion flame at the throat of the burner. The diffusion flame provides heat for endothermic pyrolysis reactions of the excess methane (above the equivalence ratio of unity) near the wall, which leads to high acetylene mass fraction at the end of the divergent burner section. On the other hand, CO is coproduced in the internal recirculation zone side of the flame sheet, as it is more favorable in an oxidizing environment.^{9,10} The intensive turbulent mixing of the combustion products and excess methane in the counter current flow due to the strong recirculation zone is critical in improving C_2 selectivity in this novel reactor design, as a shorter mixing time scale enhances C_2 production rather than CO.

Table 3 lists a comparison of the carbon molar based performance metrics (CH_4 conversion, C_2 yield, and selectivity) for experiments and CFD simulations. These metrics are defined as follows:

$$CH_4 \text{ conversion} = 1 - \frac{CH_4 \text{ molar flow rate in product gas}}{CH_4 \text{ molar flow rate in feed gas}} \quad (9)$$

$$C_2 \text{ yield} = \frac{\text{carbon molar flow rate in } C_2 \text{ product gases}}{\text{carbon molar flow rate in feed gas}} \quad (10)$$

$$\text{selectivity}_i = \frac{\text{carbon molar flow rate in species } i}{\text{carbon molar flow rate in converted } CH_4 \text{ gas}} \quad (11)$$

Figure 9 shows the experimental and CFD simulation results (using both GRI-Mech and MGRI) of CH_4 conversion and C_2 yield under all tested conditions, with data summarized in Table 3. These results are mainly affected by two variables: the enriched oxygen concentration and the equivalence ratio. In order to obtain the qualitative trends of the performance metrics, several CFD simulations were performed by varying the equivalence ratio under each oxygen concentration condition. Additionally, since the quartz tube reactor could not be operated with oxygen concentration above 60%, CFD simulations were also performed with water-jacket cooled steel reactor for 80% and 100% enriched oxygen concentration conditions, in order to ascertain potential performance this novel reactor could achieve. Note that the heat loss with water cooling jacket in the steel reactor is relatively higher than the

quartz tube reactor, and that was considered in the CFD simulations.

Both experimental results and CFD model showed high overall CH_4 conversion, above 80%, within the tested operating ranges, with conversion becoming lower at higher equivalence ratio due to the reducing environment. Although there is reasonable agreement against experimental data, the CFD simulation overpredicted CH_4 conversion beyond the equivalence ratio of 1.5, probably due to the fact that the steady-state CFD simulation could not resolve all the instabilities and dynamic features of the flame, which contributed to lower conversion. The other possibilities include the limited accuracy of the GRI mechanism for fuel rich conditions or the closures for turbulence-chemistry interactions. The CFD simulation results showed that the C_2 yield is quite sensitive to the equivalence ratio: the C_2 yield can change substantially as a function of the equivalence ratio. This indicates that experimental variations due to flow rate control accuracy may result in marginal C_2 yield result. Although the gas flow meters were calibrated, and the gas feed rate readings were stable with less than 1% change during all experiments, it is important to quantify drifting or other experimental errors. This also suggests that small modeling input deviations, either flow rate or chemistry compositions, can lead to significantly different predictions.

With acceptable agreement with the experimental results, CFD simulation with 80–100% enriched oxygen concentration and equivalence ratio around 3.0 predicted up to 20% (MGRI) and 25% (GRI) C_2 yield on a lab scale. Note that the both the original GRI-Mech and MGRI mechanisms showed a negligible difference in methane conversion prediction. However, the original GRI-Mech is shown to overpredict C_2 yield under fuel-rich conditions, as it only contains hydrocarbons up to C3 and could predict neither heavier hydrocarbon nor soot formation. The MGRI mechanism is expected to predict more accurate C_2 yield as it is fitted to fuel-rich experimental data that is representative of methane pyrolysis conditions. Soot formation might become a significant issue under high equivalence ratio conditions, and a short residence time (below 3–4 ms) should be used to mitigate the soot formation. By increasing the flow rates, one could achieve not only shorter residence times but also swirl flow with more intense recirculation region. This should improve overall robustness of the reactor operation along with improved pyrolysis performance.

Figure 10 shows a comparison between the experimental and CFD simulation results (using both GRI-Mech and MGRI) of product selectivity for major carbon species, such as acetylene + ethylene, carbon monoxide, and carbon dioxide. The CFD simulations are capable of predicting the CO and CO₂ selectivity as enriched oxygen concentration and equivalence ratio increases: the CO₂ selectivity keeps decreasing at higher enriched oxygen concentration and equivalence ratios, while experimental result CO selectivity showed a plateau at certain equivalence ratio around 2–2.5, followed by a decreasing trend at even higher equivalence ratios (as indicated by CFD simulations). In addition, the C₂H₂ selectivity keeps increasing and makes up that gap at higher equivalence ratios, indicating the higher enriched oxygen concentration and equivalence ratio is favorable for C₂ selectivity. The modified GRI mechanism showed relatively lower C₂ selectivity and higher CO selectivity than the original GRI-Mech, serving as a second model to bound the uncertainty from chemical kinetics and enable benchmarking against the experimental data.

7. FUTURE WORK

It is noteworthy that there are still gaps between the current and optimal operating conditions for high C₂ yield pyrolysis due to limitations of the test facility. Specifically, the thermal energy required for heating at least 40% inert N₂ in the oxidizer stream is significant; heat loss due to radiative heat transfer through the transparent quartz wall in the large surface-area-to-volume ratio lab-scale reactor is relatively higher than commercial scale reactors; and all inlet gases were not preheated (lack of heat recovery from the reactor). Nevertheless, these tests have provided invaluable information on flame stability and operating envelopes and showed promising methane conversion and C₂ yield under conditions of up to 60% enriched oxygen concentration and equivalence ratio of 2.4. A steel reactor with water cooling jacket has been designed and will be tested under pure oxyfuel combustion conditions and equivalence ratio up to 3.0–4.0 to verify the optimal conditions derived from CFD simulations. In addition, the CFD simulation approach was partially verified against the experimental results, however it needs further development to understand the flow instability, soot formation, residence time, and thermal integration and their impacts on the reactor performance.

8. CONCLUSIONS

A novel high-swirl flow reactor ANJEVOC-CP was developed for methane conversion and acetylene production using computational fluid dynamics simulations. This reactor features high-swirl annular jet flow patterns for fast and fine-scale mixing of combustion products and excess methane, leading to potentially higher C₂ olefin yields as compared to the conventional premixed and two-stage nonpremixed combustion pyrolysis technologies. The proof-of-concept experiments in a lab-scale 3D printed reactor demonstrated 10.4% C₂ yield with up to 60% enriched oxygen concentration and equivalence ratio of 2.4, which is promising considering the small scale of the reactor operating under limited oxygen enrichment without feed preheating. CFD simulations provided insights into the flow characteristics, mixing, heat mass transfer, and chemical reactions in the ANJEVOC reactor, and the results are in reasonable agreement with the

experimental data for methane conversion, C₂ yield, and CO/CO₂/C₂ selectivity over the tested operating conditions. CFD simulations further predicted up to 20–25% C₂ yield under the 80% and 100% oxygen concentration and equivalence ratios of 3.0–4.0 conditions at this laboratory scale. In the current study, the numerical simulations together with the experimental validation for a subset of conditions has indicated high performance for C₂ yields under optimal higher oxygen concentration and equivalence ratios. These conditions will be experimentally studied with either refractory-lined or water-cooled steel reactors and downstream processing of the product gases in the future.

AUTHOR INFORMATION

Corresponding Author

Lei Chen – SABIC Corporate Technology and Innovation, Houston, Texas 77042, United States; orcid.org/0000-0002-9521-4508; Email: lei.chen@sabic.com

Authors

Santosh Shanbhogue – Department of Mechanical Engineering, Massachusetts Institute of Technology, Cambridge, Massachusetts 02139, United States

Sreekanth Pannala – SABIC Corporate Technology and Innovation, Houston, Texas 77042, United States

Vladimir Shtern – SABIC Corporate Technology and Innovation, Houston, Texas 77042, United States

Ahmed Ghoniem – Department of Mechanical Engineering, Massachusetts Institute of Technology, Cambridge, Massachusetts 02139, United States

David West – SABIC Corporate Technology and Innovation, Houston, Texas 77042, United States

Complete contact information is available at: <https://pubs.acs.org/10.1021/acs.iecr.1c00131>

Author Contributions

[†]L.C. and S.S. contributed equally.

Notes

The authors declare no competing financial interest.

ACKNOWLEDGMENTS

The authors thank Dr. Balamurali Nair and Dr. Subramanian Sankaran for the discussions of experimental practices and heat transfer, Dr. Byeongjin Baek and Dr. Istvan Lengyel for the discussion on reaction mechanisms, and Dr. Mike Huckman, Dr. Pankaj Gautam, and Dr. Krishnan Sankaranarayanan for their constant support.

REFERENCES

- (1) Holmen, A.; Olsvik, O.; Rokstad, O. Pyrolysis of natural gas: chemistry and process concepts. *Fuel Process. Technol.* **1995**, *42*, 249–267.
- (2) Porsin, A. V.; Kulikov, A. V.; Amosov, Y. I.; Rogozhnikov, V. N.; Noskov, A. S. Acetylene synthesis by methane pyrolysis on a tungsten wire. *Theor. Found. Chem. Eng.* **2014**, *48* (4), 397–403.
- (3) Passler, P.; Feser, R.; Thelen, H. G. Preparation of acetylene and synthesis gas. US Patent US5789644A, 1998-08-04.
- (4) HOECHST. Process for the manufacture of unsaturated gaseous aliphatic hydrocarbons. Great Britain Patent GB921305A, 1963-03-20.
- (5) HOECHST. Process for cracking hydrocarbons. Great Britain Patent GB958046A, 1964-05-13.
- (6) Gattis, S.; Peterson, E. Process for the conversion of natural gas to hydrocarbon liquids. US Patent US20050065391A1, 2005-03-24.

- (7) Lin, Y.; Abdelghani, M. Process for the production of ethylene from natural gas with heat integration. US Patent US8080697B2, 2011-12-20.
- (8) Bartholomé, E. The BASF-process for production of acetylene by partial oxidation of gaseous hydrocarbons. *Chem. Eng. Sci.* **1954**, *3* (Suppl. 1), 94–104.
- (9) Zhang, Q.; Wang, J.; Wang, T. Enhancing the Acetylene Yield from Methane by Decoupling Oxidation and Pyrolysis Reactions: A Comparison with the Partial Oxidation Process. *Ind. Eng. Chem. Res.* **2016**, *55* (30), 8383–8394.
- (10) Chen, L.; Pannala, S.; Nair, B.; Lengyel, I.; Baek, B.; Wu, C.; VM, R.; West, D. Experimental and numerical study of a two-stage natural gas combustion pyrolysis reactor for acetylene production: The role of delayed mixing. *Proc. Combust. Inst.* **2019**, *37* (4), 5715–5722.
- (11) Beér, J. M.; Chigier, N. A. *Combustion aerodynamics*; Applied Science Publishers Ltd.: London, 1972.
- (12) Shtern, V.; Hussain, F. Hysteresis in a swirling jet as a model tornado. *Phys. Fluids A* **1993**, *5* (9), 2183–2195.
- (13) Shtern, V. *Cellular flows*; Cambridge University Press, 2018.
- (14) Pannala, S.; Shtern, V.; Chen, L.; West, D. Method and reactor for pyrolysis conversion of hydrocarbon gases. US Patent Application WO/2019/173570, 2018-03-07.
- (15) Chen, L.; Ghoniem, A. F. Simulation of Oxy-Coal Combustion in a 100 kWth Test Facility Using RANS and LES: A Validation Study. *Energy Fuels* **2012**, *26* (8), 4783–4798.
- (16) Escue, A.; Cui, J. Comparison of turbulence models in simulating swirling pipe flows. *Applied Mathematical Modelling* **2010**, *34*, 2840–2849.
- (17) Yang, S. L.; Siow, Y. K.; Peschke, B. D.; Tacina, R. R. Numerical study of nonreacting gas turbine combustor swirl flow using Reynolds stress model. *J. Eng. Gas Turbines Power* **2003**, *125* (July), 804–811.
- (18) German, A. E.; Mahmud, T. Modelling of non-premixed swirl burner flows using a Reynolds-stress turbulence closure. *Fuel* **2005**, *84*, 583–594.
- (19) Jawarneh, A. M.; Vatistas, G. H. Reynolds stress model in the prediction of confined turbulent swirling flows. *J. Fluids Eng.* **2006**, *128* (Nov), 1377–1382.
- (20) Li, X.; Dai, Z.; Wang, F. Characteristic Chemical Time Scale Analysis of a Partial Oxidation Flame in Hot Syngas Coflow. *Energy Fuels* **2017**, *31* (4), 4382–4390.
- (21) Magnussen, B. *On the structure of turbulence and a generalized eddy dissipation concept for chemical reaction in turbulent flow*; 19th Aerospace Sciences Meeting; American Institute of Aeronautics and Astronautics, 1981.
- (22) Smith, G. P.; Golden, D. M.; Frenklach, M.; Moriarty, N. W.; Eiteneer, B.; Goldenberg, M.; Bowman, C. T.; Hanson, R. K.; Song, S.; Gardiner, W. C. J.; Lissianski, V. V.; Qin, Z. *The GRI3.0 Mechanism*, UC Berkeley, [Online]. Available: <http://combustion.berkeley.edu/gri-mech/index.html>.
- (23) Gersen, S. Experimental study of the combustion properties of methane/hydrogen mixtures. Ph.D. Thesis, Groningen University, Netherlands, 2007.
- (24) Liu, Y.; Zhang, Q.; Wang, T. Detailed chemistry modeling of partial combustion of natural gas for coproducing acetylene and syngas. *Combust. Sci. Technol.* **2017**, *189* (5), 908–922.
- (25) Pope, S. Computationally efficient implementation of combustion chemistry using in situ adaptive tabulation. *Combust. Theory Modell.* **1997**, *1*, 41–63.
- (26) Sheen, H. J.; Chen, W. J.; Jeng, S. Y.; Huang, T. L. Correlation of swirl number for a radial-type swirl generator. *Exp. Therm. Fluid Sci.* **1996**, *12*, 444–451.

Comment on “Methane Pyrolysis for Zero-Emission Hydrogen Production: A Potential Bridge Technology from Fossil Fuels to a Renewable and Sustainable Hydrogen Economy”

Martin Keller*



Cite This: *Ind. Eng. Chem. Res.* 2021, 60, 17792–17794



Read Online

ACCESS |

Metrics & More

Article Recommendations

Sánchez-Bastardo et al. recently reviewed the pyrolysis of natural gas/methane for the production of hydrogen.¹ Their review provides an excellent overview of various mechanistic and process engineering aspects of methane pyrolysis; however, the description of methane pyrolysis as a “zero-emission” technology in the title as well as in the abstract should have been avoided. While it is true that, if carried out in an ideal manner, no direct CO₂ emissions evolve from methane pyrolysis, there are substantial greenhouse gas emissions associated with the use of natural gas. These are predominantly methane emissions. These emissions are important and would have warranted a more detailed discussion.

In methane pyrolysis, one mole of CH₄ with a higher heating value (HHV) of 891 kJ will yield, at best, 2 mol of H₂ with a total heating value of 572 kJ. The energy incorporated in the solid carbon of 394 kJ cannot be exploited if one wants to prevent the emission of CO₂ to the atmosphere. To provide the same amount of energy, natural gas production would thus have to be increased by at least a factor of 1.56. This will exacerbate the problem of upstream CH₄ emissions.

In their review, Sánchez-Bastardo et al. discuss greenhouse gas emissions from methane pyrolysis only based on results of Machhammer et al.² The authors assume upstream GHG emissions associated with natural gas production of 8.3 g CO₂ eq MJ⁻¹, which is a combined value of upstream CO₂ emissions and the CO₂-equivalent of the CH₄ emissions. Since CH₄ emissions vary widely by country and gas production method, and since there is large uncertainty in the reported data, it is useful to provide an analysis with variable CH₄ emissions. Because there is an ongoing debate whether the currently used 100-year global warming potential (GWP100 = 86) or the 20-year global warming potential (GWP20 = 34) should be used to assess the CO₂ equivalence of CH₄ emissions, I present results for both GWP100 and GWP20.³

Further, in Figure 1 of the review, the emissions from methane pyrolysis are compared to, among others, emissions from water electrolysis with grid electricity as well as H₂ produced through steam methane reforming. However, for H₂ to contribute substantially to the decarbonization of the global energy supply, its use needs to be expanded dramatically. According to the International Energy Agency (IEA), to date only about 6% of natural gas production is used for H₂ production for use in ammonia production and refining.⁴ Many potential applications of H₂ are thus those where H₂ is thought to substitute for natural

gas, such as space heating, power generation in gas turbines or solid oxide fuel cells, the provision of process heat in industry, or the direct reduction of iron ore for steel production. It is therefore useful to compare the GHG emissions of H₂ produced by CH₄ pyrolysis not just with other methods of H₂ production such as steam methane reforming and coal gasification but first and foremost with the direct use of CH₄ on an energy basis. Finally, I update some of assumptions used in the analysis by Machhammer et al. as summarized in Table 1.

In Figure 1, the GHG emissions of methane pyrolysis are shown as absolute values as well as the emission reductions compared to the direct use of CH₄. Total CH₄ emissions from the U.S. oil and gas supply chain have been estimated to be 2.3% of the total gas production by bottom-up modeling validated with top-down aerial measurements.⁷ With 2.3% CH₄ emissions, the achievable emission reduction when substituting natural gas with H₂ produced from methane pyrolysis is only 23% using GWP100 and less than 1% using GWP20. Specific emissions are 52 and 88 g CO₂ eq MJ⁻¹ with GWP100 and GWP20, respectively, significantly higher than the 31 g CO₂ eq MJ⁻¹ cited by Sanchez-Bastardo et al.¹

In the charts in Figure 2, I show whether CH₄ pyrolysis, direct CH₄ use, or electrolysis deliver energy with the lowest emissions, depending on the CO₂ intensity of the electricity used and the CH₄ emissions from the natural gas supply. State-specific, consumption-normalized, production-stage CH₄ emissions have been estimated by Burns and Grubert.⁸ Since, to the best of my knowledge, no state-specific, consumption-normalized, non-production CH₄ emissions estimates are available, I add another 0.8% of CH₄ emissions for all states based on gathering, processing, transmission, storage, and distribution estimates from Alvarez et al. (Note: The production emission estimate by Burns and Grubert is 1.6%, slightly higher than the 1.5% estimate by Alvarez et al. due to consideration of natural gas imported from Canada with 2.2% production emissions.⁷) For the estimation of the state-specific GHG intensity of electricity

Published: November 19, 2021



Table 1. Summary of Assumptions for GHG Emissions Calculations

	supply chain emissions	electricity consumption methane pyrolysis	electricity consumption electrolysis	electricity CO ₂ intensity
Machhammer et al. ² , Sánchez-Bastardo et al. ¹	8.3 g CO ₂ eq MJ ⁻¹ (CO ₂ and CH ₄ combined)	7.23 MWh _{el} t _{H₂} ⁻¹	48 MWh _{el} t _{H₂} ⁻¹	0.35 t _{CO₂} MWh _{el} ⁻¹
This analysis	3.7 g CO ₂ MJ ⁻¹ (ref 5) + variable CH ₄ emissions	7.23 MWh _{el} t _{H₂} ⁻¹	40.05 MWh _{el} t _{H₂} ⁻¹ (SOEC electrolyzer ⁶) + 2 MWh _{el} t _{H₂} ⁻¹ for H ₂ compression	0.42 t _{CO₂} MWh _{el} ⁻¹ (U.S. 2019) + natural gas supply chain emissions

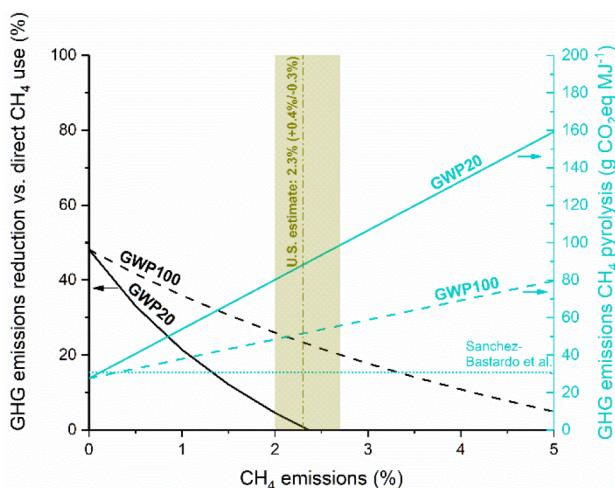


Figure 1. GHG emissions of CH₄ pyrolysis and relative emission reduction of CH₄ pyrolysis compared to direct CH₄ use, as a function of CH₄ emissions from natural gas production. Assumptions as listed in Table 1.

production, the natural gas supply chain emissions according to the state-specific natural gas consumption for power generation are added to the combustion emissions as reported by the U.S. Energy Information Administration.⁹ (Note: This simplified approach neglects supply chain emissions from coal-fired power generation, but these are comparatively small.) The resulting CH₄ emission estimates together with the GHG intensity of electricity production in the 11 states with the highest natural gas consumption are then superposed on Figure 2.

In states with comparatively high CH₄ emissions and high GHG intensity of electricity production, such as Indiana, Oklahoma, and Texas, with GWP20, a switch from direct natural gas use to H₂ produced through methane pyrolysis would increase GHG emissions. In California, electrolysis can produce H₂ with lower GHG emissions than CH₄ pyrolysis when GWP20 is considered. Only in states where CH₄ emissions are comparatively low, such as Pennsylvania, can CH₄ pyrolysis provide energy with the lowest emissions even on a 20-year horizon.

Whether CH₄ pyrolysis is a viable process to reduce GHG emissions will thus depend largely on current local conditions as well as future emission reduction trajectories for CH₄ emissions from natural gas production and emissions from electricity production. Only if CH₄ emission reductions proceed much faster than decarbonization of the electric power sector can methane pyrolysis be expected to contribute to GHG emission reduction as a bridging technology toward a carbon-neutral energy supply.

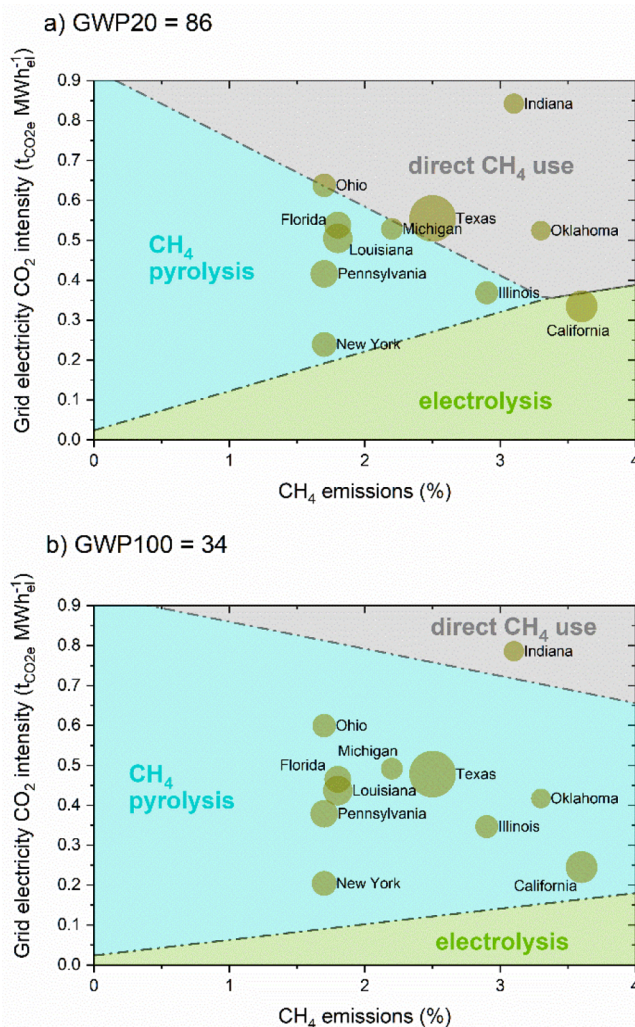


Figure 2. Charts indicating the lowest-emitting technology as a function of electric power CO₂ eq intensity and natural gas supply chain CH₄ emissions with (a) GWP20 and (b) GWP 100. Superimposed are the state-specific CO₂ eq intensity and supply chain CH₄ emissions; the size of the bubble corresponds to the state-specific volume of natural gas consumption.

■ AUTHOR INFORMATION

Corresponding Author

Martin Keller – Global Zero Emission Research Center, Smart CO₂ Utilization Research Team, National Institute of Advanced Industrial Science and Technology, Tsukuba, Ibaraki 305-8560, Japan; orcid.org/0000-0003-4583-9654; Email: keller-m@aist.go.jp

Complete contact information is available at:
<https://pubs.acs.org/10.1021/acs.iecr.1c03926>

Notes

The author declares no competing financial interest.

REFERENCES

- (1) Sánchez-Bastardo, N.; Schlögl, R.; Ruland, H. Methane Pyrolysis for Zero-Emission Hydrogen Production: A Potential Bridge Technology from Fossil Fuels to a Renewable and Sustainable Hydrogen Economy. *Ind. Eng. Chem. Res.* **2021**, *60* (32), 11855–11881.
- (2) Machhammer, O.; Bode, A.; Hormuth, W. Financial and Ecological Evaluation of Hydrogen Production Processes on Large Scale. *Chem. Eng. Technol.* **2016**, *39* (6), 1185–1193.
- (3) Ocko, I. B.; Hamburg, S. P.; Jacob, D. J.; Keith, D. W.; Keohane, N. O.; Oppenheimer, M.; Roy-Mayhew, J. D.; Schrag, D. P.; Pacala, S. W. Unmask Temporal Trade-Offs in Climate Policy Debates. *Science (Washington, DC, U. S.)* **2017**, *356* (6337), 492–493.
- (4) International Energy Agency. *The Future of Hydrogen*; Report prepared by the IEA for the G20, Japan, 2019. <https://www.iea.org/reports/the-future-of-hydrogen> (accessed 2021-11-18).
- (5) Howarth, R. W.; Jacobson, M. Z. How Green Is Blue Hydrogen? *Energy Sci. Eng.* **2021**, *9* (10), No. 1676.
- (6) Posdziech, O.; Geißler, T.; Schwarze, K.; Blumentritt, R. System Development and Demonstration of Large-Scale High-Temperature Electrolysis. *ECS Trans.* **2019**, *91* (1), 2537–2546.
- (7) Alvarez, R. A.; Zavala-Araiza, D.; Lyon, D. R.; Allen, D. T.; Barkley, Z. R.; Brandt, A. R.; Davis, K. J.; Herndon, S. C.; Jacob, D. J.; Karion, A.; Kort, E. A.; Lamb, B. K.; Lauvaux, T.; Maasakkers, J. D.; Marchese, A. J.; Omara, M.; Pacala, S. W.; Peischl, J.; Robinson, A. L.; Shepson, P. B.; Sweeney, C.; Townsend-Small, A.; Wofsy, S. C.; Hamburg, S. P. Assessment of Methane Emissions from the U.S. Oil and Gas Supply Chain. *Science (Washington, DC, U. S.)* **2018**, *188* (July), No. eaar7204.
- (8) Burns, D.; Grubert, E. Attribution of Production-Stage Methane Emissions to Assess Spatial Variability in the Climate Intensity of US Natural Gas Consumption. *Environ. Res. Lett.* **2021**, *16* (4), 044059.
- (9) U.S. Energy Information Administration https://www.eia.gov/electricity/data/state/annual_consumption_state.xls (accessed 2021-11-18).



DOI: 10.16085/j.issn.1000-6613.2018-2436

开放科学(资源服务)标识码(OSID):



热等离子体裂解甲烷制乙炔过程的数值模拟

李天阳, 安航, 李岳, REHMET Christophe, 程炎, 程易

(清华大学化学工程系, 北京 100084)

摘要: 针对热等离子体甲烷裂解过程, 建立了直流电弧反应器的数值模型, 使用磁流体力学理论对反应器内的电弧和流场进行数值模拟, 考察了电弧运动变化的规律和射流场特点, 并分别耦合热力学平衡模型和宏观动力学模型探索了裂解反应的特点及其与电弧的相互影响关系。结果表明反应器内电弧做规律运动和形态变化, 惰性无反应气氛下电弧形态变化不显著, 运动平稳。放电区发生反应时, 一方面气体的组成及热力学性质发生迅速变化, 气体放电特性受到影响, 等离子体的稳定性下降, 化学反应是等离子体不稳定性的重要来源。另一方面, 反应和扩散的特征时间小于电弧运动变化的特征时间, 各物质在空间的分布较为均匀, 受温度场非均匀性的影响较小, 模拟的甲烷转化率和乙炔收率与实验结果相近。本工作尤其是等离子体物理模型与甲烷裂解化学反应模型的耦合, 为理解热等离子体裂解相关过程提供了直接的帮助和指导。

关键词: 甲烷; 乙炔; 热等离子体; 电弧稳定性; 磁流体力学

中图分类号: TQ 2

文献标志码: A

文章编号: 1000-6613 (2019) 08-3572-11

Numerical simulation of methane pyrolysis to acetylene via thermal plasma

LI Tianyang, AN Hang, LI Yue, REHMET Christophe, CHENG Yan, CHENG Yi

(Department of Chemical Engineering, Tsinghua University, Beijing 100084, China)

Abstract: A numerical model with respect to thermal plasma pyrolysis of methane was established and a numerical study of the plasma and the reaction *via* the theory of magnetohydrodynamics (MHD) was carried out. The arc motion pattern and the characteristics of the fluid field regarding to temperature and velocity distribution inside the reactor were concluded, and further reaction model respectively considering thermodynamic equilibrium and simplified macro-kinetics was individually coupled into the MHD model to show the influence of pyrolysis reaction on plasma arc and the interactions between them. Generally, with pure argon as discharge media, the arc moved in a smooth and steady pattern, whereas the addition of methane would prolong the arc and accelerate the switch of arc-anode-spot. When reaction kinetics was considered, the gradient of temperature was elevated, yet the distribution of species was much more homogeneous due to the rapid diffusion of gas. The instability of arc under pre-mixing strategy was attributed to the pyrolysis reaction and the differences of thermodynamic properties of individual component.

Keywords: methane; acetylene; thermal plasma; arc stability; magnetohydrodynamics

收稿日期: 2018-12-17; 修改稿日期: 2019-02-15。

基金项目: 中国石油天然气集团有限公司石油化工研究院项目(16-03-03-05)。

第一作者: 李天阳(1993—), 男, 硕士研究生, 研究方向为天然气的等离子体转化。E-mail: litianyang1993@yeah.net。

通信作者: 程易, 教授, 博士生导师, 研究方向为等离子体化工过程。E-mail: yicheng@tsinghua.edu.cn。

引用本文: 李天阳, 安航, 李岳, 等. 热等离子体裂解甲烷制乙炔过程的数值模拟[J]. 化工进展, 2019, 38(8): 3572-3582.

Citation: LI Tianyang, AN Hang, LI Yue, et al. Numerical simulation of methane pyrolysis to acetylene *via* thermal plasma[J]. Chemical Industry and Engineering Progress, 2019, 38(8): 3572-3582.

世界范围内天然气的主要产能集中地与主要消费地呈现一定程度的地域隔离。由于气体长距离运输较困难, 成本较高, 因此将天然气就地转化为更高价值的化学品是提高天然气经济价值、解决运输困难的有效途径之一^[1]。热等离子体裂解法是利用高温喷射气流与甲烷混合、使之裂解并制备以乙炔为主的混合烃的方法。该方法的工作气体选择多元, 可以避免使用氧气, 进而避免二氧化碳生成, 提高碳原子利用率, 并副产大量氢气, 理论上原料甲烷的利用率能够达到 100%^[2-4]。该过程工艺简单, 水耗少, 与天然气部分氧化法相比具有竞争潜力, 对于发展绿色可持续的天然气化工过程具有重要意义^[4-5]。

对于等离子体裂解过程而言, 电弧的工作状态是影响反应结果的重要因素, 了解其稳定性和调控规律对于理解甲烷裂解过程具有实际意义。然而受限于等离子体高温、组成复杂、瞬态变化等特点, 实验中往往很难直接对等离子体电弧或高温射流进行观测。因此有必要通过数值模拟的手段认识等离子体电弧的运动变化规律及其与反应的相互耦合情况, 从而理解反应器内的过程。

磁流体力学 (magnetohydrodynamics, MHD) 理论是研究等离子体的有效工具, 但相关研究工作通常更关注模型的有效性和完善性, 对结果的分析也侧重于等离子体电弧本身的物理性质, 极少关注化学反应与等离子体的相互作用与影响^[6-10]。一些工作在研究热等离子体裂解甲烷的过程中, 在反应器的不同位置使用不同的模型, 如在反应器上游应用 MHD 模型获得等离子体射流的温度、流速等流场性质, 然后将其作为入口条件, 在下游只考察化学反应和体系组成^[11], 这种处理方法不能全面体现反应与电弧的相互作用, 尤其是对于直流电弧等离子体而言, 电弧状态与气体组成有很强的相关性, 因此有必要将化学反应动力学耦合到 MHD 模型中进行考察。

本文建立了实验室等离子体甲烷裂解反应器的数值模型, 使用数值计算软件 Code Saturne 对直流电弧等离子体进行磁流体力学模拟, 在毫秒尺度上揭示等离子体反应器内部的电弧状态以及其运动变化规律, 同时获得反应器内的流场信息。通过添加热力学平衡反应模型以及甲烷裂解宏观动力学模型, 初步探索裂解反应和等离子体电弧之间的互相影响, 并分析总结等离子体电弧产生不稳定性的原因, 与实验结果对照, 为理解等离子体反应器内部

的过程及反应行为提供重要参考。

1 物理模型的数学描述

1.1 模型简化与假设

使用由法国电力公司 (Electricité de France, EDF) 开发的计算流体力学软件 Code Saturne (Edition 2.0) 进行数值模拟, 在模拟中作以下简化与假设^[12-13]。

(1) 热等离子体处于局部平衡状态 (local thermodynamic equilibrium, LTE), 电子温度与重粒子温度近似相等。

(2) 等离子体呈电中性状态, 为不可压缩流体, 作定常流动, 给定点的热力学性质和流体力学性质由温度和压力确定。

(3) 不考虑热等离子体中的辐射过程。

(4) 不考虑电极材料的相变过程以及气相中的金属对等离子体电弧的影响, 同时由于鞘层较薄, 对反应的影响有限, 故忽略电极鞘层的影响。

(5) 认定等离子体处于层流状态。

(6) 根据准静态假设、宏观电中性假设、欧姆定律、库仑规范等条件, 将麦克斯韦方程组 (Maxwell's equations) 简化、变形为下述形式。

电场 E 表示为某标量势场 P_R 的梯度场, 见式 (1)~式(3)。

$$E = -\nabla P_R \quad (1)$$

$$j = \sigma E \quad (2)$$

$$\text{div}(\sigma \nabla P_R) = 0 \quad (3)$$

给定电势 P_R 的边界条件, 即可根据式(3)求出电势场, 进而得到空间电场分布。磁感应强度 B 表示为某矢量势 A 的旋度场, 见式(4)、式(5)。

$$B = \text{rot}(A) \quad (4)$$

$$\text{div}(\text{grad}(A)) = -\mu_0 j \quad (5)$$

给定矢量势 A 的边界条件, 即可根据上式求出矢量势场, 进而得到空间磁感应强度。式中, j 为电流密度; σ 为电导率; μ_0 为真空磁导率。

1.2 磁流体力学理论与控制方程

等离子体可以视作连续介质并用流体力学方程进行描述, 在 MHD 理论下, 需要联立变形后的电磁学方程共同求解, 即需要求解电场、磁场、电流密度等, 同时热等离子体电流密度较大, 需要在动量方程中添加洛伦兹力项 (Lorentz's force), 并在能量方程中添加欧姆效应项。此外热等离子体中的温度压强变化范围较大, 各物性参数不能简单地表

示为温度和压强的函数, 计算时需要提供完善的气体物性数据。

根据 Code Saturne 软件的说明, 其所求解的控制方程组见式(6)~式(8)。

质量守恒方程

$$\operatorname{div}(\rho \mathbf{u}) = 0 \quad (6)$$

动量方程

$$\frac{\partial}{\partial t}(\rho \mathbf{u}) + \operatorname{div}(\rho \mathbf{u} \otimes \mathbf{u}) = \operatorname{div}(\boldsymbol{\sigma}) + \mathbf{j} \times \mathbf{B} \quad (7)$$

能量方程

$$\frac{\partial}{\partial t}(\rho h) + \operatorname{div}(\rho \mathbf{u} h) = \operatorname{div}\left(\frac{\lambda}{c_p} \nabla h\right) + \mathbf{j} \cdot \mathbf{E} \quad (8)$$

以上3式联立式(1)~式(5), 即可求得等离子体的速度场、温度场、电场、磁场、电流密度等。式中, ρ 为密度; \mathbf{u} 为速度矢量; $\boldsymbol{\sigma}$ 为应力张量; h 为焓; λ 为热导率; c_p 为比热容。

1.3 反应模型

为了考察甲烷裂解反应对于电弧的影响, 需要将甲烷裂解动力学模型添加到控制方程组中, 然而由于裂解反应物种数繁多、热力学性质数据量庞大, 并且方程组刚性较强, 求解较为困难, 本研究将反应对等离子体电弧的影响分为两步来考虑。第1步使用热力学平衡模型考察甲烷-氩气混合载气对等离子体电弧的影响, 第2步以简化的宏观动力学作为反应模型, 在控制方程组中添加质量分数方程, 考察甲烷的转化效果和等离子体电弧的性质。

1.3.1 热力学平衡模型

热力学平衡模型方法是指在计算时选用甲烷-氩气混合气体达到一定温度下的热力学平衡状态后所表现出来的宏观物理性质, 这里的热力学平衡主要指组分平衡, 包括裂解生成的各种自由基、离子、电子等, 宏观物理性质主要指焓值、热容、黏度、电导率等运输性质。在热力学计算过程中考虑所有组分, 但最终名义上只存在一种气体, 即混合气体。

这样的模型可以理解为甲烷在任意温度下的动力学裂解反应速率都极快, 可以在瞬间达到热力学平衡状态, 低温下即使反应很慢, 但裂解反应几乎不发生, 模型近似于简单的物理混合。由此, 在计算时只需要提供一种物质(即混合气体)的性质即可。本文所使用的热力学数据通过美国国家航空航天局(National Aeronautics and Space Administration, NASA)开发的热力学计算程序CEA(Chemical Equilibrium with Applications)获得^[14-15]。

1.3.2 宏观动力学模型

以构建耦合反应动力学的等离子体模型为主要目的, 只初步考虑如下的宏观动力学, 即忽略反应机理和产物的分解, 甲烷直接生成乙炔和氢气, 反应式见式(9)。



其中 k 为反应速率常数, 并认定反应为一级不可逆反应, 故速率常数的单位为 s^{-1} , 由阿伦尼乌斯公式计算得到, 见式(10)。

$$k = A \exp\left(-\frac{E_a}{RT}\right) = 4.5 \times 10^{13} (\text{s}^{-1}) \times \exp\left(-\frac{91 \times 10^3}{8.314 \times T}\right) \quad (10)$$

式(10)中的活化能与指前因子均参考自文献^[16-18]。上述反应涉及3种物质, 在计算时直接求解质量分数方程, 见式(11)~式(15)。

$$\frac{\partial(\rho w_i)}{\partial t} + \nabla \cdot (\rho \mathbf{u} w_i) - D_i \rho \nabla^2 w_i - r_i = 0 \quad (11)$$

$$D_i (\text{m}^2/\text{s}) = \frac{0.0101 \times T^{1.75} \sqrt{\frac{1}{M_i} + \frac{1}{M_{\text{Ar}}}}}{\rho (v_i^{1/3} + v_{\text{Ar}}^{1/3})^2} \quad (12)$$

$$r(\text{CH}_4) = -k\rho w(\text{CH}_4) \quad (13)$$

$$r(\text{C}_2\text{H}_2) = \frac{1}{2} \times \frac{[-r(\text{CH}_4)]}{16} \times 26 = \frac{13}{16} k\rho w(\text{CH}_4) \quad (14)$$

$$r(\text{H}_2) = \frac{3}{2} \times \frac{[-r(\text{CH}_4)]}{16} \times 2 = \frac{3}{16} k\rho w(\text{CH}_4) \quad (15)$$

其中式(11)为质量分数守恒方程, w_i 为物质 i 的质量分数; D_i 表示物质 i 在氩气中的扩散常数^[19], 由式(12)计算得到; v_i 为分子扩散体积, 甲烷、乙炔、氢气、氩气的分子扩散体积分别为 $25.1 \text{cm}^3/\text{mol}$ 、 $36.4 \text{cm}^3/\text{mol}$ 、 $6.12 \text{cm}^3/\text{mol}$ 、 $16.2 \text{cm}^3/\text{mol}$ 。式(13)~式(15)分别为甲烷、乙炔、氢气的反应速率, 单位为 $\text{kg}/(\text{m}^3 \cdot \text{s})$ 。将上述反应模型引入磁流体学模型中共同求解, 则可以得到各物质的质量分数, 混合气体的物理性质由软件内置的混合规则确定, 需要提供不同物质的热力学性质数据, 同时暂不考虑反应热对于温度的影响。

1.4 计算域和边界条件

针对实验中使用的裂解反应装置^[20], 在计算时选取从等离子体载气入口上方到淬冷气入口下方的一段作为计算域, 图1为示意图及详细尺寸。阴极即为上端的棒状电极, 其尖端为一圆台, 阳极为整个壁面。上方进气口的直径为 6mm , 左右对称分布有2个; 下方淬冷气进气口有6个, 直径为 1mm , 位于第2层台阶的垂直壁面上。整体模型与

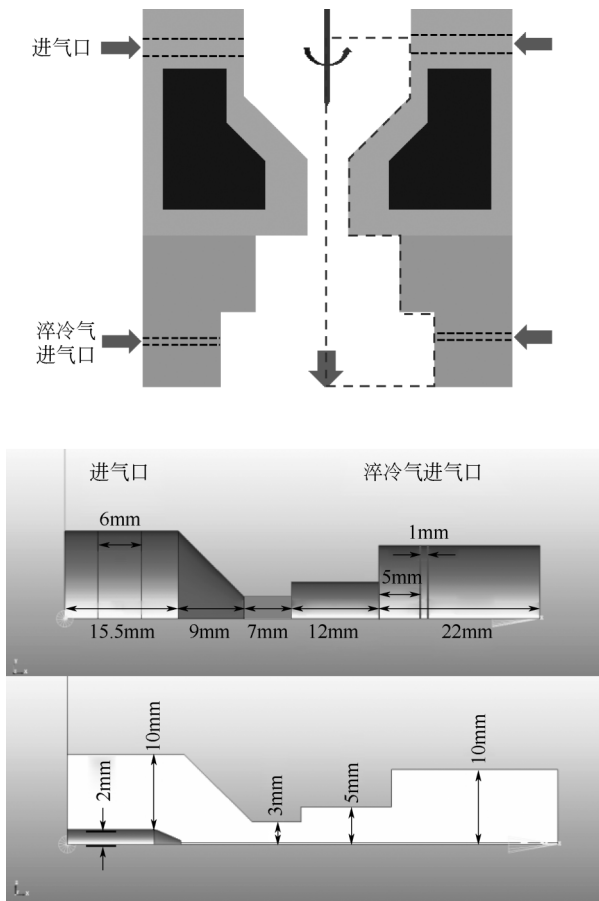


图 1 计算域示意图及详细尺寸

实际装置基本相符。使用开源软件 Salome (由 Atomic Energy Commission、EDF、Open Cascade 共同开发) 构建三维网格, 综合计算效率和准确度, 最终确定网格数量为 2×10^5 左右, 同时加密了中心轴区域附近的网格, 以使电弧的计算更为稳定、可靠。

计算时使用的边界条件和体相初始化条件见表 1。注意由于本研究工作采用的物理模型并不包含气体击穿的起弧过程, 故在初始化体相温度场(焓值)时, 直接给出一个人为设定的高温通道, 使气体电导率足够产生电流, 之后再随着计算进行任电弧自由发展。又由于忽略了鞘层影响, 故电势边界条件在电极处也是均一的, 由每步的总功率和电流计算得到。矢量势边界条件在出口和壁面处设定其梯度为 0。

2 模拟结果与讨论

2.1 模型验证

如图 2(a)所示为氩气气氛下电弧电压随时间变化的模拟结果 (15ms 之前尚处于非稳状态), 图 2

表 1 反应器不同位置的边界条件及体相初始化条件

位置	入口	出口	壁面	阴极	体相初始化
温度	300K	—	$\frac{\partial T}{\partial n} = 0$ (中间段) 300 K (其他)	$\frac{\partial T}{\partial n} = 0$	10 ⁴ K (电弧) 300K (其他)
电势	0	0	0	-10 (初始化)	0
矢量势	0	$\frac{\partial A}{\partial n} = 0$	$\frac{\partial A}{\partial n} = 0$	0	0

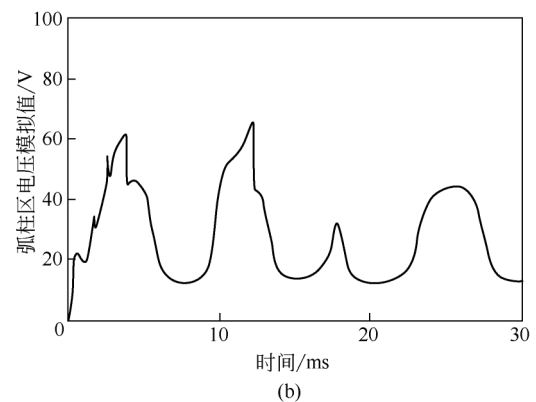
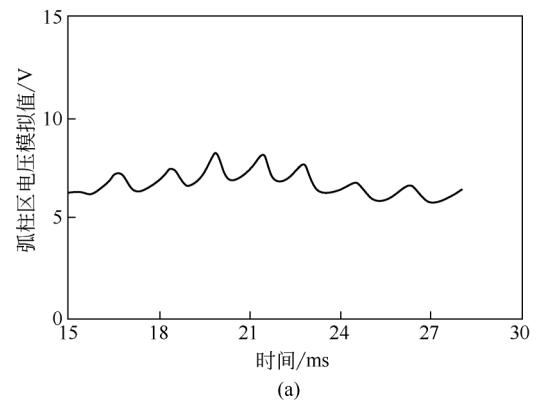


图 2 弧柱区电压模拟值随时间变化关系

(b)为含甲烷混合气作为载气时 (甲烷体积分数为 10%) 电弧电压随时间变化的模拟结果, 模拟中载气流量均设定为 10L/min, 电流值均设定为 40A。模拟结果可以在一定程度上反映出电压的波动, 这里以模拟电压的平均值与实验中观测的电压平均值进行对比, 同时需要指出的是, 由于鞘层中电势降较大, 忽略鞘层的影响会导致模拟的电压结果偏小, 故在比较时根据文献中类似条件下对鞘层电压的估计值加上弧柱区电压的模拟值作为实际电压的估算值。

在氩气气氛下, 实验中的电压平均值约为 17.5V, 阴极鞘层电势降取 12V^[19-20], 阳极鞘层电势降约为 2V^[21-22], 模拟给出的弧柱电势降约为 6.7V, 故电弧电压估计值约为 20.7V, 与实验中测得的电压的差距在合理范围内。类似地, 在预混有 10%

甲烷（体积分数）的载气气氛下，实验中的电压平均值约为 45V，模拟电压的平均值约为 27V，鞘层电势降仍取为 14V，则电弧电压估计值为 41V，与实验中的结果基本接近。

经过对模拟电压和实验观测电压的比较，可知模拟结果与实验结果基本相符，模型适用于该体系。

2.2 热力学平衡模型下的等离子体裂解过程

在模拟中选用甲烷体积分数为 10% 的混合气作为等离子体炬的载气，与实验中典型条件下的混合气甲烷分数基本对应（1L/min 的甲烷进流量、10L/min 的载气流量）。首先考察甲烷混合气放电的特性，对含甲烷载气和惰性载气的热力学性质差异进行分析，之后考察载气流量和电流设定值对等离子体的影响，并对实验中的现象进行解释。

2.2.1 含甲烷载气与惰性载气放电特性的不同

设定载气流量为 10L/min，电流为 40A，首先

考察纯氩载气和含甲烷载气情况下电弧的形态、运动规律以及温度场的分布，图 3 为等离子体电弧随时间的变化情况。由图可知载气中含有甲烷时，电弧在 2ms 内延伸至进料混合段，在实验中也确实发现此处有不锈钢熔化的迹象。之后约每 2ms 发生一次弧根转移，同时电弧作伸缩变化，弧根位置不断在锥形结构顶部和炬出口之间移动。温度场的变化滞后于电弧的运动。与纯氩气氛下的电弧相比，混有甲烷的载气会使电弧的变化幅度更大、变化周期更短，并且当弧根的位置靠近上游时，射流温度分布的不对称性较严重，更多的载气会从弧根的对侧流出，在实际过程中意味着甲烷尚未转化就离开高温区。同时，在载气中混有甲烷时，电弧核心高温区的半径相比氩气作载气时更小，进料混合段的径向温度梯度更大，中心温度接近 10⁴K，靠近壁面位置的温度大约为 5000K，射流高温更迅速地延

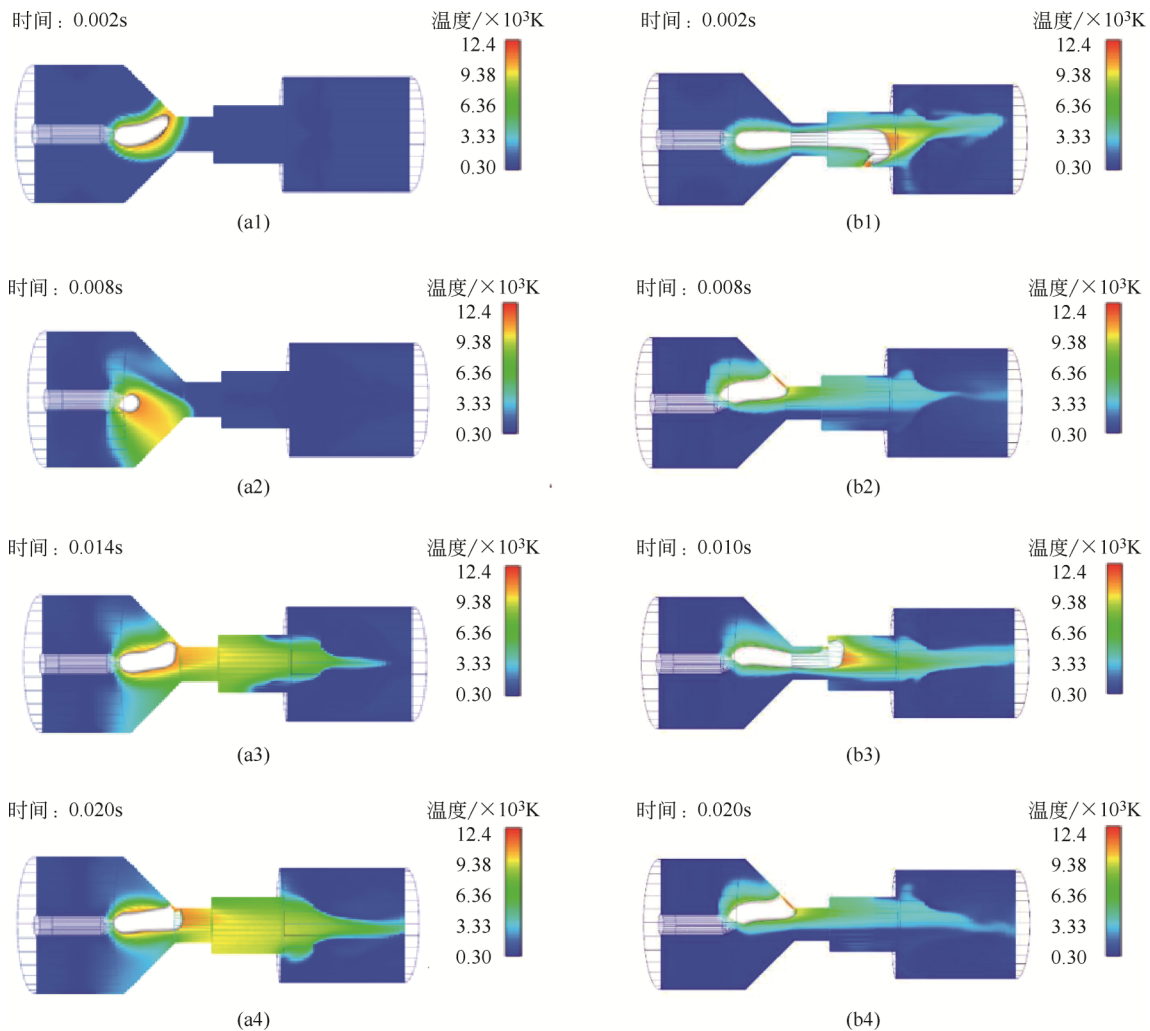


图 3 电流密度等值面及温度场随时间变化情况

(a1) ~ (a4) 纯氩载气; (b1) ~ (b4) 含甲烷载气

伸至下游反应段（2ms 内即延伸至第二级变径处）。

图 4 为不同载气氛围下反应器中心轴线温度分布的对比图，在混有甲烷时第一级台阶（40mm 之前）的温度显著高于纯氩气的温度，而该区域正是等离子体发生装置内甲烷发生裂解反应的主要位置，因此在载气中混入甲烷获得的裂解效果要优于在等离子体炬下游给入甲烷的裂解效果。

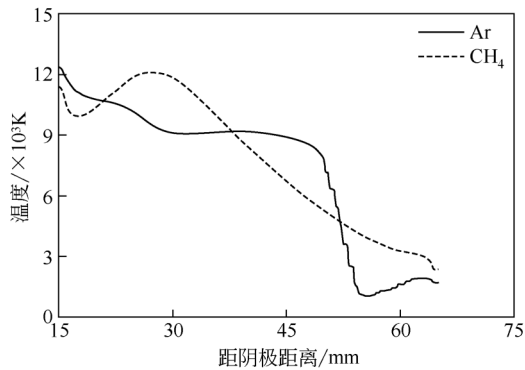


图 4 两种气氛下反应器轴线温度分布对比

图 5 分别为不同载气氛围下反应器内的速度场示意图。首先可见纯氩气氛围下，反应器内的最大气速接近 70m/s，而混入甲烷后，最高气速显著提升至 110m/s。其次，当电弧弧根位置靠近下游、射流被充分加热时，射流的速度分布较为对称，而当弧根处于上游时，速度分布也会受温度场不均匀的影响而出现不对称，冷侧的平均速度下降至约 50m/s，高气速区域明显缩小。电弧的不断伸缩是流体曳力和电磁力约束共同作用的结果，高温下的高气速使流体曳力增强，电弧被拉伸，同时电压升高，使电弧具有更高的热功率和温度，进而电导率

增加，电流密度增加，电磁力增强，电弧受到约束，形成波动。

2.2.2 含甲烷载气与惰性载气热力学性质的差异

含甲烷混合气与纯氩气分别作载气时，等离子体放电特性的区别主要是载气的热力学性质差异造成的，图 6 为两种气体的比热容和电导率随着温度变化的曲线。可见含甲烷混合气体的比热容高于氩气比热容 3~4 个数量级，因此相同温度下其焓值也高于氩气，故在功率一定的情况下，为了维持电弧核心区的高温，甲烷混合气放电的高温区更加集中，高温区与周边流体的温度梯度更大。同时，含甲烷混合气的电导率在 7000K 后显著小于氩气电导率，即含甲烷的混合气体放电难度增加，因此需要高电压来维持通路，一方面功率需求增大，另一方面电弧在空间中的扩散和传导难度增加，体现在电弧形态上即倾向于形成长度更长、半径更小的电弧，与模拟、实验结果均相符。

2.2.3 载气流量与电流设定值的影响

图 7 显示了不同载气流量下（甲烷入口体积分数保持不变）反应器中心轴线的温度分布。流量较小时（5L/min 与 10L/min）稳定状态下轴线温度分布相似，最高温接近 12000K；当流量为 20L/min 时，由于电弧稳定性下降、波动明显，中心轴线温度随时间发生显著变化，2ms 时中心轴线大部分位置的温度在 10⁴K 左右，5ms 时电弧偏移，只在炬出口（30mm 位置）处的温度仍可达到 10⁴K，其余位置的温度显著下降，而 8ms 时电弧被挤压在炬内一侧，高温完全偏离中心，因此中心轴线温度骤降，轴线平均温度不足 2000K。

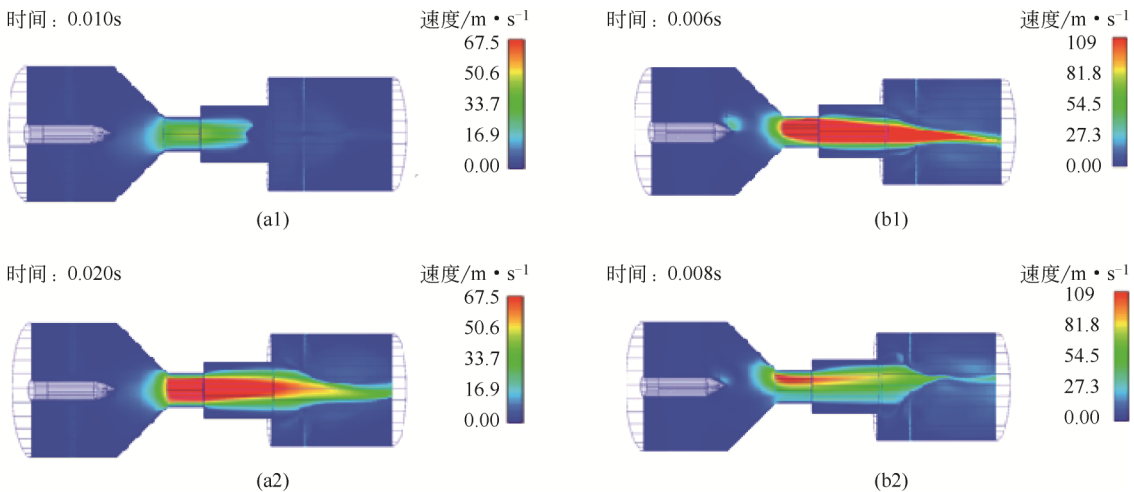


图 5 不同气氛下反应器内的速度分布
(a1)、(a2)纯氩载气；(b1)、(b2)含甲烷载气

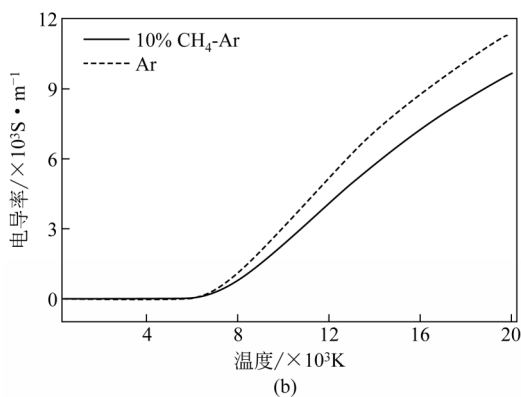
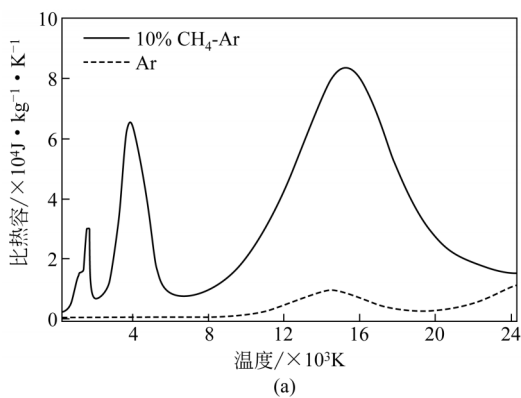


图6 两种气体的比热容及电导率随温度变化关系

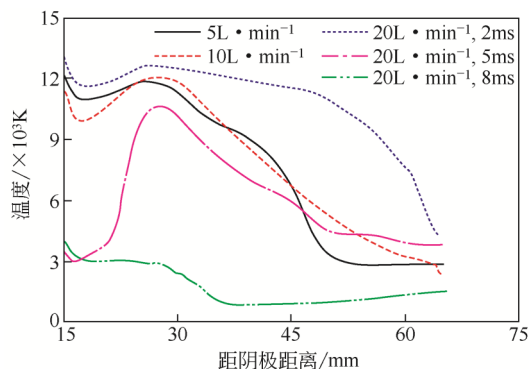


图7 不同含甲烷载气流量下(甲烷入口体积分数不变)反应器轴线温度分布

综合来看,载气量过小时高温射流的延伸性较差,而载气量过大时,由于流动的不稳定性增加,电弧出现偏移或短路的概率增大,因此也不利于反应的正常进行,故需要选择一个合适的载气流量。

如图8所示为电流提高至60A后甲烷混合气放电的中心轴线温度分布。首先提高电流后电流密度等值面的半径增加,电弧核心高温区的半径对应增加。其次,60A下轴线的温度分布在形态上与40A下的分布相似,但比40A下的温度高1000~2000K,45mm后的温度下降主要是由于电弧发生了一定偏移。

此外,电弧仍存在波动现象,但波动的范围和

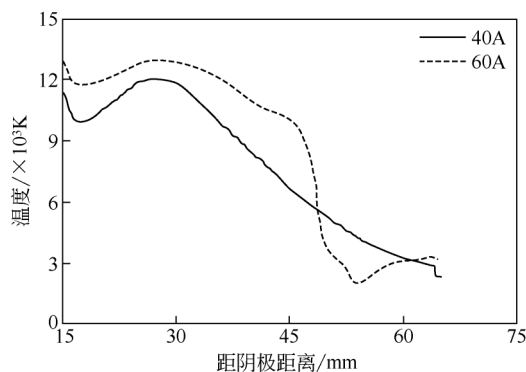


图8 不同电流下反应器轴线温度分布

频率与40A下类似,速度分布也没有出现显著不同,说明提高电流后增加的功率主要用于升温,而非转化为动能。在实验中提高电流后甲烷转化率和乙炔收率都有所提升,从模拟结果可知这是由于射流平均温度有了较大提升。

2.3 宏观动力学模型下的等离子体甲烷裂解过程

热力学平衡模型下的模拟缺少对于反应的描述以及各物质浓度分布的相关信息,需要进一步利用宏观动力学模型进行考察。计算时设定气体入口处甲烷的质量分数固定为0.0427(对应于10%的体积分数),其余为氩气,载气流量10L/min,电流设定值40A。

2.3.1 反应对等离子体的影响:宏观动力学模型下的放电特性

首先考察电弧和温度场的情况。图9为电弧和温度在不同时间下的形态和分布,1ms时电弧阳极弧根靠近炬出口,位置高于热力学平衡模型下的弧根位置,并且移动较为缓慢,发展到2.5ms时达到进料混合段,5ms时达到反应段,5.5ms时才发生第1次弧根转移;同时在形态上,电流密度等值面的边缘变得十分粗糙,尤其是靠近阴极的高温部分出现了较明显的褶皱,这是由于反应的发生使得气体组成发生显著变化,局部物理性质梯度过大所致。相比热力学平衡模型,电弧高温区的温度梯度更大,热量在中心区域更加集中,这是因为反应生成大量氢气,氢气的焐值要高于同温度下的甲烷和乙炔,故热量被用于维持中心气体温度,而热力学平衡模型中氢气的体积分数要小于动力学模型中的氢气体积分数。

这样大的梯度意味着在本模型精度下,电弧的稳定性主要受气体热力学性质影响,并取决于不同组分物质的空间分布,即化学反应是电弧不稳定性的主要来源,此处注意区分“不稳定性”和“波动”——“波动”主要指电弧运动、变化的周期规

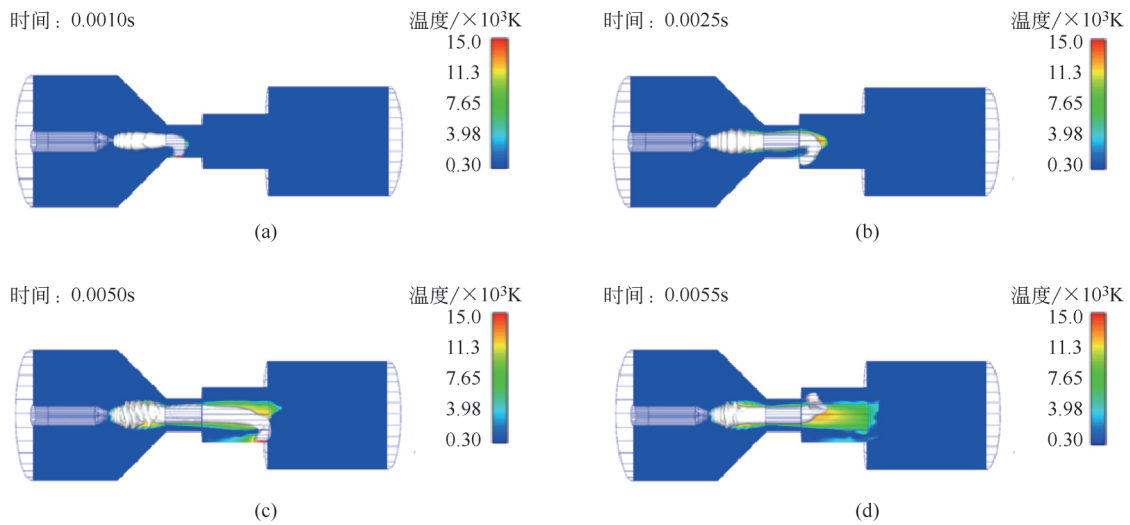


图9 宏观动力学模型下电弧的运动变化及温度分布情况

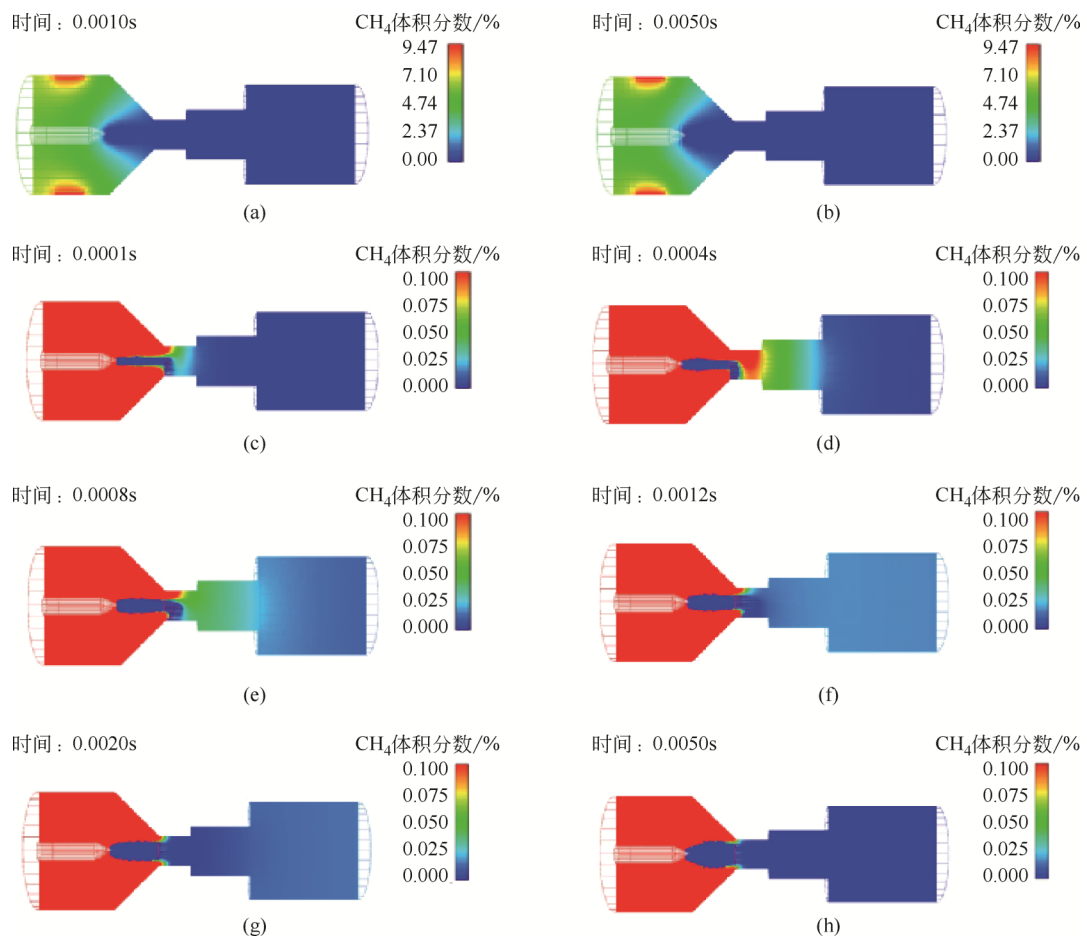


图10 反应器内甲烷体积分数分布变化情况

律，“不稳定性”主要指电弧波动的规律不稳定、电弧不能稳定存在等现象。电弧的波动更多是流体曳力与电磁力互相平衡的结果，当化学反应造成气体分布不均匀时，电弧的空间稳定形态和运动模式受到干扰，从而使其稳定性下降，一方面波动幅度

增大、规律性下降（周期性被一定程度破坏），另一方面更易出现极端情况而使电弧熄灭。

2.3.2 等离子体对反应的影响：各组分体积分数的空间分布

图10为甲烷的体积分数分布，图10(a)、(b)中

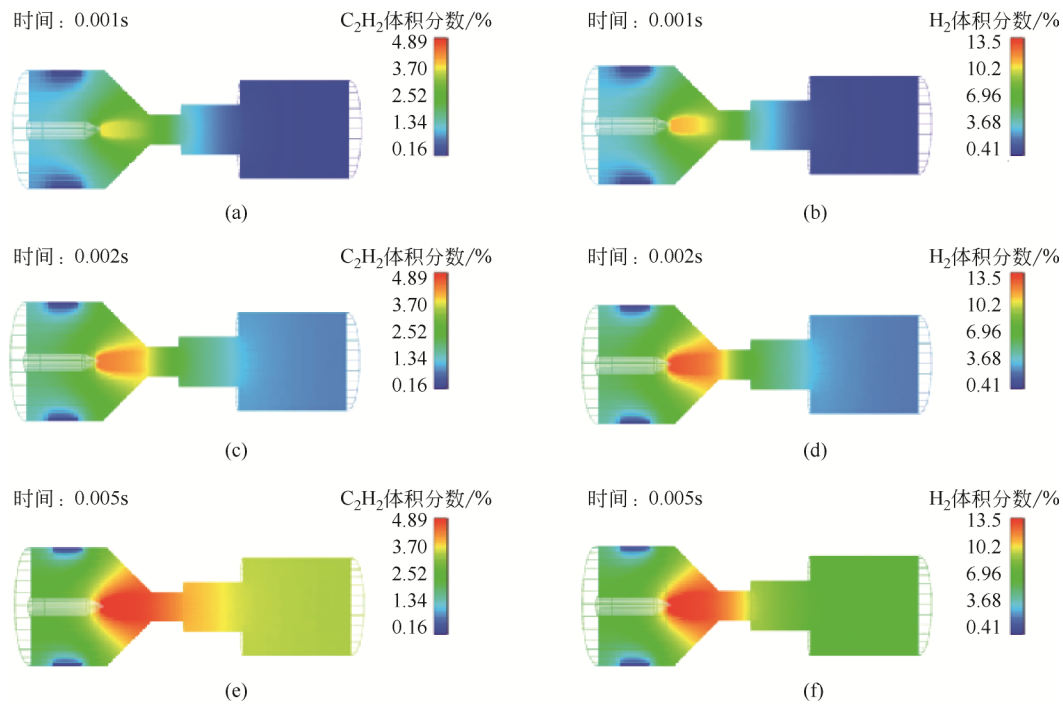


图 11 反应器内乙炔和氢气体积分数分布变化情况

红色代表的体积分数为 10%，在 1~5ms 之间甲烷的分布情况变化较小，并且在电弧区几乎全部转化，下游反应段的体积分数小于 0.1%。为了清楚地表示甲烷的扩散、转化过程，将红色代表的体积分数设定为 0.1%，如图 10(c)~(h)所示，在 1ms 内甲烷绕过电弧扩散至进料混合段，之后随着电弧的发展和温度的升高而迅速转化，在 2~5ms 内下游反应段的甲烷体积分数逐渐降低，最终甲烷在反应器内的分布达到稳定。根据体积分数计算得到的甲烷转化率在 99% 以上，与实验中预混策略下甲烷的高转化率相符。此外与温度分布对比可知，温度梯度较大的位置甲烷浓度梯度也较大，例如电弧阴极极端边缘处，这是由于反应较为迅速（反应速率常数在 8000K 下的数值为 $1.15 \times 10^{13} s^{-1}$ ），故甲烷被迅速消耗，从而形成较大梯度。

图 11 为乙炔和氢气的体积分数分布情况。从 1~5ms 反应迅速发生，乙炔和氢气首先从炬内阴极附近生成，随射流流动并扩散至下游反应段，逐渐形成稳定的浓度分布，这一方面证实了炬内空间温度较高，反应首先在这一区域发生（并且由于没有考虑辐射，炬内反应发生的程度实际上被低估了），另一方面说明气体向下流动的阻力较大，存在一定程度的返混等现象。同时，电弧高温区附近的产物体积分数最高，尤其是阴极电极末端到炬出口的位置，充分说明高温对于甲烷裂解反应具有极

大的促进作用。

在所考察时段内，浓度场尚未完全稳定，反应器出口中心位置的乙炔体积分数大约为 3.9%，氢气体积分数大约为 7.6%，与实验和热力学计算的数据有一定差别（表 2），一方面这与所选用的反应模型较为简单有关，实际过程中甲烷并不完全转化为乙炔，乙炔会继续分解生成炭黑，产物的体积分数要小于目前的模拟结果。另一方面表中的数据均来自带淬冷的实验，除载气外仍有 10L/min 的氩气用于淬冷，故氩气体积分数较高，对其他组分的平衡浓度也有一定影响。

由反应器内不同物质的浓度分布随时间的变化可知，即便电弧的运动造成了电弧的不稳定以及射流温度场和速度场的不均匀，浓度场受到的影响却比较小，各物质在反应器内的分布较为对称。浓度

表 2 不同条件下的反应体系组成

组分体积分数/%	热力学平衡		实验结果
	2000 K	1500 K	
Ar	94.61	94.84	94.09
CH ₄	0.001	0.067	0.231
C ₂ H ₂	1.111	0.890	1.194
C ₂ H ₄	0	0.010	0.016
H ₂	4.161	4.054	3.249
C ₆ H ₆	0	0.029	
C ₁₀ H ₈	0	0.036	

场的均匀性一方面来自于预混策略下载气组成的均匀性,反应在空间内能够均匀地发生,另一方面高温下气体的传递(扩散和对流)较为迅速,10⁴K下氢气的扩散系数约为0.038m²/s,通过炬出口段缩径的特征时间大约为0.7ms,这一特征时间小于电弧弧根的移动和变化特征时间(约2ms),射流温度场和速度场的变化则更要滞后,因此浓度场的发展更为迅速,受影响较小。这定性解释了实验中等离子体电压波动较大但下游气体组成仍较为稳定的现象。

综上,将甲烷裂解反应宏观动力学引入本MHD模型中后,可知在等离子体放电区发生的反应会对电弧的形态和稳定性造成较大影响,而相对地,由于电弧区的温度极高,反应的发生较为迅速,各物质浓度的空间均匀性受电弧波动影响较小。这是由于等离子体的特性主要由气体组分的热力学性质决定,也意味着需要通过控制反应的进行程度(例如控制原料气浓度)来得到更稳定的等离子体工作状态。

3 结论

数值模拟是研究高温、瞬态变化的热等离子体过程的有效方法,本文建立了热等离子体直流电弧反应器的数学模型,使用磁流体力学理论对热等离子体甲烷裂解过程进行数值模拟,考察了电弧运动变化的规律和射流场的特点,并分别通过热力学平衡模型和宏观动力学模型探索了反应与电弧的相互影响关系。电弧做规律运动和形态变化,以壁面弧根附着点的变换和水平面内的转动为主,氩气氛围下运动较平稳,形态变化不显著;含甲烷混合气作为载气时等离子体稳定性下降,电弧拉伸程度增大,弧根附着点变换频率增大,更易出现冷气“短路”现象。载气流量会影响电弧的稳定性,不宜或高或过低,增大电流获得的能量将主要用于提升电弧的温度。此外,使用热力学平衡模型可以获得含甲烷混合气的放电特性,但模型缺乏对反应的描述,需要耦合宏观动力学模型。结果表明甲烷裂解反应的发生会使放电区气体组成发生迅速变化,对电弧造成显著影响,化学反应是等离子体不稳定性的重要来源。同时由于高温下气体扩散迅速,各物质的浓度分布较为均匀和对称,受温度场非均匀性的影响较小。甲烷的转化率达到99%,乙炔质量收率约81%(完全转化情况下),实验中较优条件下甲烷转化率约95%,乙炔质量收率在60%~73%之

间,与模拟结果相近。本模拟工作为理解热等离子体甲烷裂解实验结果提供了帮助,是对MHD模型与化学反应模型相结合的有益尝试,未来仍可在等离子体模型和反应动力学模型的精细化方面加以探索。

参考文献

- [1] FINCKE J R, ANDERSON R P, HYDE T, et al. Plasma thermal conversion of methane to acetylene[J]. *Plasma Chemistry and Plasma Processing*, 2002, 22(1): 105-136.
- [2] CHENG Yan, YAN Binhang, LI Tianyang, et al. Experimental study on coal tar pyrolysis in thermal plasma[J]. *Plasma Chemistry and Plasma Processing*, 2015, 35(2): 401-413.
- [3] AN Hang, CHENG Yan, LI Tianyang, et al. Numerical analysis of methane pyrolysis in thermal plasma for selective synthesis of acetylene[J]. *Fuel Processing Technology*, 2018, 172: 195-199.
- [4] 程炎,李天阳,金涌,等.热等离子体超高温化学转化的过程研发和应用进展[J]. *化工进展*, 2016, 35(6): 1676-1686.
CHENG Yi, LI Tianyang, JIN Yong, et al. State-of-the-art development of research and applications of chemical conversion processes at ultra-high temperature in thermal plasma reactors[J]. *Chemical Industry and Engineering Progress*, 2016, 35(6): 1676-1686.
- [5] 张祥富,曾达权.天然气等离子体法制乙炔[J]. *天然气化工*, 1998(4): 39-43.
ZHANG Xiangfu, ZENG Daquan. The plasma method for acetylene production from natural gas[J]. *Natural Gas Chemical Industry*, 1998(4): 39-43.
- [6] 王志斌,陈国旭,王哲,等.三电极非热电弧发生器放电模式的实验研究[J]. *清华大学学报(自然科学版)*, 2014(1): 73-77.
WANG Zhibin, CHEN Guoxu, WANG Zhe, et al. Experimental investigation of the discharge modes of a non-thermal arc plasma generator with three-electrode configuration[J]. *Journal of Tsinghua University (Science and Technology)*, 2014(1): 73-77.
- [7] 付友,王振,王宁会.用于高效冶炼氧化镁的双电极直流电弧炉的仿真与实验[J]. *电工技术学报*, 2016, 31(24): 79-87.
FU You, WANG Zhen, WANG Ninghui. Simulation and experiment investigation on a dual-electrode DC arc furnace with high smelting efficiency for MgO production[J]. *Transactions of China Electrotechnical Society*, 2016, 31(24): 79-87.
- [8] 董其鹏,张炯明,雷少武,等.直流等离子体电弧特性的模拟[J]. *焊接学报*, 2014(12): 27-30.
DONG Qipeng, ZHANG Jiongming, LEI Shaowu, et al. Simulation of characteristics of DC plasma arc[J]. *Transactions of the China Welding Institution*, 2014(12): 27-30.
- [9] TANG K M, YAN J D, CHAPMAN C, et al. Three-dimensional modelling of a DC arc plasma in a twin-torch system[J]. *Journal of Physics D: Applied Physics*, 2010, 43(34): 345201.
- [10] HUR M, HONG S H. Comparative analysis of turbulent effects on thermal plasma characteristics inside the plasma torches with rod- and well-type cathodes[J]. *Journal of Physics D: Applied Physics*, 2002, 35(16): 1946-1954.
- [11] 余徽,印永祥,戴晓雁.等离子体射流裂解甲烷制乙炔的数值模拟[J]. *化工学报*, 2006, 57(10): 2319-2326.
YU Hui, YIN Yongxiang, DAI Xiaoyan. Numerical simulation of methane conversion to acetylene in plasma jet reactor[J]. *Journal of Chemical Industry and Engineering (China)*, 2006, 57(10): 2319-2326.
- [12] 周前红.直流电弧等离子体炬的数值模拟[D].上海:复旦大学,

- 2009.
- ZHOU Qianhong. Numerical simulation of a DC arc plasma torch [D]. Shanghai: Fudan University, 2009.
- [13] 李和平, 陈熙. 等离子体反应器中传热与流动的三维数值模拟[J]. 工程热物理学报, 2001(3): 324-327.
- LI Heping, CHEN Xi. Three-dimensional simulation of heat transfer and fluid flow in a thermal plasma reactor[J]. Journal of Engineering Thermophysics, 2001(3): 324-327.
- [14] WU Changning, CHEN Jiaqi, CHENG Yi. Thermodynamic analysis of coal pyrolysis to acetylene in hydrogen plasma reactor[J]. Fuel Processing Technology, 2010, 91: 823-830.
- [15] National Aeronautics and Space Administration Glenn Research Center. Chemical equilibrium with applications[CP/OL]. [2019-01-17]. <https://cearun.grc.nasa.gov>.
- [16] 罗义文, 漆继红, 印永祥, 等. 热等离子体裂解甲烷的热力学与动力学分析[J]. 四川大学学报(工程科学版), 2003(4): 33-37.
- LUO Yiwen, QI Jihong, YIN Yongxiang, et al. Kinetic and thermodynamic analysis of the thermal plasma decomposition system of methane[J]. Journal of Sichuan University (Engineering Science Edition), 2003(4): 33-37.
- [17] HOLMEN A, ROKSTAD O A, SOLBAKKEN A. High-temperature pyrolysis of hydrocarbons. I. Methane to acetylene[J]. Industrial & Engineering Chemistry Research, 1976, 15(3): 439-444.
- [18] HOLMEN A, OLSVIK O, ROKSTAD O A. Pyrolysis of natural gas: chemistry and process concepts[J]. Fuel Processing Technology, 1995, 42(2): 249-267.
- [19] 郭平, 涂汉敏, 汪周华, 等. 多组分气-气扩散系数的计算[J]. 天然气工业, 2015, 35(8): 39-43.
- GUO Ping, TU Hanmin, WANG Zhouhua, et al. Calculation of multi-component gas-gas diffusion coefficient[J]. Natural Gas Industry, 2015, 35(8): 39-43.
- [20] LI Tianyang, REHMET C, CHENG Yan, et al. Experimental comparison of methane pyrolysis in thermal plasma[J]. Plasma Chemistry and Plasma Processing, 2017, 37(4): 1033-1049.
- [21] 李和平, 吴贵清, 李鹏, 等. 阴极边界条件对双射流电弧等离子体特性影响的二维数值模拟[J]. 高电压技术, 2013(7): 1549-1556.
- LI Heping, WU Guiqing, LI Peng, et al. Two-dimensional modeling concerning the effects of the boundary conditions along the cathode sheath-arc column interface on the characteristics of the dual-jet arc plasmas[J]. High Voltage Engineering, 2013(7): 1549-1556.
- [22] MORROW R, LOWKE J J. A one-dimensional theory for the electrode sheaths of electric arcs[J]. J. Phys. D: Appl. Phys., 1993, 26: 634.



DOI: 10.16085/j.issn.1000-6613.2022-0902

熔融金属法甲烷裂解制氢和碳材料研究进展

何阳东, 常宏岗, 王丹, 陈昌介, 李雅欣

(中国石油西南油气田公司天然气研究院, 四川 成都 610213)

摘要: 熔融金属法甲烷裂解技术作为近年来新兴的制氢技术, 有效地解决了传统甲烷热裂解或催化裂解高能耗、低转化率以及催化剂失活等问题, 避免了甲烷蒸汽重整制氢工艺高碳排放。在制氢的同时还能生产出具有附加值的碳产品, 因而受到各方广泛关注。本文总结了熔融金属法甲烷裂解技术研究进展, 并围绕工艺流程、反应机理、熔融介质的选择以及反应器设计等方面展开, 给出了液相介质是否起催化作用的两类甲烷裂解反应机理, 并详细阐述了熔融介质选择原则、发展趋势以及不同类型熔融介质的优缺点。再者, 技术经济性以及温室气体减排量也在文中详细体现, 进一步论证了该工艺的可行性和潜在效益。此外, 文中还给出了未来技术发展趋势和建议, 指出调控碳材料形貌, 使之向高附加值碳材料转变应是未来重点发展方向之一。

关键词: 熔融金属; 熔融盐; 甲烷; 热解; 氢; 碳产品

中图分类号: TE09

文献标志码: A

文章编号: 1000-6613 (2023) 03-1270-11

Development of methane pyrolysis based on molten metal technology for coproduction of hydrogen and solid carbon products

HE Yangdong, CHANG Honggang, WANG Dan, CHEN Changjie, LI Yaxin

(Research Institute of Natural Gas Technology, PetroChina Southwest Oil & Gasfield Company, Chengdu 610213, Sichuan, China)

Abstract: Molten metal methane pyrolysis is an emerging hydrogen production technology in recent years. Compared with conventional methane pyrolysis and catalytic pyrolysis, it effectively overcomes the problems of high energy consumption, low conversion and catalyst deactivation, and also avoids the high carbon emission as in steam methane reforming technology. The ability to produce value-added solid carbon products along with hydrogen has attracted extensive attention. This article summarizes the latest research and development of methane pyrolysis based on molten metal technology, focusing on the process flow, reaction mechanism, selection of molten medium and reactor design *etc.* We also propose two types of potential reaction mechanisms for elucidating whether the liquid medium plays a catalytic role in methane pyrolysis. Moreover, the selection principle, trends in the development, benefits and drawbacks of different types of molten media are comprehensively elaborated. And the technical economy and greenhouse gas emission reduction also have been discussed, which further demonstrates the feasibility and potential benefits of the process. Finally, suggestions for future technological improvements are presented, and we points out morphology regulation of carbon materials to facilitate transformation into high-value-added products should inevitably become one of the key development directions in the future.

Keywords: molten metal; molten salt; methane; pyrolysis; hydrogen; solid carbon products

收稿日期: 2022-05-16; 修改稿日期: 2022-08-29。

基金项目: 中国石油西南油气田公司博士后基金 (20220306-11)。

第一作者及通信作者: 何阳东 (1992—), 男, 博士后, 研究方向为氢能及碳捕集。E-mail: heyd01@petrochina.com.cn。

引用本文: 何阳东, 常宏岗, 王丹, 等. 熔融金属法甲烷裂解制氢和碳材料研究进展[J]. 化工进展, 2023, 42(3): 1270-1280.

Citation: HE Yangdong, CHANG Honggang, WANG Dan, et al. Development of methane pyrolysis based on molten metal technology for coproduction of hydrogen and solid carbon products[J]. Chemical Industry and Engineering Progress, 2023, 42(3): 1270-1280.

对零CO₂排放能源系统的渴望源于对气候变化的认知，特别是在《巴黎气候协定》背景下，各国开始在碳中和方面竞赛。氢能因其具有绿色清洁、多样化来源以及广泛用途被视为未来清洁能源重要组成部分。

我国相继于2016年在《能源技术革命创新行动计划2016—2030》和《“十三五”国家科技创新规划》中将氢能列为重要发展方向，同年在《中国氢能产业基础设施发展蓝皮书》中首次指出氢能发展路线图，并于2019年将氢能纳入《政府工作报告》，2021年发布了《氢能产业标准化白皮书》。尽管从长远角度来看，使用可持续、可再生能源（风能、太阳能、生物质能、核能等）为基础的制氢技术更具有发展前景，但受能耗、成本、效率、资源分布以及技术水平的制约，使得化石能源制氢在短期乃至21世纪中下叶仍将发挥着重要的作用^[1-2]。当前，世界氢气总产量的96%来源于以化石能源为基础制备，其中，甲烷蒸汽重整制氢（SMR）约占48%，这主要得益于较低的生产成本和相对成熟的工艺^[3]。然而，高能耗（供给的甲烷约1/3被直接用来燃烧供能）、高碳排放（产1kg H₂排放CO₂ 9~12kg^[4]）使得该工艺与当前越来越严苛的环境政策以及低碳经济相悖。因此，在向可持续氢能过渡期间，寻觅一种更清洁、更低碳的化石能源利用方式，对加快氢能规模化利用和完善相关产业链发展具有重要意义。

对于低碳氢生产而言，甲烷热裂解法被视为潜在的、低成本生产方法。因其理论上生成氢气所需要能量仅为SMR过程的约60%（产1mol H₂耗能37.7kJ vs. 63.4kJ），约为电解水制氢能消耗的13%（产1mol H₂耗能37.7kJ vs. 285.8kJ），且产物中不含CO₂。然而，传统甲烷热裂解技术面临着高反应温度、低转化效率以及炭沉积在催化剂活性位点造成催化剂失活等问题，使得该工艺难以大规模商业化应用^[5]。熔融金属法甲烷裂解技术通过利用液态金属作为传热介质和催化剂促使甲烷在液态金属中直接裂解，生成氢气和碳材料。生成的碳材料由于其密度远低于液态金属而自发漂浮在金属表面，实现固体炭直接分离，有效避免了传统甲烷裂解过程中上述种种弊端，且生成的碳材料可进一步处理变成高值碳，因而受到大量关注。本文对近年来熔融金属法甲烷裂解制氢和碳材料技术进行详细概述，并给出今后需持续攻关方向展望。

1 熔融金属法甲烷裂解工艺

熔融金属法甲烷裂解反应大多都在鼓泡反应器中进行，如图1所示。为了增强气液接触有效传热表面积，促进原料气在液态金属体系中均匀分布，通常在进气管出口端加入多孔分布器。研究表明多孔分布器的加入能有效提高原料气的转化率，促进氢气和碳材料生成。例如，Serban等^[6]对比了两种不同尺寸大小的进气管，即0.21in和0.02in（1in=25.4mm），发现后者较前者甲烷气泡大小减少了近10倍，转化率随之增加了5倍。若采用Mott多孔分布器，甲烷转化率还将进一步提升，源于分布器表面具有更细小的气孔结构，提供了良好的气泡传播能力。此外，增加原料气与液相金属接触的时间或提高裂解反应温度也能增大甲烷转化率，而接触时间主要与熔融金属液相层高度以及输入气流速等有关。为了减少甲烷气体加热所需的时间，可对原料气进行预热，但预热温度不易过高否则将导致少部分甲烷气体直接裂解，生成的碳颗粒会堵塞分布器气孔。

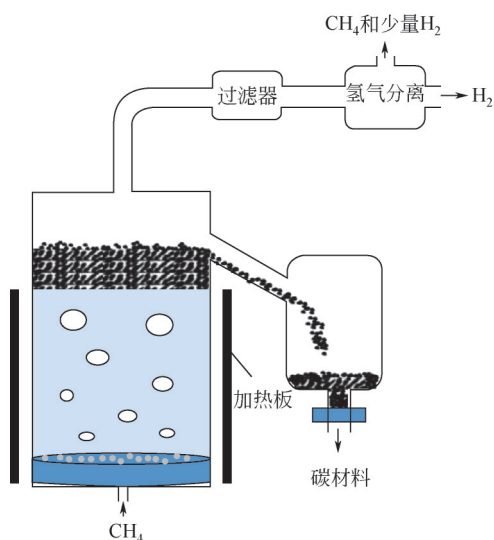


图1 熔融金属法甲烷裂解制氢和碳材料装置示意图

进入熔融金属液相层的原料气在不断上升过程中发生裂解反应，生成氢气和固体炭材料，由于生成的碳材料密度远低于熔融金属而漂浮在液相表面，当累积到一定高度时从反应器的开口处分离出来。生成的碳材料可以是炭黑、石墨烯、碳纳米管、碳纤维等高附加值碳材料，这主要取决于使用的金属种类。另一方面，所制备的碳材料表面通常会附着微米或纳米级的金属颗粒，造成碳材料不

纯,需进一步净化处理。可采用去离子水在超声震荡中去除明显的金属杂质,再进行酸洗及过滤,最后用去离子和无水乙醇反复清洗,最终烘干即可得到纯净的碳材料^[7]。

甲烷裂解生成的氢气则从反应器顶部排出,排出的气体中除了氢气和部分未反应完全的甲烷外,还夹带少量固体炭颗粒。可先通过过滤器处理掉固体颗粒,再进行氢气提纯。当前氢气提纯的方法主要有深冷法、膜分离法、吸收-吸附法以及变压吸附法等,根据技术成熟度、能耗、提纯氢气纯度、投资成本以及操作难易程度等综合考虑,变压吸附法具有明显的优势。经变压吸附后的尾气(主要是甲烷以及少量未完全分离的氢气)则可用于燃烧供能或是循环回反应器以提高原料气的转化率。

熔融金属法甲烷裂解氢和碳联产工艺具有如下优势:①避免了传统甲烷催化裂解过程中,催化剂因表面积炭逐步失活问题,实现了系统产物持续、稳定的输出;②整个过程无氧气参与,使得反应过程中无 CO_x 化合物生成,产物仅以固体炭输出,无直接 CO_2 排放;③在生产氢气的同时,还可生产高附加值碳材料,有助于降低制氢成本,提高技术经济性。当碳税等相关政策实施后,系统经济效益还将进一步释放;④若考虑碳捕集、碳运输、碳压缩、碳封存等能耗,其能量利用效率显著高于煤制氢工艺,且能与SMR工艺相竞争^[8];⑤整个装置占地面积小,能有效降低对土地资源的需求。

2 甲烷裂解反应机理

当前,熔融金属法甲烷裂解制氢和碳材料技术可根据液相金属是否做催化剂分为两类,即非催化甲烷裂解反应和催化甲烷裂解反应。

2.1 非催化甲烷裂解反应机理

对于非催化甲烷裂解反应,尽管前人已经提出多种反应机理,但目前尚未形成统一认识。大多研究人员较为认同Chen等^[9]提出的观点,认为在反应过程中甲烷首先分解成甲基自由基和氢原子, C_{2+} 烃类是由甲基自由基与其他中间烃类反应生成,整个热解反应是逐级进行的。在第一阶段,甲烷分解成甲基自由基和氢原子,随后形成乙烷和氢气;在第二阶段,通过乙烷自由基脱氢得到乙烯,并且乙烷也可以解离成两个甲基自由基;在第三阶段,乙烯分别通过自由基脱氢和自由基甲基化反应生成乙炔和丙烯,乙炔进一步裂解生成碳单质。与此同时,乙烷生成速率急剧增加,该现象并不能用上述

反应机理加以解释,显然涉及到自催化。部分研究者认为自催化现象是由于反应中催化活性炭生成所引起的;另一部分人则认为这是由于出现新的自由基导致乙烷及其衍生物生成速率增加,新的自由基可能是乙炔或丙烯等^[10]。此外,通过引入可逆反应、异构化反应以及加成反应等使得甲烷裂解反应机理得到了进一步扩展^[11]。

虽然研究人员普遍认为甲烷裂解为甲基自由基和氢原子是限制整个热解反应速率的关键步骤,但也有研究人员提出不同的见解,认为控制反应速率在于甲烷裂解为亚甲基和氢分子,如图2所示。这种在反应初始以及反应速率控制步骤上的差异可能与甲烷热解实验采用不同反应温度有关。在低于 1400°C 下,实验中观察到甲烷分解为甲基自由基和氢原子,而在高于 1400°C ,甲烷热解为亚甲基和氢分子^[12]。

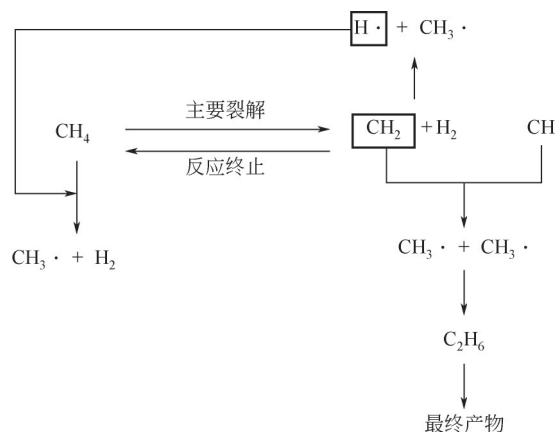


图2 Kevorkian等^[13]及Kozlov等^[14]提出非催化甲烷热解反应机理

2.2 催化甲烷裂解反应机理

对于催化甲烷裂解反应,研究者认为甲烷首先吸附在催化剂表面,然后解离生成具有化学吸附性的 CH_3^* 和 H^* ,并经过一系列的表面逐步脱氢反应,最终形成氢气和固体炭颗粒,具体反应过程如图3所示^[15]。就其限速步骤而言,研究人员提出了不同的见解:一些研究者认为从吸附的甲烷分子中分离出第一个氢原子,形成具有吸附性的甲基自由基是控制速率的关键步骤^[16];另一些研究者则认为甲烷的吸附解离以及从甲基自由基中分离出第二个氢原子是限制甲烷催化裂解速率的关键^[17]。

Wang等^[18]研究了熔融态金属镁对甲烷裂解催化作用机理并提出了潜在反应路线,如图4所示。金属镁由于自身具有较强的还原性以及高温熔融态

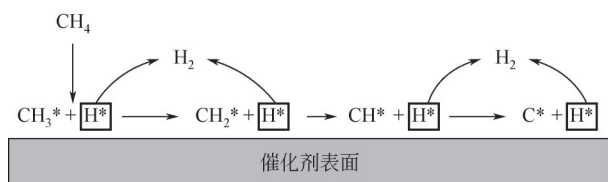
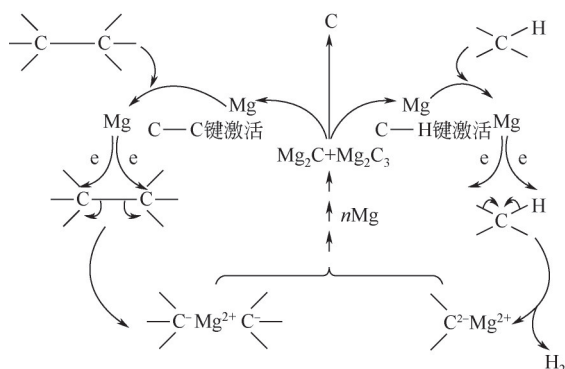


图3 催化甲烷热解反应机理

图4 CH_4 或其他碳氢化物在熔融金属镁中的反应机理^[18]

为活化甲烷分子中C—H键提供了充足的能量，促使其断裂，所得碳负离子与镁离子结合生成镁的碳化物（ Mg_2C_3 和 Mg_2C ）和氢气。由于反应处于熔融体系，生成的产物能迅速与液态金属镁分离，有利于反应源源不断向着产物方向进行。并且镁的碳化物在高温下极不稳定，易分解成镁单质和固体炭，进而实现镁的再生，再生后的金属镁又继续活化碳氢化合物中其他C—H键，实现整个反应的循环。

Zhou等^[19]研究了熔融金属铁对甲烷裂解反应活性的影响，结果表明不仅金属铁对甲烷裂解具有催化活性，生成的中间产物碳化铁同样具有催化性。反应机理为甲烷首先在 Fe^0 表面分解成无定形炭（ $\text{C}_{\text{amorphous}}$ ）和氢气，无定形炭再继续与 Fe^0 反应生成 Fe_3C ，并作为裂解反应自身的催化剂。随着反应进行，炭的持续沉积将导致 Fe_3C 过饱和而形成 $\text{Fe}_3\text{C}_{1+x}$ ，并迅速分解回 Fe_3C ，同时将无定形炭转变为石墨炭（ $\text{C}_{\text{graphite}}$ ），具体反应路径如式(1)~式(4)^[19]。



3 熔融介质类型

熔融介质的选择是熔融金属法甲烷裂解制氢和碳材料的关键基石，利用其特性促使反应在液相中

进行，避免了传统甲烷催化裂解因反应生成的炭粉吸附在催化剂表面，覆盖活性位点造成催化剂寿命大幅降低的缺陷，有力地保障了反应持续、稳定的进行。当前，对于熔融介质的筛选和研究主要集中在金属单质、金属合金以及金属盐，对上述熔融介质的选择通常需要兼顾以下特点。

(1) 低熔点、高沸点。低熔点有助于降低金属熔融过程中能量的消耗以及对反应器材耐高温的要求；高沸点则避免熔融态金属在反应温度下出现挥发流失现象。此外，低熔点、高沸点能在较宽的温度范围内保持金属液相状态，为反应提供充足的操作空间。

(2) 具有良好的化学稳定性。在反应温度范围内金属合金以及金属盐不易热分解，且相对容易获取或制备。

(3) 低黏度、低张力。流体中粒子的扩散速率和碰撞次数取决于黏度，进而影响系统的反应速率，而低黏度有利于反应物之间较好的混合；张力则主要决定了气泡的形成，当向液相金属底部通入甲烷气体时，气泡的大小除了与输入管孔径有关外，还与液相金属表面张力和容器高度密切相关。

3.1 金属单质

金属锡由于具有较低的熔点以及较宽的可操作液相反应温度范围（232~2600℃），常被用作熔融法甲烷裂解的金属介质，例如：Serban等^[6]以金属锡为反应液相介质，采用Mott多孔分布器作为甲烷的进料器，输入甲烷组分为95% CH_4 和5% C_2H_6 ，在反应温度750℃下，甲烷转化率达到51%，生成的碳材料主要为石墨，且反应过程中乙烷转化率始终高于甲烷，主要源于乙烷分子的C—H键能相对较低。在标准状况下，乙烷裂解生成1mol氢气仅需要消耗能量为28.2kJ，而甲烷需消耗能量37.4kJ，因此反应过程中乙烷优先分解^[6]。Geibler等^[8]发现在装填液相金属锡高度为1m的鼓泡反应器中，甲烷通入量50mL/min，反应温度为1175℃，氢气产率可达78%，生成的固体炭呈粉末状，并在反应器壁上发现了部分碳纳米管。然而，近期的研究表明金属锡并没有最初报道的高催化活性，而是作为一种传热介质，生成的固体炭产品可能在甲烷裂解过程中起到催化作用^[20]。

Wang等^[18]考察了熔融态金属镁对甲烷热裂解性能的影响，并对其活化机理进行详细阐述，具体描述如上文所示，这里不再赘述。研究同时发现在

甲烷流量保持为 5 mL/min, 反应温度为 700 °C 条件下, 甲烷转化率接近 25%, 远高于同等反应条件下甲烷直接热解转化率 (约为 5%), 并且每摩尔氢气生产能耗仅为 SMR 工艺的 65.1%, 生成的碳颗粒微观形貌为不规则类似羽毛结构。倘若采用两级串联反应器, 甲烷转化率还将进一步提升。然而, 由于金属的蒸发作用, 镁在高温下的稳定性较差, 限制了其工业放大。Tang 等^[21]以熔融态金属铜作为甲烷裂解的液相介质, 在 1450 °C 下, 输入甲烷摩尔分数为 5%, 石墨烯产量可达 9.4 g/h, 甲烷转化率为 58%, 且生成的石墨烯品质较传统液相剥离法更优。此外, 研究还发现大部分石墨烯生长是在气泡表面进行, 也有极少量石墨烯是在熔融金属铜表面形成。温度和甲烷浓度对石墨烯的生长影响较大, 随着反应温度和甲烷浓度的增高, 石墨烯生长速度随之变快, 其厚度也逐渐增大。Zeng 等^[22]研究了熔融金属铈对甲烷裂解的催化性能, 为了防止液态金属蒸发, 反应器中安装回流装置。整个反应器采用分段加热, 反应器底部温度维持在 1000 °C、中部保持在 900~1000 °C, 顶部维持为 480 °C, 当输入甲烷摩尔分数在 70% 时, 甲烷转化率为 37%, 且该产率在 16 h 内保持稳定, 生成的碳材料是具有层状结构的石墨。文中还指出不仅液态金属铈具有催化活性, 其蒸气同样具有催化活性, 后者的催化活性明显低于前者。值得注意的是由于金属铈较为稀有、易挥发以及价格昂贵, 其不大可能用于商业化应用。Pérez 等^[23]探究了熔融金属镓及其装载高度对甲烷裂解性能的影响, 输入气流量保持 450 mL/min, 甲烷摩尔分数为 50%, 液相金属镓装载高度 50 mm, 反应温度在 960~995 °C 时, 甲烷转化率为 69%~74%。当装载高度升高至 150 mm, 甲烷转化率达到 80% 以上, 且随着温度升至 1119 °C, 甲烷转化率超过了 90%, 生成的碳材料为炭黑。高转化率源于多方面因素, 如镓金属良好的催化活性、多孔分布器应用提高气液接触面积、较高的反应温度和液相介质高度。此外, 低分压的甲烷输入也有利于裂解反应朝着氢气生成方向进行。

3.2 金属合金

鉴于对甲烷热解具有催化活性的金属 (Ni、Pt、Cu、Pd 等) 普遍具有较高的熔点, 需要供应大量的能量使其达到熔融状态, 增加了系统能耗。因而, 科研工作者开始把目光转移到金属合金中, 将具有催化活性的高熔点金属与低熔点金属结合形成低熔点、高活性金属合金。

Upham 等^[24]以 $\text{Ni}_{0.27}\text{Bi}_{0.73}$ 合金为液相介质、填充高度为 1.1 m、在反应温度 1065 °C 下, 甲烷转化率达到 95%, 反应产物主要为高纯度氢气和石墨, 且该合金催化性能能长时间保持稳定。研究同时还指出熔融态合金的活性金属原子是分散并具有电负性的。在此基础上, Palmer 等^[25]分析该合金对甲烷、丙烷、苯以及原油的热解性能, 发现在相同反应条件下, 甲烷的转化率最低, 源于其结构最稳定。生成的碳产品方面, 丙烷、苯和原油主要为炭黑, 而甲烷则是石墨。敖东羿等^[26]分析了 Ni_2Sn_8 合金在不同裂解温度及甲烷浓度下对碳材料生成结果影响, 研究表明随着反应温度以及甲烷浓度的增高, 原料转化率及产品产率均呈上升趋势。其中, 在甲烷摩尔分数为 10%、反应温度为 1300 °C 时, 甲烷转化率达到 77.05%, 生成的碳产品石墨烯达到 0.49 g/h。最近的研究指出 $\text{Cu}_{0.45}\text{Bi}_{0.55}$ 合金对甲烷裂解催化活性优于 $\text{Ni}_{0.27}\text{Bi}_{0.73}$ 合金, 且 Cu 的价格较 Ni 更便宜^[27]。尽管纯 Cu 或纯 Bi 均不是很好的甲烷裂解催化剂, 但两者结合形成的合金却显示出较高的活性, 实验结果表明 Bi 在熔融铜中的溶解可以起到表面活性剂作用, 少量 Bi 的加入大大降低了液态铜的表面张力, 且 Bi 在熔融 Cu-Bi 合金中的表面富集, 其活性因铜原子作用得到激活, 缺电子的 Bi 位点促进了甲烷的裂解。

3.3 金属盐

由于熔融态金属与正在生成中的碳原子相互作用以及金属蒸发沉积在固体炭表面造成碳材料纯度不高, 若进行后续净化处理, 成本可能会急剧增高。例如, Upham 等^[24]发现在以 Ni-Bi 合金为液相介质的熔融金属甲烷裂解中, 回收的碳材料纯度只有 61% (质量分数), 如此大量的金属耗损在经济上是不可接受的。熔融盐具有不互溶性 (不溶于熔融金属和碳产品) 以及水中溶解度高等特点, 常被用于工业生产分离提纯, 如冶金净化^[28]。与熔融金属相比, 熔融盐成本更低, 且生成的固体炭可以在单独的容器中以较低温度将金属盐去除。

近年来, 以熔融态金属盐作为甲烷裂解反应液相介质开始受到研究人员的关注, 得到的固体炭产品通过简单的水洗就可以去除金属盐污染, 进而得到净化。然而, 仅含熔融盐的甲烷裂解反应体系难以在较低温度下实现较高转化。因此, 在熔融盐中加入一些金属催化剂构成熔融金属与熔融盐两相或多相液相介质是不错的选择, 其作用原理如图 5 所示。

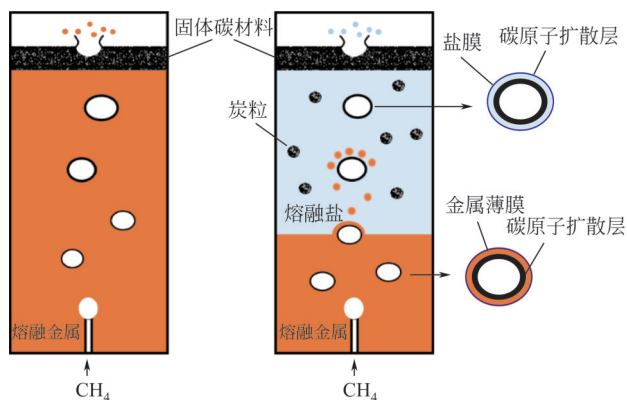


图5 气泡通过熔融金属（左）和熔融金属与熔融盐构成两相液相介质（右）示意图

从图5中可以看出，在没有盐层情况下，气泡周围的金属薄膜会一直存在，直至气泡到达液面表层破裂，金属液滴将污染所有的炭表面。在含盐层的熔融金属两相液相介质中，当气泡到达熔融金属与熔融盐交界处，金属薄膜剥离并分散到熔融盐中，由于其密度较高，金属液滴将下沉至熔融金属液相层，而低密度的固体炭则上升至熔融盐表面，有效降低金属污染^[29]。并且熔融金属与熔融盐之间的表面张力差将使得界面处气泡体积快速增加而破裂，进一步加强该过程^[30]。

Kang 等^[31]采用摩尔比为 0.67/0.33 的 MnCl_2 与 KCl 熔融盐混合物作为甲烷裂解催化剂，其表观活化能得到大幅降低，相较于纯 KCl 熔融盐作催化剂下降约 139kJ/mol ，这可能与熔融液相介质中 MnCl_4^- 粒子存在有关。在 1050°C 下，甲烷转化率达到 55%，生成的碳产品主要为石墨碳，通过水清洗，盐的污染可减少到 4% 以下。在考察 NaCl 与

KCl 混合熔融盐对甲烷热裂解催化特性时，发现加入 FeCl_3 盐后，其表观活化能从 301kJ/mol 降低到 171kJ/mol ，生成的碳产品从无序炭转变为具有石墨结构的炭产品，碳纯度达到 93.7%^[32]。Rahimi 等^[29]发现在 $\text{Ni}_{0.27}\text{Bi}_{0.73}$ 熔融合金体系中加入熔融溴盐，生产的碳产品金属杂质含量低于 0.1%（质量分数），且随着熔融盐层高度的增加而进一步降低。相较于未加入熔融盐的 $\text{Ni}_{0.27}\text{Bi}_{0.73}$ 合金，其生成的碳材料形貌也发生改变，前者生产的固体炭含有炭黑和碳纳米管，而后者只检测到石墨炭。表 1 总结了熔融金属与熔融盐构成的两相液相介质体系中不同装载高度以及洗涤方式对生成炭的纯度影响，该分析结果是在反应温度为 1000°C 、甲烷输入为 70% 条件下获得的。

Noh 等^[4]发现与两相液相介质（ Ni-Bi 合金与 KBr ）相比，三相液相介质（ Ni-Bi 合金、 ZrO_2 以及 KBr ）中甲烷转化率在 985°C 下能从 32% 提高到 37%，且均获得类似的碳材料（无序炭和石墨基炭）。氧化锆颗粒的加入限制了气泡的大小，间接增大气泡与液相介质表面的接触面积，提高甲烷裂解速率，同时也有利于熔融金属与熔融盐之间气泡的流动。Parkinson 等^[33]以碱金属卤化盐（ NaBr 、 KBr 、 KCl 、 NaCl 和 48.7% NaBr -51.3% KBr 混合物）作为甲烷热裂解液相反应介质，考察其催化性能并对反应生成的碳材料进行表征。从动力学来看，其活化能在 $223.5\sim 277.6\text{kJ/mol}$ ，显著低于甲烷直接热裂解活化能 422kJ/mol ，显示出了一定的催化活性。经去离子水洗涤后，炭的纯度在 55.0%~91.6%（质量分数），若经过进一步真空处理或酸洗，纯度还

表 1 金属熔融与熔融盐两相反应器中甲烷裂解碳材料组分分析结果（质量分数）^[29]

熔融介质	装载高度/mm	纯化方式 ^①	C/%	Ni/%	Bi/%	Na/%	K/%	Br/%
NiBi	350	—	17.36	12.98	69.66	—	—	—
NiBi	350	真空加热	51.82	1.84	46.34	—	—	—
NiBi	350	酸洗	58.81	4.09	37.10	—	—	—
NiBi/KBr	110/110	水洗+真空加热	85.63	0.82	1.10	—	3.73	8.72
NiBi/KBr	240/110	水洗	85.68	0.22	0.66	—	4.38	9.06
NiBi/KBr	240/110	水洗+真空加热	98.22	0.23	0.32	—	0.36	0.87
NiBi/KBr	110/240	水洗	74.19	0.06	0.42	—	8.07	17.26
NiBi/KBr	110/240	水洗+真空加热	88.47	0.10	0.00	—	3.60	7.83
NiBi/KBr	110/240	水洗+酸洗	84.63	0	0.00	—	4.98	10.39
NiBi/NaBr	110/240	水洗	95.06	0.18	0.56	1.06	—	3.14
NiBi/NaBr	110/240	水洗+真空加热	97.40	0.18	0.00	0.59	—	1.83
NiBi/NaBr	110/240	水洗+酸洗	97.34	0	0.00	1.15	—	1.51

① 真空加热温度为 1000°C ；水洗与酸洗干燥温度为 90°C 。

将大幅上升。此外, 研究结果还表明炭的纯度与卤盐的粒径以及卤盐对固体炭表面湿润性密切相关, 粒径越小、湿润性越差则炭的纯度越高。与Na盐相比, K盐对碳材料表面的粘附能更高, 相应的盐的污染也更大。NaCl由于较小的粒径以及低黏附性, 其作为熔融液相介质得到的碳材料纯度最高。

综上, 熔融介质发展历程可概括分为三个阶段(图6), 即金属单质向金属合金转变、金属合金向熔融盐转化、熔融盐向多相熔融介质转变。在金属单质中, 金属的催化活性与其电负性密切相关, 通常具有催化活性的金属熔点都较高, 而非催化活性金属虽具有低熔点, 但其催化活性也较低。因此, 将两者特性结合起来形成低熔点、高活性的金属合金, 此为第一阶段的转变。在金属合金中, 科研人员开展了大量的工作, 发现Ni-Bi合金与Cu-Bi合金显示出较好活性, 但无论是使用金属单质还是金属合金作熔融介质, 生成的碳材料均存在金属污染, 造成后续处理繁杂, 成本显著上升。金属盐因水中溶解度高、不溶于固体炭产品以及液相金属、低成本等优点, 使得研究人员开始将注意力转移到利用金属盐作为熔融介质上, 此为第二阶段转变。然而, 在使用熔融盐作液相介质时, 尽管生成的碳材料中金属污染可有效避免, 但反应活性也显著降低, 原料转化率大幅减小。虽然采用两种盐或多种盐的混合作为熔融液相介质有助于提高甲烷转化率, 但增幅有限。因而, 研究人员又开始向金属单质或金属合金与熔融盐组成的二相或多相液相介质转变, 此为第三阶段转变。最终目的是形成低熔点、高活性、低成本、低金属污染的液相介质。

4 反应器

反应器是甲烷热裂解的另一核心部件, 对于熔

融金属法甲烷裂解反应器而言, 其常采用鼓泡反应器, 它能在高温下稳定运行, 并且具有较大的气液界面, 因而具备良好的加热特性。

对于立式鼓泡反应器, 在有限的表观速度下, 想要实现较大气体吞吐量, 可通过增加压力的方式来减少所需反应器的数量, 但这会对反应器材质提出较高的要求, 大幅增加设备成本。Parkinson等^[34]提出利用卧式反应器, 在有限的表观速度下通过延长反应器的长度来为气体注入创造更大的横截面积, 从而提高气体吞吐量, 反应器内部设计如图7所示。对于碳连续分离, 这里借鉴了石油加工中卧式三相分离器的经验。

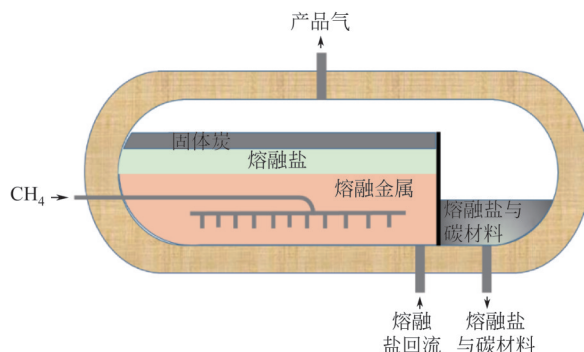


图7 Parkinson等提出的熔融金属甲烷裂解反应器设想^[34]

苟富均等^[35]设计出了一种甲烷热裂解反应装置如图8所示, 反应器左上角分别安装导流槽和回流槽, 其分别用于排出固体炭颗粒以及与导流槽对流换热。对于导流槽而言, 其内部设置有翅片结构, 有利于液态金属和固体炭颗粒在导流槽内形成湍流, 使得固体炭颗粒尽量析出并漂浮于液态金属表面, 有利于后续碳分离和收集。对于导流槽的设置, 一方面降低了反应器流入过渡腔室的固体炭以及液态金属的温度, 进而降低过渡腔室对材质和结

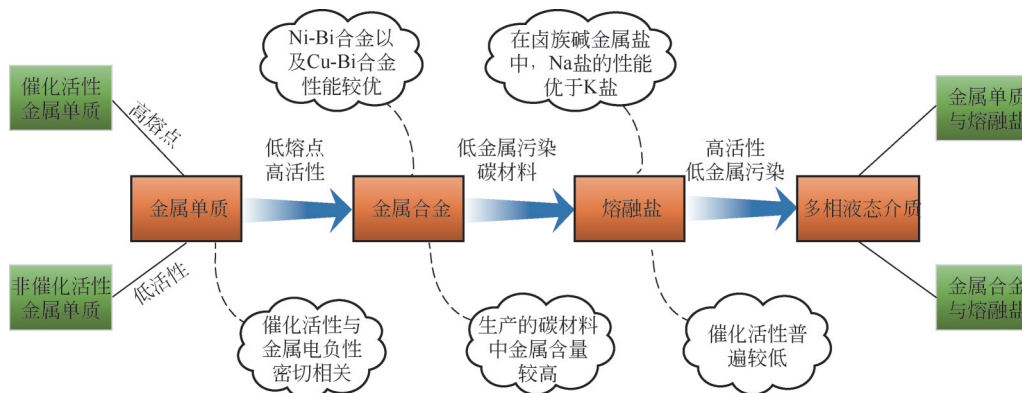
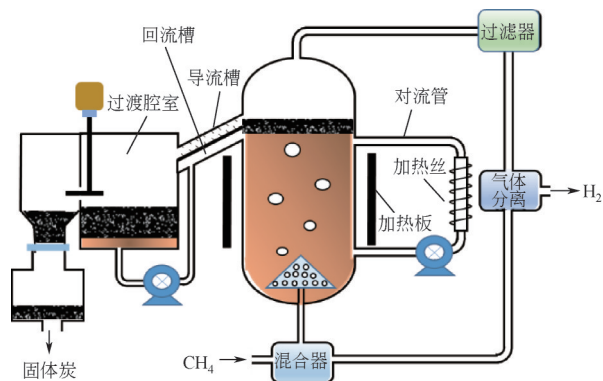
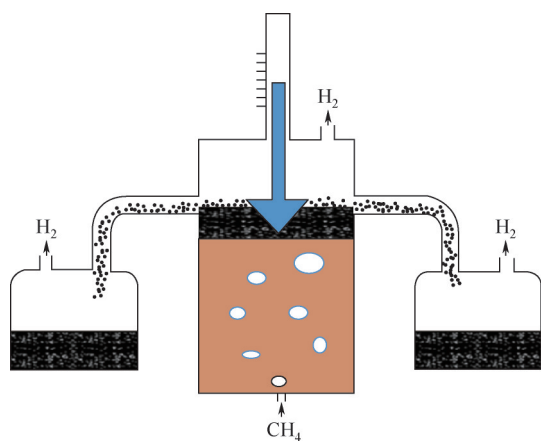


图6 熔融介质发展趋势

图8 苟富均等设计的熔融金属甲烷热裂解装置^[35]

构的要求；另一方面，又能使从过渡腔室流入到反应器的液态金属升温，达到节能目的。反应器右端安装对流管，通过电磁泵的作用使得反应器内的液态金属保持循环流动，实现甲烷与液态金属的对流，促进甲烷裂解反应的进行。对流管外部安有加热丝，以保持液态金属必要的温度。过渡腔室的固体炭颗粒在液态金属表面堆积，并被叶片扫入至收集腔室进而储存，液态金属则在电磁泵的作用下输送至回流槽进行循环利用。

Kudinov 等^[36]设计出一种可以周期性分离的碳装置，如图9所示，通过在反应器内插入一个浮动结构来检测熔融金属的水平高度，当达到某一临界值时，就会启动真空装置，固体炭颗粒将从反应器两侧排出并被收集。

图9 Kudinov 等设计的熔融金属甲烷裂解装置示意图^[36]

5 经济评估

在评估不同制氢系统性能优劣时，除了关注系统自身耗能情况外，生产成本也是一个重要的考核指标。在某种程度上，生产成本是决定一个系统是

否具有竞争力的关键因素。熔融金属法甲烷裂解技术是一种潜在的替代SMR工艺方法，生产出来的碳材料还可以作为副产品进行销售，从而提高了系统的经济可行性。

Parkinson 等^[37]对比了熔融金属法甲烷裂解技术与SMR工艺，发现在碳税为78USD/t，碳产品价值在200USD/t时，以电加热供热方式的熔融金属法生产的氢气成本较SMR工艺更具竞争力，且整个工艺的经济性受甲烷的转化率以及碳产品的价值影响较大。值得注意的是，这里熔融态金属并未考虑其催化活性。因而，Parkinson 等^[34]继续研究了具有催化活性Ni-Bi合金对甲烷裂解工艺经济性能影响，反应热来源于甲烷燃烧供应，生产的副产品碳材料以150USD/t计算，在没有考虑碳税时，SMR制氢工艺氢气生产成本最低。当碳税超过21USD/t时，熔融金属甲烷热裂解工艺相较于SMR工艺更具有低成本氢气生产优势。Timmerberg 等^[38]分析了三种不同甲烷热分解方式，即等离子体法甲烷热分解、熔融金属法甲烷热分解以及传统甲烷直接热分解，并将获得的结果与电解制氢以及SMR制氢工艺相比。结果显示甲烷热分解系统制氢成本在1.6~2.2EUR/kg，大大高于SMR过程制氢成本1.0~1.2EUR/kg，但低于电解制氢成本2.5~3.0EUR/kg，然而这里并未考虑裂解过程生成碳的价值，造成氢气生产成本较实际偏高。Pérez 等^[23]分析了熔融金属镓作液相介质甲烷热裂解经济可行性，并考察了不同供能方式（天然气燃烧供能、氢气燃烧供能、碳燃烧供能以及电供能）对氢气生产成本的影响。在假定碳产品售价为296EUR/t、碳税为50EUR/t时，通过燃烧部分碳产品为熔融金属法甲烷裂解供能所得到的氢气成本，能与装备碳捕集的SMR工艺相竞争。值得注意的是，研究人员同时也指出将碳产品定价为296EUR/t是相对较为保守的估值，远低于前人所提出500~4000EUR/t的估价。表2总结了SMR工艺、质子交换膜电解水以及熔融金属法三种不同制氢工艺投资成本，在年产10万吨氢气且内部收益率（IRR）为10%条件下，产1kg氢气平准化生产成本分别为1.26USD、7.13USD和1.39USD。当碳税价格约为21USD/t时，熔融金属法较SMR工艺更具优势，而对于质子交换膜电解水，碳税需要超过600USD/t才能与SMR工艺相竞争。另一方面，若SMR工艺加装碳捕集装置，假定CO₂捕集率为90%，碳捕集及封存成本为78USD/t时，碳税价格要超过300USD/t，加装碳捕集装置

表2 不同制氢工艺年产10万吨氢气投资成本

成本	SMR	质子交换膜电解水	熔融金属法
总装置成本/10 ⁶ USD	42	495.8	40.8
总投资成本/10 ⁶ USD	252.1	829.1	349.7
运行成本/10 ⁶ USD·a ⁻¹	94.5	582.4	122
原料成本/10 ⁶ USD·a ⁻¹	63.2	543.8	92.8
净电输出/MW _e	12.6 ^①	—	5.4 ^①
1kg H ₂ 的碳排放/kg	9.3	0	2.5
氢气售价 (IRR=10%) /USD·kg ⁻¹	1.26	7.13 ^②	1.39 ^③
与SMR工艺IRR收益为10%相等时, 碳税价格/USD·t ⁻¹	—	585	18

① 净电售价0.06USD/kWh; ② 电价假定为0.1USD/kWh; ③ 碳产品价格假定150USD/t。

的SMR工艺才能与熔融金属法相竞争。

6 环境评估

尽管甲烷热裂解过程中并不直接产生CO₂, 但热解反应需供给一定的能量以维持该过程的持续稳定进行, 这将间接导致温室气体排放。因此, 对于整个系统的环境可行性还需要进行系统性评估。

Abúnades等^[39]对比了SMR工艺、煤气化制氢工艺以及甲烷热解工艺, 发现单位输出氢能所对应的碳排放量排列顺序为甲烷热解制氢工艺<SMR制氢工艺<煤气化制氢工艺, 其产1kg H₂的CO₂排放量数值分别为1.1kg、7.48kg以及18.26kg。Steinberg等^[40]指出甲烷热裂解生产氢气对应的碳排放远低于SMR工艺, 仅为后者的约12%。为了减少SMR工艺碳排放量, 需要对排放的CO₂进行捕集并封存, 然而该过程将导致系统能效损失约15%, 使得在净能量利用效率上装备碳捕集的SMR工艺与甲烷热裂解工艺基本持平。Pérez等^[23]对比了不同供能方式对熔融金属法甲烷热裂解工艺碳排放的影响, 并与SMR工艺进行对照, 这里供能方式主要有燃烧部分碳产物供能、氢能供能、甲烷燃烧供能以及电供

能。获得的结果如表3所示, 从表中可以看出无论采用那种供能方式其单位输出氢能对应的CO₂排放量均低于SMR工艺, 显示出熔融金属法较优的环境效益。然而, 当SMR工艺装备碳捕集设施后, 碳排放量大幅降低, 从1kg H₂产生CO₂排放量9.18kg降至1.57kg, 此时对于熔融金属法甲烷裂解技术而言, 仅有电供能以及燃烧部分氢能供能才能与之竞争。若考虑碳捕集工艺同样装备在以甲烷或碳为燃料的熔融金属法甲烷热裂解工艺中, 其单位输出氢能对应的CO₂排放量同样低于装备碳捕集的SMR工艺, 类似的研究可以在Parkinson等^[37]报道中发现。Rodat等^[41]发现当采用太阳能供能时, 相较于传统SMR工艺以及气炉法制炭黑工艺, 在相同的氢气与碳产品产量下, 能减少92%的污染物排放。Dufour等^[42]从全生命周期角度出发, 对熔融金属法甲烷裂解技术进行环境评估, 发现即使与装备碳捕集设备的SMR工艺相比, 其生命周期内温室气体排放量也明显低于后者。Postels等^[43]进一步指出, 相较于SMR工艺, 甲烷热裂解技术在全生命周期内能实现64%的温室气体减排, 进一步证实了熔融金属甲烷裂解技术的环境可行性。

表3 不同供能方式对碳排放的影响

CO ₂ 捕集条件	SMR		熔融金属法 (碳供能)		熔融金属法 (氢供能)	熔融金属法 (天然气供能)		熔融金属法 (电供能)
	—	MDEA脱碳	—	MEA脱碳		—	MEA脱碳	
反应温度/°C	890	890	1200	1200	1200	1200	1200	1200
反应压力/MPa	3.2	3.2	1	1	1	1	1	1
NG 流量/kg·s ⁻¹	2.62	2.81	3.86	3.86	7.31	5.33	5.33	3.86
H ₂ 流量/kg·s ⁻¹	0.75	0.75	0.75	0.75	0.75	0.75	0.75	0.75
1mol CH ₄ 的H ₂ 产率/mol	2.49	2.48	1.65	1.63	0.93	1.25	1.23	1.71
1kg H ₂ 的CO ₂ 排放量/kg	9.18	1.57	5.26	0.45	1.46	6.16	0.56	1.01
CO ₂ 减排率/%	—	83	43	95	84	33	94	89

7 结语与展望

熔融金属甲烷裂解技术由于液态金属独特的性质以及均相催化能力，其活性组分不再拘泥于某一特定区域而是处于自由移动状态，有效地避免了传统催化裂解炭沉积、催化剂失活等现象。然而，激活甲烷分子需要较高活化能以及碳产品的分离和提纯，使得熔融金属法甲烷裂解技术在商业化应用前，仍面临着不小的挑战。在未来的研究中应着重关注以下几个方面。

(1) 当前，熔融金属甲烷裂解技术研究主要集中在早期的实验阶段，尽管相关金属催化材料研究已取得了阶段性进展，但裂解反应温度普遍较高，原料转化率依然较低。因此，在接下来的研究中应持续重视对高催化活性、低熔点、低经济成本的金属催化材料研发。一方面，这有助于提高甲烷燃料的利用率，增加目标产品产率；另一方面，还有助于降低甲烷裂解过程中对能量的需求，降低系统能耗，减少因购买耐高温设备以及额外的燃料供给的投资成本。

(2) 调控碳材料形貌，使得生成的碳产品向高纯度、高附加值碳材料转变，提高系统经济可行性，并在最大产率和最小经济成本投入以及氢气收益和碳材料价值之间寻求适当的平衡，以实现综合效益最大化。

(3) 加大对熔融金属与熔融盐构成的二元或多元液相介质研究，以降低碳产品中金属污染，减少后续净化处理成本；加强对产品气以及碳材料中所包含的显热利用，提高系统能量利用效率。

(4) 有必要对熔融金属甲烷裂解制氢和碳材料工艺进行全面分析，探究不同供能方式对碳排放的影响。同时，相较于传统单产系统，该工艺在能源节约率、减排潜能以及经济成本节约量上都有待进一步分析。

参考文献

[1] ABÁNADES A, RUBBIA C, SALMIERI D. Thermal cracking of methane into Hydrogen for a CO₂-free utilization of natural gas[J]. *International Journal of Hydrogen Energy*, 2013, 38(20): 8491-8496.

[2] HE Yangdong, ZHU Lin, FAN Junming, et al. Life cycle assessment of CO₂ emission reduction potential of carbon capture and utilization for liquid fuel and power cogeneration[J]. *Fuel Processing Technology*, 2021, 221: 106924.

[3] HE Yangdong, ZHU Lin, LI Luling, et al. Hydrogen and power cogeneration based on chemical looping combustion: is it capable of reducing carbon emissions and the cost of production?[J]. *Energy &*

Fuels, 2020, 34(3): 3501-3512.

[4] NOH Y G, LEE Y J, KIM J, et al. Enhanced efficiency in CO₂-free hydrogen production from methane in a molten liquid alloy bubble column reactor with zirconia beads[J]. *Chemical Engineering Journal*, 2022, 428: 131095.

[5] ABÁNADES A, RUIZ E, FERRUELO E M, et al. Experimental analysis of direct thermal methane cracking[J]. *International Journal of Hydrogen Energy*, 2011, 36(20): 12877-12886.

[6] SERBAN M, LEWIS M A, MARSHALL C L, et al. Hydrogen production by direct contact pyrolysis of natural gas[J]. *Energy & Fuels*, 2003, 17(3): 705-713.

[7] AO Dongyi, TANG Yongliang, XU Xiaofeng, et al. Highly conductive PDMS composite mechanically enhanced with 3D-graphene network for high-performance EMI shielding application[J]. *Nanomaterials (Basel, Switzerland)*, 2020, 10(4): 768.

[8] GEIBLER T, ABÁNADES A, HEINZEL A, et al. Hydrogen production via methane pyrolysis in a liquid metal bubble column reactor with a packed bed[J]. *Chemical Engineering Journal*, 2016, 299: 192-200.

[9] CHEN C J, BACK M H, BACK R A. The thermal decomposition of methane. II. Secondary reactions, autocatalysis and carbon formation; non-Arrhenius behaviour in the reaction of CH₃ with ethane[J]. *Canadian Journal of Chemistry*, 1976, 54(20): 3175-3184.

[10] CHEN C J, BACK M H, BACK R A. Mechanism of the thermal decomposition of methane[J]. *ACS Symposium Series*, 1976(32): 1-16.

[11] ROSCOE J M, THOMPSON M J. Thermal decomposition of methane: Autocatalysis[J]. *International Journal of Chemical Kinetics*, 1985, 17(9): 967-990.

[12] KHAN M S, CRYNES B L. Survey of recent methane pyrolysis literature[J]. *Industrial & Engineering Chemistry*, 1970, 62(10): 54-59.

[13] KEVORKIAN V, HEATH C E, BOUDART M. The decomposition of methane in shock waves[J]. *The Journal of Physical Chemistry*, 1960, 64(8): 964-968.

[14] KOZLOV G I, KNORRE V G. Single-pulse shock tube studies on the kinetics of the thermal decomposition of methane[J]. *Combustion and Flame*, 1962, 6: 253-263.

[15] CHEN Q Q, LUA A C. Kinetic reaction and deactivation studies on thermocatalytic decomposition of methane by electroless nickel plating catalyst[J]. *Chemical Engineering Journal*, 2020, 389: 124366.

[16] WANG Jiaofei, LI Xiaoming, ZHOU Yang, et al. Mechanism of methane decomposition with hydrogen addition over activated carbon via *in-situ* pyrolysis-electron impact ionization time-of-flight mass spectrometry[J]. *Fuel*, 2020, 263: 116734.

[17] YADAV M D, DASGUPTA K, PATWARDHAN A W, et al. Kinetic study of single-walled carbon nanotube synthesis by thermocatalytic decomposition of methane using floating catalyst chemical vapour deposition[J]. *Chemical Engineering Science*, 2019, 196: 91-103.

[18] WANG K, LI W S, ZHOU X P. Hydrogen generation by direct decomposition of hydrocarbons over molten magnesium[J]. *Journal of Molecular Catalysis A: Chemical*, 2008, 283(1/2): 153-157.

[19] ZHOU Lu, ENAKONDA L R, HARB M, et al. Fe catalysts for methane decomposition to produce hydrogen and carbon nano materials[J]. *Applied Catalysis B: Environmental*, 2017, 208: 44-59.

[20] PLEVAN M, GEIBLER T, ABÁNADES A, et al. Thermal cracking of methane in a liquid metal bubble column reactor: Experiments and kinetic analysis[J]. *International Journal of Hydrogen Energy*, 2015, 40(25): 8020-8033.

[21] TANG Yongliang, PENG Peng, WANG Shuangyue, et al. Continuous production of graphite nanosheets by bubbling chemical vapor deposition using molten copper[J]. *Chemistry of Materials*, 2017, 29

- (19): 8404–8411.
- [22] ZENG J R, TARAZKAR M, PENNEBAKER T, et al. Catalytic methane pyrolysis with liquid and vapor phase tellurium[J]. *ACS Catalysis*, 2020, 10(15): 8223–8230.
- [23] PÉREZ B J L, MEDRANO JIMÉNEZ J A, BHARDWAJ R, et al. Methane pyrolysis in a molten gallium bubble column reactor for sustainable hydrogen production: Proof of concept & techno-economic assessment[J]. *International Journal of Hydrogen Energy*, 2020, 46(7): 4917–4935.
- [24] UPHAM D C, AGARWAL V, KHECHFE A, et al. Catalytic molten metals for the direct conversion of methane to hydrogen and separable carbon[J]. *Science*, 2017, 358(6365): 917–921.
- [25] PALMER C, BUNYAN E, GELINAS J, et al. CO₂-Free hydrogen production by catalytic pyrolysis of hydrocarbon feedstocks in molten Ni–Bi[J]. *Energy & Fuels*, 2020, 34(12): 16073–16080.
- [26] 敖东羿. 多层高品质石墨烯的大量制备及其应用研究[D]. 成都: 电子科技大学, 2020.
AO Dongyi. Study on massive production of multilayer high-quality graphene and its applications[D]. Chengdu: University of Electronic Science and Technology of China, 2020.
- [27] PALMER C, TARAZKAR M, KRISTOFFERSEN H H, et al. Methane pyrolysis with a molten Cu–Bi alloy catalyst[J]. *ACS Catalysis*, 2019, 9(9): 8337–8345.
- [28] RIEDEWALD F, SOUSA-GALLAGHER M. Novel waste printed circuit board recycling process with molten salt[J]. *Methods X*, 2015, 2: 100–106.
- [29] RAHIMI N, KANG D, GELINAS J, et al. Solid carbon production and recovery from high temperature methane pyrolysis in bubble columns containing molten metals and molten salts[J]. *Carbon*, 2019, 151: 181–191.
- [30] WICHTERLE K. Breakup of gas bubbles rising in molten metals[J]. *Steel Research International*, 2010, 81(5): 356–361.
- [31] KANG D, RAHIMI N, GORDON M J, et al. Catalytic methane pyrolysis in molten MnCl₂–KCl[J]. *Applied Catalysis B: Environmental*, 2019, 254: 659–666.
- [32] KANG D, PALMER C, MANNINI D, et al. Catalytic methane pyrolysis in molten alkali chloride salts containing iron[J]. *ACS Catalysis*, 2020, 10(13): 7032–7042.
- [33] PARKINSON B, PATZSCHKE C F, NIKOLIS D, et al. Methane pyrolysis in monovalent alkali halide salts: Kinetics and pyrolytic carbon properties[J]. *International Journal of Hydrogen Energy*, 2021, 46(9): 6225–6238.
- [34] PARKINSON B, TABATABAEI M, UPHAM D C, et al. Hydrogen production using methane: Techno-economics of decarbonizing fuels and chemicals[J]. *International Journal of Hydrogen Energy*, 2018, 43(5): 2540–2555.
- [35] 苟富均, 陈建军, 叶宗标, 等. 一种催化辅助甲烷裂解制氢的设备: CN113213423A[P]. 2021-08-06.
GOU Fujun, CHEN Jianjun, YE Zongbiao, et al. Catalysis-assisted methane cracking hydrogen production equipment: CN113213423A [P]. 2021-08-06.
- [36] KUDINOV I V, PIMENOV A A, KRYUKOV Y A, et al. A theoretical and experimental study on hydrodynamics, heat exchange and diffusion during methane pyrolysis in a layer of molten tin[J]. *International Journal of Hydrogen Energy*, 2021, 46(17): 10183–10190.
- [37] PARKINSON B, MATTHEWS J W, MCCONNAUGHY T B, et al. Techno-economic analysis of methane pyrolysis in molten metals: Decarbonizing natural gas[J]. *Chemical Engineering & Technology*, 2017, 40(6): 1022–1030.
- [38] TIMMERBERG S, KALTSCHMITT M, FINKBEINER M. Hydrogen and hydrogen-derived fuels through methane decomposition of natural gas–GHG emissions and costs[J]. *Energy Conversion and Management: X*, 2020, 7: 100043.
- [39] ABÁNADES A, RATHNAM R K, GEIBLER T, et al. Development of methane decarbonisation based on liquid metal technology for CO₂-free production of hydrogen[J]. *International Journal of Hydrogen Energy*, 2016, 41(19): 8159–8167.
- [40] STEINBERG M. Fossil fuel decarbonization technology for mitigating global warming[J]. *International Journal of Hydrogen Energy*, 1999, 24(8): 771–777.
- [41] RODAT S, ABÁNADES S, FLAMANT G. Co-production of hydrogen and carbon black from solar thermal methane splitting in a tubular reactor prototype[J]. *Solar Energy*, 2011, 85(4): 645–652.
- [42] DUFOUR J, GÁLVEZ J L, SERRANO D P, et al. Life cycle assessment of hydrogen production by methane decomposition using carbonaceous catalysts[J]. *International Journal of Hydrogen Energy*, 2010, 35(3): 1205–1212.
- [43] POSTELS S, ABÁNADES A, VON DER ASSEN N, et al. Life cycle assessment of hydrogen production by thermal cracking of methane based on liquid–metal technology[J]. *International Journal of Hydrogen Energy*, 2016, 41(48): 23204–23212.